STATUS OF THESIS

Title of thesis | EARLY FLAME CHARACTERISTIC STUDY IN A LEAN CNG DI COMBUSTION

I,_____YOHANNES TAMIRAT ANBESE_____

hereby allow my thesis to be placed at the Information Resource Centre (IRC) of Universiti Teknologi PETRONAS (UTP) with the following conditions:

1. The thesis becomes the property of UTP

2. The IRC of UTP may make copies of the thesis for academic purposes only.

3. This thesis is classified as

☐ Confidential

☑ Non-confidential

If this thesis is confidential, please state the reason:
_____
_____
_____

The contents of the thesis will remain confidential for _____ years.

Remarks on disclosure:

_____
_____
_____

                                        Endorsed by

_____   _____
Signature of Author   Signature of Supervisor

Permanent address   Name of Supervisor
No. 32, Kebele 10   Assoc Prof Dr. Abdul Rashid Bin Abdul
Bole Kifle Ketema   Aziz
Addis Ababa
Ethiopia
Date :_____   Date : _____

UNIVERSITI TEKNOLOGI PETRONAS

EARLY FLAME CHARACTERISTIC STUDY IN A LEAN CNG DI
COMBUSTION

by

YOHANNES TAMIRAT ANBESE

The undersigned certify that they have read, and recommend to the Postgraduate
Studies Programme for acceptance this thesis for the fulfilment of the requirements
for the degree stated.

Signature: _____

Main Supervisor: Assoc Prof Dr. Abdul Rashid Bin Abdul Aziz

Signature: _____

Co-Supervisor: Dr. Zainal Ambri B. Abdul Karim

Signature: _____

Head of Department: Assoc Prof Dr. Ahmad Majdi Bin Abdul Rani

Date: _____

EARLY FLAME CHARACTERISTIC STUDY IN A LEAN CNG DI
COMBUSTION

by

YOHANNES TAMIRAT ANBESE

A Thesis

Submitted to the Postgraduate Studies Programme

as a Requirement for the degree of

DOCTOR OF PHILOSOPHY

MECHANICAL ENGINEERING DEPARTMENT

UNIVERSITI TEKNOLOGI PETRONAS

BANDAR SERI ISKANDAR

PERAK

SEPTEMBER 2011

DECLARATION OF THESIS

Title of thesis	EARLY FLAME CHARACTERISTIC STUDY IN A LEAN CNG DI COMBUSTION

I, _____ YOHANNES TAMIRAT ANBESE _____

hereby declare that this thesis is based on my original work except for quotations and citations which have been duly acknowledged. I also declare that it has not been previously or concurrently submitted for any other degree at UTP or other institutions.

Witnessed by

_____   _____
Signature of Author   Signature of Supervisor

Permanent address: Name of Supervisor
No. 32, Kebele 10   Assoc Prof Dr. Abdul Rashid Bin Abdul
Bole Kifle Ketema   Aziz
Addis Ababa
Ethiopia
Date :_____   Date : _____

This work is dedicated to my wife Rahel and my daughter Ruth; for the memory of those wonderful years we spent together in Malaysia

ACKNOWLEDGEMENT

First, I would like to express my deepest thanks to my supervisors, Associate Professor Dr. Abdul Rashid Abdul Aziz and Dr. Zainal Ambri B. Abdul Karim, for supporting and guiding me to conduct this research and for their kind advice during challenging times of my study. I am very grateful to Prof. Morgan Haikal, Brighton University, for his assistance in my first challenge of PIV experiment. My deepest thanks also go to Mr. Saiful Azrin Zulkifli, Electrical and Electronics department UTP, who assisted me on the LabView and trigger signal generation systems.

I would like to thank the ME lab executive, Mr. Sani, for his fast response and great support during lab material procurement and equipment repairs. I would also like to thank the lab crews, Mr. Mior, Mr. Khairul and Mr. Hazri, for making the automotive lab a good work place. My gratitude also goes to Mr. Jani B Alang Ahmad in the machine lab that assisted me in all my fabrications for my PIV experimental setup.

I am very grateful to my friends, Mr. Ftwi Yohannes and Mr. Firmansyah, they assisted me a lot during data collection. Without their help it would have been challenging for me to work in the lab.

My special thanks go to my wife Rahel and my daughter Ruth. I was very lucky to have them during my study. Their love was so special and comforting.

Behind all these scenes, my Lord was supporting me in His Mighty and divine love. He was comforting me in time of frustration. Thank you Lord, You are my firm foundation.

May God bless you all.

ABSTRACT

Since the invention of the first successful four-stroke Otto cycle engine, engineers and scientists have done a lot to improve engine performance by thorough investigation on air-fuel mixture preparation, creation of turbulence in the cylinder, improving lean combustion, investigation on combustion and emission performance of different kinds of fuels and vary design feature of engine geometries. In regard to this, the study of flame initiation and development has acquired the attentions of many researchers due to its strong dependence to the in-cylinder flows and its capability to influence flame propagation behavior in spark ignition (SI) engines. The objective of this study also focused on this area of flame characterization.

The present study was carried out in two separate experimental setups. The first experiment was the investigation of flow characteristics of the induction process performed on the engine cylinder head using Particle Image Velocimetry (PIV) system. The other experimental work was conducted in a single cylinder direct injection (DI) engine to demonstrate the effect of induction swirl variations on the nature of early flames in a lean-stratified and lean-homogenous compressed natural gas (CNG) combustion at variable engine speeds. Flame images were captured using endoscope and intensified charge-coupled device (CCD) camera. Computer codes were prepared to identify induction flow quantities and flame characteristics.

The study showed that coherent and organized swirling cores were created and observed on the swirl plane of medium and high swirl angle inductions. Swirl intensity was increasing with swirl angle adjustment, whereas velocity RMS values declined with increasing swirl angle. Regarding flame development, the growth rate of the early flame was found to be high in homogeneous combustion than in stratified one. And medium tumble intake showed a better growth rate in stratified combustion, whereas high swirl intake was the best in homogeneous combustion. The medium swirl induction with the strong and compact swirl core resulted in a lower rate of flame development for both stratified and homogeneous combustion cases.

ABSTRAK

Sejak ciptaan yang pertama yang Berjaya empat lejang enjin kitar Otto, jurutera dan saintis telah melakukan banyak untuk meningkatkan prestasi enjin dengan penyiasatan yang menyeluruh ke atas penyediaan campuran udara-bahan api, mewujudkan pergolakan dalam silinder, meningkatkan pembakaran tanpa lemak, siasatan ke atas pembakaran danprestasi pelepasan pelbagai jenis bahan api dan mengubah ciri-cirireka bentuk geometri enjin. Dalam hal ini, kajian permulaan nyalaan dan pembangunan telah memperolehi perhatian ramai penyelidik kerana pergantungan yang kukuh dengan aliran dalam silinder dan keupayaan untuk mempengaruhi tingkah laku penyebaran api dalam enjin pencuсuh pencucuhan (SI). Objektif kajian ini juga memberi tumpuan kepada kawasan ini pencirian api.

Kajian ini telah dijalankan dalam dua setup eksperimen berasingan. Percubaan pertama penyiasatan ciri-ciri aliran proses aruhan dilakukan pada kepala silinder enjin menggunakan sistem *Particle Image Velocimetry* (PIV). Kerja percubaan yang lain telah dijalankan dalam satu silinder enjin suntikan langsung (DI) untuk menunjukkan kesan variasi pusaran induksi pada ciri-ciri api awal pembakaran dalam gas asli termampat kurus berstrata dan kurus-homogenus (CNG) pada kelajuan enjin yang berubah-ubah. Pemasaan suntikan berubah-ubah telah digunakan untuk membuat campuran udara-bahan api homogen dan berstrata. Imej nyalaan dirakam menggunakan endoskopi dan kamera CCD. Kod komputer telah disediakan untuk mengenal pasti kuantiti aliran induksi dan ciri-ciri nyalaan

Kajian ini menunjukkan bahawa teras berpusar koheren dan teratur telah diwujudkan dan dipatuhi pada satah pusaran sederhana dan tinggi inductions sudut pusaran. Keamatan pusaran dengan pelarasan sudut pusaran yang semakin meningkat, manakala halaju RMS nilai-nilai yang menurun dengan peningkatan sudut pusaran. Mengenai pembangunan api, kadar pertumbuhan api awal adalah didapati tinggi dalam pembakaran homogen berbanding dalam satu berstrata. Dan pengambilan jatuh

jungkir-balik sederhana menunjukkan kadar pertumbuhan yang lebih baik dalam pembakaran berstrata, manakala pengambilan pusaran tinggi adalah yang terbaik dalam pembakaran homogen. Induksi pusaran sederhana dengan teras pusaran yang kuat dan padat menyebabkan kadar yang lebih rendah pembangunan api bagi kedua-dua kes pembakaran berstrata dan seragam.

TABLE OF CONTENTS

LIST OF TABLES

LIST OF FIGURES

xiv

NOMENCLATURE

General Abbreviations

ATDC	-	After Top Dead Center
BSFC	-	Brake Specific Fuel Consumption
BTDC	-	Before Top Dead Center
CA	-	Crank Angle
CAR	-	Center for Automotive Research
CCD	-	Charge Coupled Device
CDI	-	Capacitive Discharge Ignition
CFD	-	Computational Fluid Dynamics
CMOS	-	Complimentary Metal-Oxide Semiconductor
CNG	-	Compressed Natural Gas
CVCC	-	Constant Volume Combustion Chamber
DAQ	-	Data Acquisition
DI	-	Direct Injection
DNS	-	Direct Numerical Simulation
ECU	-	Engine Control Unit
EFA	-	Elliptic Fourier Analysis
FFT	-	Fast Fourier Transform
FOSP	-	Fiber Optics instrumented Spark Plug
HCCI	-	Homogeneous Charge Compression Ignition
HS	-	High Swirl
IC	-	Internal Combustion
LDV	-	Laser Doppler Velocimetry
MS	-	Medium Swirl
MT	-	Medium Tumble
Nd: YAG	-	Neodymium-doped Yttrium Aluminum Garnet
NI	-	National Instruments
PIV	-	Particle Image Velocimetry
PLIF	-	Planar Laser Induced Fluorescence

RCM	-	Rapid Compression Machine
RMS	-	Root Mean Square
RMSD	-	Root Mean Square Deviation
SCV	-	Swirl Control Valve
SI	-	Spark Ignition
STD	-	Standard Deviation
TCI	-	Transistorized Coil Ignition
TDC	-	Top Dead Center
TTL	-	Transistor-Transistor Logic
VO	-	Valve Opening

General Notations

A	-	Ampere
dB	-	Decibel
F_{bf}	-	Fuel Mass Burn Fraction
F_d	-	Flame Distortion
Hz	-	Hertz
J	-	Joule
K	-	Gladstone-Dale Constant
K	-	Kelvin
kV	-	Volt
M_a	-	Mach Number
mA	-	Milliampere
ms	-	Millisecond
MW	-	Megawatt
n	-	Refractive Index
ns	-	Nanosecond
S_g	-	Flame Expansion Rate
u	-	x-velocity component
v	-	y-velocity component
V_c	-	Convection Velocity
W	-	Watt
λ	-	Eigenvalue

λ_i	-	Imaginary Part of Eigenvalue
μ	-	Mean
μm	-	Micrometer
μs	-	Microsecond
ρ	-	Density
σ	-	Standard Deviation
σ^2	-	Variance
ϕ	-	Equivalence Ratio
ω	-	Angular Speed
ω_z	-	Local Vorticity

Chemical Symbols

CH_4	-	Methane
CO	-	Carbon Monoxide
HC	-	Hydrocarbon
NO_x	-	Nitrogen Oxide
OH	-	Hydroxide Radical

CHAPTER 1

INTRODUCTION

1.1 Motivation

Compressed natural gas (CNG) is one of the most viable alternative fuel options today. Natural gas has been used as fuel in domestic households for many years but it has not yet gained the necessary attention to be used as automobile fuel in most countries. CNG can be an ideal fuel source for vehicles for many reasons compared to gasoline.

- **Eco-friendly:** since CNG combustion produces fewer harmful emissions and hydrocarbons, it is more eco-friendly than gasoline.

- **High octane number:** CNG is considered to be a fuel with high octane number compared to gasoline. The main constituent of CNG i.e. methane has an octane number of 120, whereas gasoline has 90. Hence, knocking resistance in CNG combustion is better than gasoline so that CNG engines run quieter than gasoline engines.

- **More safe than gasoline:** CNG has a higher ignition temperature (about 580°C) so it is not dangerous. It is lighter than air so it can easily disperse into the atmosphere when leaks happen.

Currently, unavailability of filling stations relative to gasoline and size of the tanker can be disadvantages for the utilization of CNG as a fuel for mainstream vehicles. Nonetheless, researchers have done numerous investigations to enable effective use of this clean gas fuel to drive automobiles on roads.

The study of combustion characteristics and performance of compressed natural gas can be summarized into three major categories:

i. Natural gas combustion was studied in a dual fuel engine using homogeneous mixture of it and diesel spray [1], [2].

ii. Natural gas combustion characteristics were also studied in a homogeneous spark ignition engine [3], [4].

iii. Natural gas combustion was also investigated in direct injection spark ignition engine.

The Direct Injection (DI) Spark Ignition (SI) system takes the attentions of most researchers due to the possibility of controlling ignition timing and its capability of extending the lean limit by means of fuel stratification. The lean burning is found to be an attractive means of combustion from both environmental and fuel economy point of view. On practical applications, it might be difficult to combust lean fuel in SI engines. In addition to this, lean combustion has slow burning rate compared to stoichiometric or rich combustion conditions. Due to these, the lean mixture might not ignite, or the initial flame may extinguish or quenched easily by variable scale vortices. For a successful flame propagation and combustion completion, successful early flame development must be guaranteed. The appropriate level of turbulence must be created in the vicinity of the spark electrodes to obtain a self propagating and a high growth rate of early flame in the engine. However, due to the very dynamic nature of flow and combustion process in the cylinder the investigation of early flame characteristics is still a challenging work that demands multidisciplinary approach.

1.2 Problem Statement

The early flame development study in a combustion engine is very crucial to investigate the combustion performance and exhaust emission. Experimental and numerical studies on variable combustor setups utilizing various approaches have been performed by several researchers. For instance, the recent work of Aleiferies et al. [5] was done on the early flame characteristics of an iso-octane combustion in a port-fuel injection engine for a stoichiometric or near stoichiometric air/fuel mixture. Their work aimed to characterize the early flames at specific engine parameters. An earlier work of the same authors [6] was also performed on the same engine setup to investigate the effects of initial flame growth rate and ignition energy on cyclic

2

variability. References [7] and [8] depicted a flame kernel/vortex interaction in a specially designed quiescent combustion chamber. However there has been no comprehensive investigation of the early flame for direct injection CNG combustion in an actual engine. In addition, there is also gap in flame wrinkles identification and characterization technique. The conventional Fourier analysis method for flame contour characterization has some drawbacks, as discussed in [9]. These are: i) divisions should be equal on the construction of contours, ii) the method is a coordinate dependant, and iii) defining complex contours needs multi-valued function.

1.3   Objective of the Research

The main objectives of this study are listed out as follows.

i.   To experimentally investigate the early flame characteristics of a CNG combustion in a direct injection SI engine in both stratified and homogeneous combustion modes at variable engine speeds and variable intake swirl levels.

ii.   To utilize chain coding and elliptic Fourier analysis technique for the investigation of surface wrinkles, distortion and identification of mean flame contours.

iii. To investigate the level of swirl and the nature of intake flows during induction at variable swirl valve adjustment.

1.4   Dissertation Outline

This thesis comprises of five chapters. Chapter 1 discusses the motivation and introduces the research works that identifies problem which leads to the objectives. The significance of the work is also highlighted in this chapter. Chapter 2 contains extensive review of literatures on spark-ignited flame development phases and their characteristics. It also discusses in details the influence of ignition energy and flow turbulence on the early flame characteristics of a spark ignited combustion system. Previous works of researchers are also reviewed in this chapter. Chapter 3 outlines the

experimental setups and the equipments used for both flame and flow investigation experiments. The details of the methodology used and data analysis techniques are also discussed here. Chapter 4 discloses the results from the flame and flow experiments. The findings are discussed and compared with results on similar works. Finally, Chapter 5 concludes the research work and the significance of findings. Future work recommendations are also included in this chapter.

CHAPTER 2

LITERATURE REVIEW

2.1 Natural Gas Combustion and Emission

The combustion and emission characteristics of CNG and its comparison with gasoline have been the main objectives of previous studies. Comparing CNG's combustion efficiency and emission characteristics with gasoline is acceptable as the later currently dominates the consumption of mainstream automobiles and CNG application is more related to a gasoline engine (that is SI engine). Due to this, some research works have been done previously on variable combustion setups. To mention some of them, Shiga et al. [10] investigated combustion efficiency of a CNG fuel at variable equivalence ratio using rapid-compression-machine (RCM). The work examined the combustion performance and lean limit of CNG fuel in a direct injection system (with stratification) and homogeneous mix. Huang et al. [11] worked to compare the combustion characteristics of direct injection CNG and gasoline combustion over a wide range of equivalent ratio in RCM unit. They investigated a faster CNG combustion, which might be feasible for the combustion of extremely lean and stratified mixture. The same researchers in another work [12] investigated effect of variable injection timing on CNG combustion in RCM unit, and found that combustion duration decreased with decreasing time interval between injection and ignition timings. Jahirul et al. [13] compared performance and emissions of a retrofitted engine using CNG and gasoline. They mainly investigated the brake specific fuel consumption (BSFC), brake power and NO_x emission. There are more research works on this area. Most of the works portrayed that CNG can have more stable lean combustion, high lean limit via stratified combustion, less cycle-by-cycle variation, lower brake specific fuel consumption and lower emissions (except NOx, it depends on local temperature) as compared to gasoline.

2.1.1 Lean Combustion

Lean combustion is a condition related to the level of excess air relative to stoichiometric value needed to perform the combustion reaction. Level of leanness or richness of fuel/air mixture is measured using normalized value that can be appropriate for all kinds of fuel. The most common measurement units are equivalence fuel/air ratio (which is actual fuel/air ratio divided by stoichiometric fuel/air ratio) denoted by ϕ, and relative air/fuel ratio (which is the inverse of equivalence ratio) denoted by λ. The mixture is lean when $\phi < 1$ or $\lambda > 1$, and rich when $\phi > 1$ or $\lambda < 1$.

Equivalent ratio was mentioned in [14] as it is one of the important variables to determine emission levels in SI engines. Figure 2.1 shows the variation of some of the main emission gases (NO, CO, and HC) against fuel/air equivalent ratio. It shows that the leaner the mixture the lower the emission, as long as there is no misfire with further leaning. These results show noticeable benefits of lean combustion.
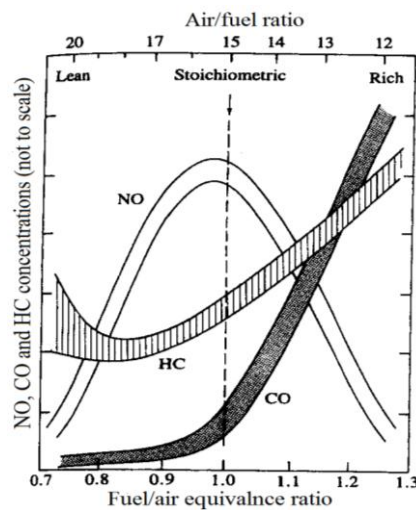
Figure 2.1 Emissions in SI combustion as function of fuel/air mixture [14]

On practical applications, it might be difficult to combust lean fuel in SI engines. In addition to this, lean combustion has slow burning rate compared to stoichiometric or rich combustion conditions. Due to these, the lean mixture might not ignite, or would rather extinguish easily or even quenched by large-scale vortices. To overcome this situation and even to extend the combustible lean limit, mechanisms should be devised to create strong initial flame kernel that can generate sustainably propagating flame throughout the combustion chamber. Techniques used previously and further

6

discussed in [15] to create such strong initial flame kernel were enhancement of turbulence generation just before ignition onset and during the combustion process, and stratification of the charge in order to create rich mixture near to spark plug at the time of ignition so that it can ignite readily than the very lean charge away from spark center.

2.1.2 Laminar Burning Velocity

Laminar burning velocity can be defined as the relative velocity of unburned gas (fuel/air mixture) that moves into the flame front and combusted in a laminar flow environment. It is an intrinsic property of a combustible fuel/air mixture (or can be considered as a physiochemical property of the fuel) that can be a useful information in engine modeling and design. Laminar burning velocity can be measured in a radially propagating laminar flame inside a closed spherical vessel at variable pressure and temperature.

Magnitude of laminar burning velocity of a fuel/air mixture depends on its equivalence ratio, unburned gas pressure and temperature. Liao et al. [16] measured the laminar flame speed of natural gas at the variable parameters mentioned, and observed that the laminar flame speed increased with temperature and decreased with pressure as shown in Figure 2.2. With regard to equivalent ratio, leaner and richer mixtures exhibited low laminar flame speeds, whereas the maximum laminar flame speed was recorded at near stoichiometric fuel/air mixture.
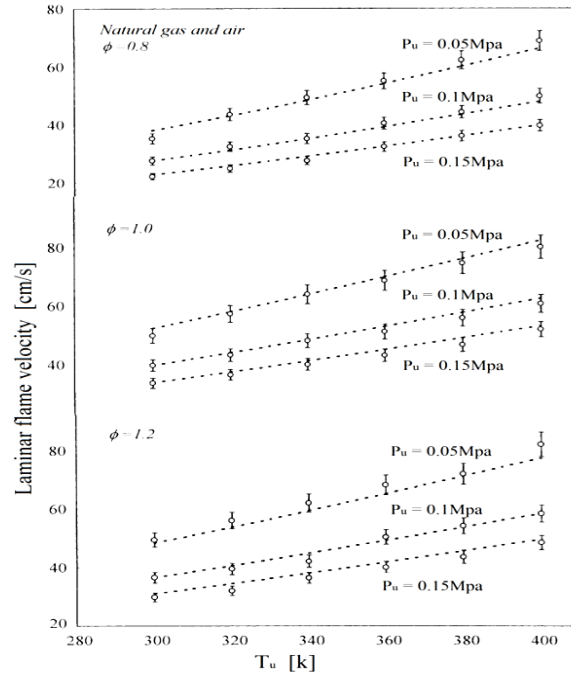
Figure 2.2   Laminar flame velocity of variable equivalent ratio natural gas as functions of pre-ignition temperature and pressure [16]

2.2   Ignition and Flame Initiation in SI Engine

In an SI engine, combustion is initiated by a spark discharge which is imposed by the electrical ignition system. The initiation and formation of self-sustaining flame kernel in combustion of such engine is composed of complex processes that can have many phases. These phases are generally categorized as the pre-breakdown, the plasma and the initial combustion phases [14], [17] and [18]. The following sections present the detail characteristics of the phase formation and completion process in the spark-ignited combustion system.

2.2.1   Ignition Process

The charge in between the electrodes of the spark plug can be considered as a perfect insulator for electrical discharge flow. With the application of high voltage from the ignition system, breakdown of the intervening air-fuel mixture occurs, and then electrons start to flood from one electrode (cathode) to the other (anode).

8

Ignition systems must provide the necessary amount of voltage within a reasonable span of time to ignite the mixture in the vicinity of the spark electrodes. The rate of voltage supply may depend on the type of ignition system used. The fundamental requirements for the ignition system to create a self-sustaining flame kernel were summarized in [14]. The requirements that must be considered are, i) the system must have enough voltage in order to break the gap resistance between the electrodes, ii) it should have enough energy storage capacity to create sufficient size ignition kernel, and iii) there should be sufficient duration of voltage release. The most common types of ignition systems commercially available are the Transistorized Coil Ignition (TCI) system and the Capacitive Discharge Ignition (CDI) system. These ignition devices provide different voltage rise time i.e. the time it takes for the coil to collapse and reach 90% of its peak potential voltage. The TCI system uses transistor switches to disconnect the coil and releases the energy it stores to initiate the spark via induction effects. The TCI system has low voltage rise, thus resulted to longer spark duration. This is advantageous to obtain a satisfactory ignition in a wide range of operating condition. As for CDI system, [17] reported that due to its high capacitive discharge, it has a spark that is strong but of short duration (10-12 μs). CDI system does not store the energy but amplifies it into a higher level. The CDI coil works just like a transformer which steps up the voltage to a higher level (typically 100:1 ratio). The voltage rise in TCI device is about 10 kV/ms, whereas CDI unit has about 100 kV/ms. The short spark duration in CDI may lead to ignition failure especially when the mixture is lean. But its quick charge time is an advantage in high engine speed condition.

When the applied voltage from the ignition system reaches a sufficient amount, the electrons rushing between spark electrodes excite and ionize the gas molecules in the gap by collision. Due to these creation of new ionized molecules, the number of electrons flowing becomes too much. Arcoumanis and Kamimoto [17] expressed this process as an avalanche of electrons with a high electron density ($> 10^{18}$e/cm^3) filling the spark gap and generating sufficiently high field strength, depending on the rate of voltage rise by the ignition system, until it breaks the intervening gas mixture between the electrodes. With the breakdown of the gas resistance, the electrons flood reaches the other end of the electrode and the impedance of the gas mixture in the gap

drastically drops. When the pre-breakdown current is in excess of 10 mA, the breakdown phase starts to occur. The current can rise to hundreds of amperes until it is limited by the circuit in the spark plug. This breakdown phase is characterized by a high voltage (as high as 10 kV), high peak current (up to 200 A) and a very short process duration, about 10 ns as shown in Figure 2.3. In the breakdown phase, the current flow confines itself within the highest conductivity region, and increases its density to produce a cylindrical channel of 40 μm diameter in the early stage of this phase [14]. Electron density increases vigorously within the channel and reaches up to 10^{19}e/cm^3 that can facilitate effective transfer of energy from the ignition coil to the channel. As a result, the temperature and pressure of the gaseous molecules in the plasma channel rises extremely, up to about 60,000 K and about 200 bars [14], [17]. Due to this extreme condition, the channel expands supersonically and a strong shock wave is emitted outwardly. Heywood [14] approximated that the loss of energy by the shock wave expansion could reach up to 30% of the plasma energy. However, since the shock waves release most of their energy within 2 mm diameter sphere of the spark center, the energy lost would be regained soon by the plasma kernel due to its fast expansion (the kernel can expand up to 2 mm diameter within 50 μs [14], [17]).
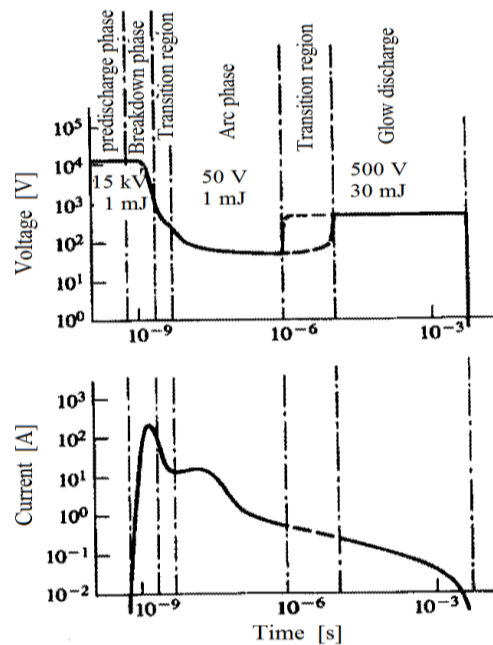
Figure 2.3 Schematic of voltage, current and energy variations in the different phases of conventional ignition system, taken from [14]

The breakdown phase is followed by the arc phase, in which electrically conductive path is created between the electrodes. This phase is characterized by low voltage (as low as 50 V) and substantially high current which can be limited by the circuit resistance of the ignition system [14], [17]. Due to the hot cathode spot requirement for the arc, erosion of cathode material is apparent (mostly Platinum and Iridium tips and pads are used to reduce erosion and corrosion). The size of the arc principally increases due to heat transfer and diffusion to the surrounding gases, and the temperature and degree of dissociation drops rapidly with increasing distance from the arc axis.

The glow discharge phase, which is the last ignition phase, is similar to the preceding arc phase unlike its cold cathode and lower dissociation level. The glow discharge phase is also characterized by its low power level (about 10 W) and due to its relatively longer discharge time, it can be the highest energy supply phase; above 30 mJ as illustrated in Figure 2.3 and discussed in [14]. Heat losses to the spark electrodes are relatively higher in glow discharge due to long discharge duration, and radiation losses are expected to be high in arc phase due to its high temperature. Energy losses and supplies of the three phases of ignition kernel are summarized in Table 2.1 .

Table 2.1   Typical energy distribution of the three phases under idealized conditions of the ignition process [17]

	Breakdown	Arc	Glow
Radiation loss	< 1%	5%	< 1%
Heat loss to electrodes	5%	45%	70%
Total losses	6%	50%	70%
Plasma energy	94%	50%	30%

Duration of the breakdown phase is extremely short, as observed on Figure 2.3, that it is hardly affected by the flow fields of its surrounding, whereas due to the longer exposure of the arc and glow discharge phases, the ignition kernel can be taken away by the flow from the electrodes gap. This eventually reduces or avoids heat losses that might happen due to the contact of the ignition kernel with the electrodes.

The required minimum energy of ignition systems can be the function of equivalence air-fuel ratio. For a lean local air/fuel mixture, the required minimum

ignition energy can be higher. Mixture equivalence ratio does not directly affect the initial plasma kernel, but the inflammation process and the inflammation thickness are greatly affected by the local air/fuel ratio. Hence, the lean air/fuel mixture demands a larger plasma kernel before inflammation becomes apparent. The works of Aleiferis et al. [6] also showed that for a given spark energy the longest discharge duration produced the highest initial flame kernel growth rate.

2.2.2 Combustion Process

Though fuel combustion starts at the very beginning of ignition, the ignition kernel expansion rate is dominated by its strong shock wave propagation and heat conduction due to its extremely high temperature and pressure condition, as discussed in [14], [17], [18]. The expansion process cools the ignition kernel to a lower temperature level. The arc and glow discharge phases bring a further cooling of the plasma, and hence temperature drops significantly. With temperature drop, combustion contribution for the plasma expansion becomes more important and it reaches a point where combustion prevails the other ways of plasma kernel expansion. Eventually, this phenomenon ends the plasma kernel phase and commences the flame kernel or initial combustion phase. Decaying effect of the plasma kernel and increasing influence of strain and turbulent flow that surrounds the flame kernel reduce its expansion rate to the minimum. Arcoumanis and Kamimoto [17] describes the early flame development stage as that for a flame radius of less than 1 mm its kernel growth is dominated by the ignition system properties. Up to the size of about 2 mm radii the balance between laminar flame speed and strain rate controls the kernel expansion rate. Gradually, the flame kernel starts to interact with the surrounding turbulent flow fields and within the size of about 10 mm radius it will acquire the property of a fully developed flame structure. The fuel fraction burned in this period can be about 10% the total mass.

The combustion process of SI engine can be categorized in three different phases according to the energy release and fuel burn rate as shown in Figure 2.4 and discussed in [14]. The first phase is the flame development process during which a

small fraction of fuel is burned (up to 10%). The flame size in this phase, especially in the early stages, is very small and highly influenced by the turbulent flow surrounding it, equivalent ratio of mixture and heat transfer due to early flame contact with spark electrodes. Design feature of insulating the spark plug might reduce heat losses due to contacts of the early flame with the cold electrodes. The early flame kernel existence can also be determined by its interaction with the level of turbulence and the vertical flows surrounding it. Kolera and Echekki [19] showed that the small early flame kernel can be completely quenched by its interaction with relatively larger core size vortices. Hence, the survival or extinction of the flame can be decided in the early stages of the flame development phase. It is also considered that the cyclic combustion variability has roots in this early stage of combustion.
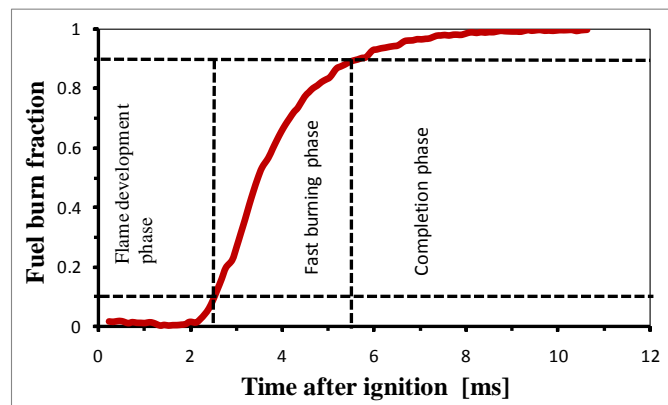
Figure 2.4   Burn fraction of a homogenous CNG combustion

The interaction of the early flame with the surrounding turbulent flow has resulted in the laminar flame to be a wrinkled laminar flame, and subsequently it grows into a fully turbulent flame. This process is schematically illustrated in Figure 2.5 . The turbulent flame then propagates at a fast rate until its expansion is limited by the combustion chamber. Up to 90% of the total fuel energy is released at the end of the fast burning phase [14]. The rest of the process will be the completion phase that might be long or may not achieved complete combustion depending on air-fuel ratio and other factors.

(a) The early flame kernel burns within an eddy in the spark plug electrod gap

(b) The flame kernel burns out from the spark gap and begins to interact with the surrounding turbulent flow

(c) The flame kernel has grown large enough to interact fully with the turbulent flow, and the flame becomes a wrinkled laminar flame
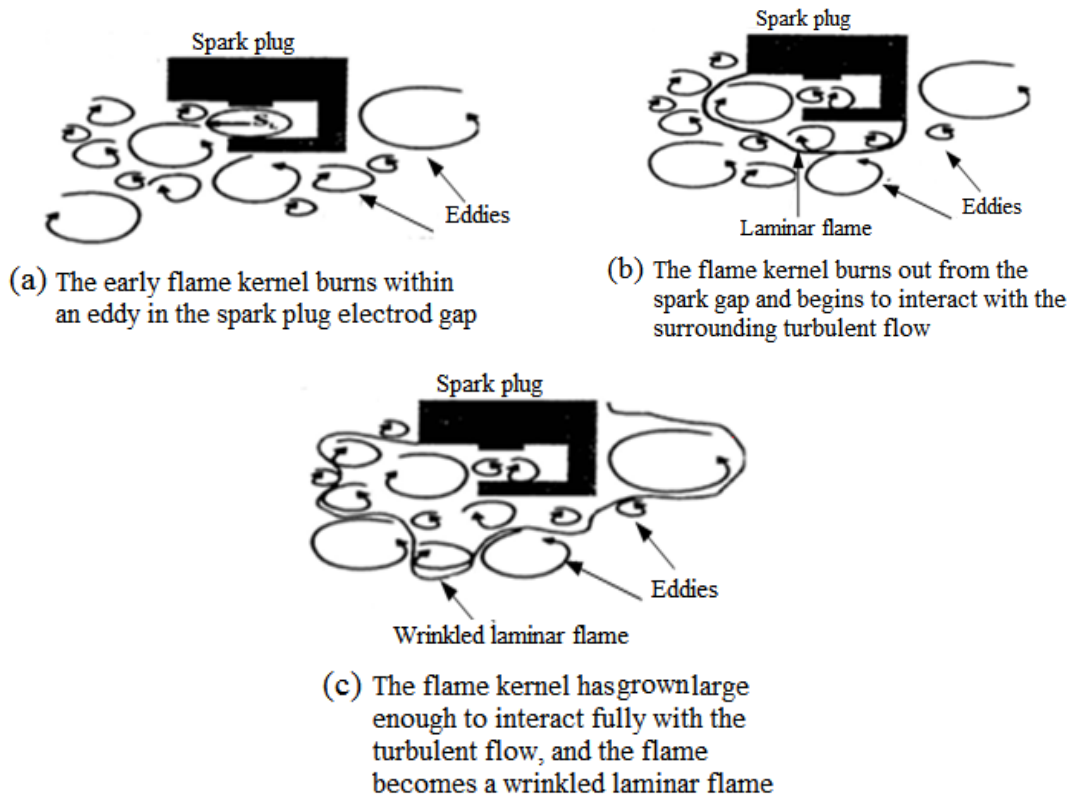
Figure 2.5   Schematics of early flame growth and its interaction with the flow in the vicinity of spark plug

2.3   Experimental Flame Visualization Techniques

Flame visualization and experimental study of flame characteristics would require imaging of the flame directly or indirectly by imaging devices. The light source for the illumination purpose can be from the flame's natural luminosity or by an external light source such as a high power laser. In simulating real engine combustion scenario, applying laser tomography method for initial flame kernels could be impractical due to the nature of flame orientation. Since the flame in the early development time can be very small in size, it can easily be convected away from the spark center by the in-cylinder flow. This random position of the flame kernel makes the attempt of capturing the early flames by a laser sheet very challenging, as also discussed in [5]. Nonetheless, the laser technique has been applied in specially designed combustors or nozzle burners (further discussed in section 2.3.3). The most commonly utilized flame study via laser techniques are planar laser-induced fluorescence (PLIF) imaging of combustion radicals (such as OH) and

two-dimensional imaging of particles based on Mie scattering. The very weak fluorescence emission from the combustion gas radicals of the small flame kernel would add further challenge on the attempt of investigating early flame kernels via PLIF imaging technique. Hence, the non-laser diagnostic techniques are widely used to visualize and study the early flame characteristics of SI engine combustion.

The most common non-laser diagnostic methods that can be used for flame visualization are; direct imaging of the flame using its natural luminosity by single shot camera or continuous video recording device, imaging the chemiluminescence signals of combustion gas radicals (such as OH, CH, C_2) and measuring flame expansion and convection speed from flame arrival time using multiple optical-fiber instrumented spark plugs.

2.3.1   Fiber-Optics Instrumented Spark Plug

Witze et al. [20] implemented eight optical fibers in a standard spark plug without any engine modification for flame kernel study for the first time at Sandia Laboratories. In 1993, similar type of fiber-optics instrumented spark plug (FOSP) was used by Meyer et al. [21] for the study of combustion phenomena under cold start and cold idle conditions. The FOSP design used by Meyer and his colleagues had no major changes from [20], but they managed to use commercially available spark plugs by taking out the electrodes and inserted it into a specially fabricated housing. On the periphery of the housing, the eight fiber optic sensors were installed symmetrically spaced in 11mm diameter ring. A sapphire window was fitted to protect the fibers from the direct heat of the combustion gases as shown in Figure 2.6 . Hinze and Cheng [22] utilized the FOSP unit to study flame kernel expansion behavior for the combustion of variable methanol and gasoline mixture fuel. Subsequent work by Ancimer et al. [23] used this modified type of FOSP to study the flame kernel characteristics in a production engine without the need of any engine modification.
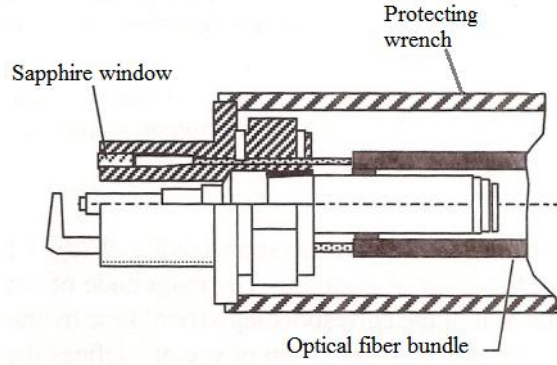
Figure 2.6   The improved design of fiber-optics instrumented spark plug [24]

The working principle of FOSP is that the light emitted by the flame is captured by the optical fibers when the flame crosses the field of view of the fibers. Then the very weak light signal is sent to a photomultiplier unit to be magnified and for the detection of its arrival time in the acceptance region. When the output of the photomultiplier after receiving the light signal exceeds the preset threshold voltage value the flame arrival times will be registered. To perform flame kernel analysis from these arrival time information, implementation of mathematical models has been a common procedure. The mostly adopted models in this area are; elliptic fit model that was developed by Kerstein and Witze [25], and cubic-spline model by Lord et al. [26]. These models are used for the construction of a 2-D flame contour based on the arrival times.

Constructing the flame contour from the arrival time recordings of each fiber optic needs some assumptions. In cubic-spline model, the radial position of the flame contour at each probe is calculated by assuming that flame front expansion rate is constant in each direction of the contour. Hence, the radial distance of the contour at each probe (R_i) at a target time after ignition onset (T_0) can be identified by the ratio of arrival time (T_i) at each probe to the target time multiplied by radial distance of the probes from the spark center (R_p),

$$R_i = \frac{T_i}{T_0} R_p \qquad\qquad (2.1)$$

Using the cubic-spline analysis technique, the 2-D flame contour can be constructed from the calculated radial distance,

$$R_L = \frac{1}{2\pi} \int_0^{2\pi} \int_0^{T_0} \dot{R}(\varphi) dt d\varphi \qquad\qquad (2.2)$$

The flame growth rate (S_g) then can be identified using perimeter based method,

$$S_g = \frac{R_L}{T_0} \tag{2.3}$$

or centroid based methods,

$$S_g = \frac{1}{2\pi} \int_0^{2\pi} S_e(\varphi) d\varphi \tag{2.4}$$

where $S_e(\varphi)$ is the expansion rate in direction φ given by,

$$S_e(\varphi) = \frac{R_m(\varphi)}{T_0} \tag{2.5}$$

and R_m is the distance from the contour centroid to contour perimeter.

The calculated flame expansion rate is a measure of average growth rate over time and direction. As for convection velocity (V_c), it can be determined from the displacement of the flame centroid from the spark center. Ancimer et al. [23] implemented both growth rate calculation techniques and they found that the centroid based flame kernel growth rate was larger than perimeter based rate.

The ellipse model, on the other hand, is based on the assumptions that i) the flame kernel is elliptical in nature with constant eccentricity, ii) the major and minor axes increase linearly with time and iii) the convection speed of the flame can be considered as constant [23]. In ellipse model, the growth rate of the flame kernel can be identified from the semi-minor axis of the ellipse, and the convection velocity (V_c) from the growth rate of the major axis of the ellipse. The graphical representation of these two models for flame kernel characterization are shown in Figure 2.7
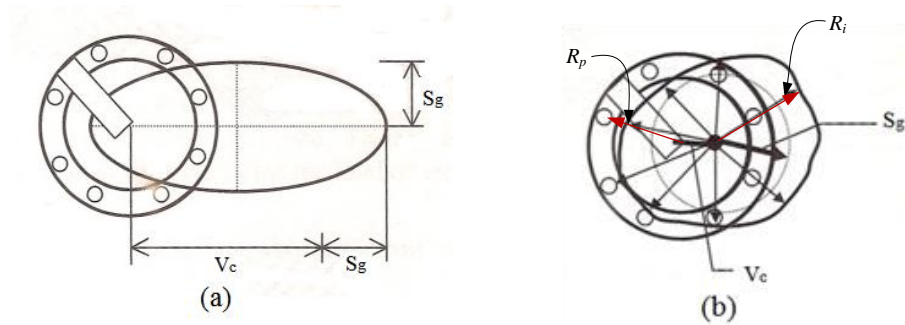
Figure 2.7   Schematics of the ellipse (a) and cubic spline (b) models for flame data analysis [23]

17

2.3.2 Chemiluminescence Measurement Technique

Chemiluminescence is defined as the emission of electromagnetic radiation as a result of chemical reaction. Some molecular radicals, such as OH, CH, C_2, can be found in a combustion gases that can emit electromagnetic radiation (or light wave) of known wave lengths. Ikeda et al. [27] measured flame propagation by imaging the chemiluminescence signals using high speed camera. They compared the direct imaging result with the local (one point) OH chemiluminescence measurement using Cassegrain optics, and were able to measure the flame thickness from the intensity level recorded by the system. In another work, Ikeda et al. [28] implemented the same technique with a three-point measurement of chemiluminescence signals to detect the local concentration of the above three radicals (OH, CH, C_2) for the combustion of CH_4. They improved the measurement by using three different techniques of spectrum analysis to convert the light signal into usable information. The first one was optical filters and photomultiplier tubes technique, in which the detected light was separated into the colors that correspond to the three radicals of interest. Then using optical filters for their respective wave length characteristics, they managed to measure the luminance intensity of the three radicals simultaneously. In the second technique they employed an optical multi-channel analyzer that was able to resolve time series spectra of flame emission in the engine cylinder. Thirdly, a monochrometer and an image intensifier were applied. From the detail analysis of the flame spectrum they detected OH radicals in the early combustion before the other combustion radical were observed, and the accumulation rate in the early combustion period was also fast for the OH radical. However, the rise in intensity of the spectral measurement with engine speed was higher in CH and C_2 molecules.

On the other hand, Fajardo et al. [29] used the OH chemiluminescence imaging to monitor flame initiation and propagation for the study of cyclic variation in SI direct injection engine. Their study was qualitative description of the processes near to the spark plug. In addition to OH chemiluminescence measurement, they employed Particle Image Velocimetry (PIV) to observe the flow pattern before and after injection and ignition, and PLIF measurement of toluene tracer particles to visualize fuel distribution in the vicinity of the spark plug. However, Ikeda et al. [27] in another

work mentioned the challenge of identifying the flame contour from the planar chemiluminescence OH measurement due to the weak signals of the combustion radical, and they faced difficulties to define flame front from the one point Cassegrain optics measurement as well.

2.3.3 Laser Diagnostics Measurement

The most common laser-dependant 2-D flame visualization technique is the Planar Laser-Induced Fluorescence (PLIF) that can be utilized by exciting some combustion diatomic molecules (mostly OH radical) using pulsed laser of appropriate wavelength and recording of the fluorescence emitted by the excited molecules on intensified CCD (charge-coupled device) or CMOS (complimentary metal-oxide semiconductor) cameras. In most cases the excitation source can be Nd: YAG (neodymium-doped yttrium aluminum garnet) laser at the absorption wave length of the combustion molecule under consideration. For instance, wavelength of 266 nm can excite OH radical and the fluorescence can be detected around 308 nm wavelength. The highest challenge in PLIF measurement is quenching of the fluorescence signal. The quenching can happen due to collision of the excited molecule with other molecules. The quenching is also directly proportional to the cylinder pressure. Since the combustion process in internal combustion (IC) engines occurs during high cylinder pressure, quenching of fluorescence signals from the excited combustion molecules is apparent.

Felton et al. [30] performed the first OH fluorescence measurement in an internal combustion engine using PLIF. They used frequency-doubled Nd: YAG laser for excitation and captured the fluorescence signal using a band-pass filter of 313 nm. The OH fluorescence was measured on a 3 cm by 3 cm field of view and spatial resolution of 0.3 mm. From the measurement, they observed the sharp rise of OH signals through the flame front, and gradual drop of it in post-combustion gas. Muller et al. [31] utilized the same PLIF technique to study flame development at variable exhaust gas recirculation ratio. They employed a high frequency pulsed laser with a wavelength of 288 nm to excite the OH radical and imaging the fluorescence of the

exited molecule at around 306 nm using UV lens and intensified CMOS camera. Bohm et al. [32] applied OH PLIF method to identify the reaction zone in their study of premixed opposed jet flame characteristics simultaneously with PIV measurement. For the OH PLIF, they employed a frequency doubled tuneable laser radiation at 281.3 nm with a field of view of 20 mm x 20 mm. However, in regard to early flame kernel visualization, the PLIF technique is very difficult to implement in an actual engine basically due to the random nature of the flame [5].

The other laser diagnostic flame study technique would be the application of a 2-D imaging based on Mie scattering principle. This technique is based on the imaging of scattered light from the seeded particles in the intake air around the burned gas region. A pulsed laser with a wavelength of 532 nm can be used for illumination of the seed particles. Since seed particles are consumed by the flame in the burned gas region, reduction in scattered light intensity can be observed compared to the unburned gas region. This variation of intensity can allow imaging of the boundary between burned and unburned gases as detailed in [24]. Pasquier et al. [33] employed PIV and PLIF techniques simultaneously to measure velocity field, fuel concentration and plotting of propagating flame front contour in a propane-air mixture combustion. The flame area was identified to be the region where seed particles were burnt out as shown in Figure 2.8. Identifying the flame contour or boundary can be challenging in this method of flame visualization.
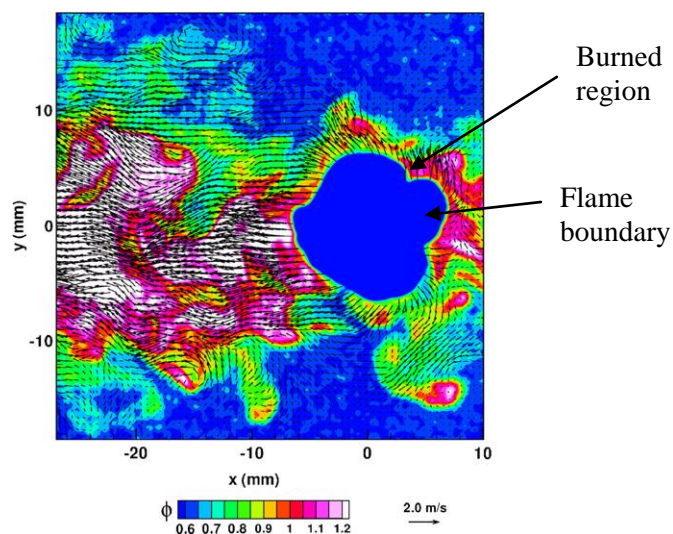
Figure 2.8   Velocity vectors (arrows), concentration fields (colored region) and flame region *[33]*

2.3.4   Schlieren Technique

Schlieren is a low cost imaging technique that has been used for many years to study the distribution of density gradients within a transparent medium. This density sensitive system has been used to create image of the fluid with variable refractive indexes. Refractive index (n) and density of fluids (ρ) might be related linearly by Equation 2.6,

$$n = 1 + K\rho \qquad (2.6)$$

where K is the Gladstone-Dale constant. The optical setup of the Schlieren system needs a high-speed camera, a spherical mirror preferably with long focal length, a light source and a knife edge or aperture to block part of the light. In most cases high intensity lamp has been used as a light source. However, employing laser as the light source can be advantageous due to its monochromatic nature and also it can increase image sharpness [24]. The quantitative evaluation of this technique is based on measurement of contrast values over the images, which can be highly influenced by noise, optical nonlinearities, diffraction and shadowing effects as discussed in [34]. The main limitations of this imaging technique are that it needs a large visualization window and it is usually only for qualitative purpose.

Some works have been performed on the qualitative visualization of flame initiation and development using schlieren technique. The works of Maly and Herweg on application of this technique for early flame development was reported in [17]. Their study was to compare the effect of two different ignition systems, TCI and CDI, on the early flame development rate of a propane-air combustion in an SI engine. It was reported from the schlieren images that the late energy supply from the TCI system was helpful to have a higher development rate especially for a lean burn condition. Recently Wang et al. [35] utilized this schlieren method to study the effect of hydrogen addition in natural gas combustion in constant volume chamber that has two transparent sides for visualization purpose. They observed qualitatively the laminar and the turbulent wrinkled flames at the different hydrogen injection strategies that were employed. The flow turbulence and the fuel stratification at the time of ignition were varied by the ignition timing variation after the end of injection

timing. The schlieren images of the flame in this work clearly showed the variations on the flame images with the variable fuel mixture preparation strategy. Miao et al. [36] used it for the study of flame propagation investigation of a natural gas/hydrogen/air mixture bomb combustion in a constant volume chamber. The application of this technique on practical IC engine is limited due to the high visualization window requirement and due to the challenge of retrieving quantitative information from the captured data.

2.3.5 Direct Visualization

Lean combustion in SI engines is characterized by its weak luminosity. Visualizing early flame kernels of a lean burn creates much more challenge due to its weak luminescence nature of the early flame. Therefore, intensified CCD cameras are very useful to capture flames of this type. A CCD camera with higher dynamic range provides a high sensitivity with a linear response for a wider range of light intensity levels [37]. A linear CCD image contains much more information than can be displayed on a computer screen or seen by the eye at one time. Hence, image processing is very important in bringing out various details of the captured weak luminescence flame images.

With the increase in technical capability of CCD cameras, image intensifiers and high frame rate video cameras, direct imaging of weak flames and analyzing them quantitatively become more apparent. The high dynamic rages of modern CCD cameras incorporated with the advancement of image processing technology maximize the capability of this flame study technique.

Figure 2.9   CCD camera and image intensifier units

Lee et al. [38] employed direct flame visualization technique via intensified CCD camera to study the effects of intake tumble/swirl combination on flame development. They identified the inflamed area and initial flame displacement from the captured flame images for comparison of the different intake effects. Aleiferis et al. [5] also employed a direct visualization of the early flame kernel using two intensified CCD cameras for imaging consecutive flames at preset crank angles in a cycle for temporal as well as spatial resolutions consideration. The earlier work of the same authors [6] also applied this direct imaging of flame luminosity for investigating spark energy variations effect on early flame growth rate. Joo et al. [39] implemented similar technique for the study of flame propagation by using high-frame rate video camera to observe flame behavior with and without swirl.

2.4   In-cylinder Flow and Mixture Formation

Details of in-cylinder flow, turbulence generation and mixture preparation were discussed in [14], [17], [40]. The large scale swirl and tumble flows formed during intake stroke have significant contribution in air-fuel mixture preparation and formation of turbulence at the time of ignition and combustion. The in-cylinder flow is basically composed of a highly turbulent flow with variable length and time scales that can be derivatives of the decomposition of the macro flow structure. The common characteristic of the flow for different kinds of engines are that it becomes unsteady because of the piston motion. In addition, cyclic variability and turbulent flow can be observed at any engine speed.

The induction process during the opening of the intake valves is one of the sources of turbulence in the engine cylinder. The intake flow generally have two flow structures when it is introduced into the cylinder; swirl and tumble as can be shown in Figure 2.10. A swirling intake is the flow which rotates about the cylinder axis, whereas a tumble flow has a rotation axis that is perpendicular to cylinder axis. In most cases practical engine induction creates a combined swirl and tumble flow condition in the cylinder. The magnitude of the generated swirl and/or tumble intake flows are highly dependent on engine geometry such as intake port design, valve geometries, bore/stroke ratio and cylinder head shape.
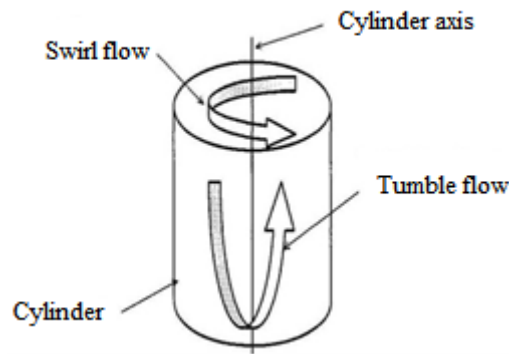
Figure 2.10   Schematic of intake flow structure in engine cylinder

The intake opening in a four-stroke engine is the minimum area for the induction such that the gas flow has the highest velocity at the valve during the intake process. The gas which flows into the cylinder as a conical jet has a high axial and radial velocity components that can be about 10 times of the mean piston speed as mentioned in [14]. The evolution of turbulent in the intake stroke and in the compression stroke was discussed in [41] and the schematic is shown in Figure 2.11. With the continuous valve lift, the turbulence energy increases starting from the valve opening. This can be sources for the turbulence created in the cylinder. Basically, in a turbulent fluid flow, viscous shear stresses perform deformation of fluid layers, and the break-up of eddies convert the turbulent kinetic energy into internal energy of the fluid in an energy cascade process [42]. This makes turbulent flow always dissipative, and so unless otherwise there is a continuous source of energy to generate turbulence, it eventually decays. The turbulent energy starts to decay even before the inlet valves closed as discussed in [41]. Nonetheless, the decaying rate is very much dependant on the intake flow structure. Due to the favorable geometry of the cylinder, the swirling structure of the in-cylinder flow experiences a lesser rate of viscous dissipation than the tumble structure. Hence, the energy of a swirling intake can be preserved longer during compression process compared to tumble flows [40]. In practical engine, the intake flow structure can be complex depending on the position of the intake valves, intake port geometry and the swirl angle. Fuel direct injection, especially during compression process, can have its own impact on the in-cylinder turbulence variation.

24
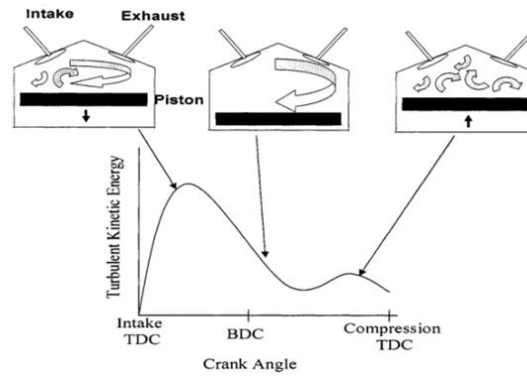
Figure 2.11   Typical representation of turbulence in the cylinder during intake and compression process [41]

There are different mechanisms to create a swirling intake into the engine cylinder. Modifying the intake valves to be shrouded to one side or masking cylinder head around the valve periphery so that the flow will be discharged into the cylinder tangentially in a side way deflection manner [14] or applying swirl control valve (SCV) in the port that employs adjustable butterfly valves to vary swirl are the most common techniques. Shrouding of the intake valves is not a good choice for swirling flow generation due to its negative effect on volumetric efficiency. In modern research engines SCVs can be used to produce swirling flow at the valve stem inside the port. This kind of SCV is advantageous to create different levels of swirl intake without changing or modifying the intake port. Application of helical ports is also able to create swirling intake flow inside the port before it is introduced into the cylinder [14], [43].

On the other side, the level of tumble induction can be varied by varying the entry angles of the port. Lee et al. [38] used tumble induction at three different port entry angles (15°, 20°, 25°) to study the effects of tumble strength on combustion. They found that tumble generated turbulence was best at 20° port entry, and this was found to enhance lean burn performance.

During compression process the intake flow structures are subjected to significant change by decomposition of the large scale flow into smaller scale turbulent eddies. Heywood [14] discussed this process that an increase in turbulent intensity due to compression and combustion was noticed toward the end of compression stroke in some in-cylinder flow patterns. With the compression of the large scale flows, angular

velocity increases to conserve angular momentum. This phenomenon generates turbulence due to shear flow.

The other important flow structure created during compression process is squish flow, which can be defined as radially inward flow that occurs toward the end of compression process when the piston approaches TDC [14]. Zhao et al. [40] highlighted that squish flow can enhance a swirl in-cylinder flow and increase turbulence intensity in the early portion of the combustion period.

2.5 Early Flame Development in SI Engine Combustion

Flame kernel development period is the time over which the initial flame kernel burns from the spark gap and begins to interact fully with the turbulent flow field. This portion of the combustion process corresponds to a 10% mass fraction burned period [5], [6] and [44].

As discussed in Section 2.1.1, the expansion of ignition kernel is controlled by its supersonic shockwave propagation and conduction due to its extreme temperature and pressure. Gradually, the significance of combustion on plasma kernel expansion increases and the thermo-chemical and flow properties of the fluid near the spark plug become the governing factors of flame kernel development. The combustion reactions at this stage are then sufficiently powerful to lead the expansion of the kernel without supplementary energy supply from the spark plug.

2.5.1 Modeling of the Early Flame Kernel

Many techniques were used in the attempt to model the initial combustion phase and the flame development characteristics. The most common models used are zero-dimensional model, quasi-dimensional model and multi-dimensional model. The zero-dimensional model is based on energy conservation and thermodynamic laws, and it does not involve the flow field analysis. This model can be considered as a low level modeling of combustion in SI engines [45]. The quasi-dimensional model involves the consideration of spatial dependence into combustion and heat transfer explicitly,

and it is capable of relating the model outputs to the combustion chamber geometry and flow field parameters. The multi-dimensional model, on the other hand, involves solving of the Navier-Stokes equation and it can directly relate the details of flow and combustion processes in the cylinder. Currently, the quasi-dimensional model has been used most frequently in SI engine simulation than the multi-dimensional model [45], [46], [47]. Quasi-dimensional model can reasonably connect flow and combustion with engine geometry and predict engine performance and emissions satisfactorily. Its computation time and computer resource utilization are also better than the multi-dimension model which depends in most cases on computational fluid dynamics (CFD) codes such as KIVA. Hence, the quasi-dimensional model is believed to bridge the zero-dimensional and the multi-dimensional models. The zero-dimensional model is hardly used due to its incapability to relate combustion with the in-cylinder flow and the geometry of the combustion chamber.

Willems and Sierens [18] utilized the mass and energy conservation principles to model the initial combustion process and characterize flame kernel growth rate. Setting the initial condition for the initial combustion model was a challenge that needs determination of the moment of transition between the plasma phase and the initial combustion phase. Practically, those two phases demonstrate different expansion characteristics. As discussed earlier, the plasma expansion is dominated by shock wave and series of diffusion expansions, and it is characterized by supersonic expansion process, whereas flame expansion as a result of combustion is a subsonic process. Hence, the modeling strategies of these two processes are different and the output of the former will be the initial condition for the later. Willems and Sierens [18] set the transition stage between the two phases via the amount of adiabatic flame temperature. When the kernel average temperature reached threefold of the adiabatic flame temperature, they noticed that the Mach number of the plasma expansion equaled to unity (Ma = 1). This condition starts to signify the combustion contribution on flame expansion process. They compared their one-dimensional model result with experimental work done by schlieren visualization. Heywood [45] used the quasi-dimensional modeling approach to characterize flame kernel properties, which was achieved through flame structure and flame speed sub-models. The sub-models were

27

used to identify the turbulent flame thickness, mean flame contour and the laminar and turbulent flame speeds.

2.5.2 Effect of Ignition Energy on Flame Kernel Formation and Growth

Energy supplied by spark plug also shown to have influence on flame development rate. High spark energy is mostly associated with low supply duration. As discussed in Section 2.1.1, the voltage rise rate for the two ignition systems which are known as TCI and CDI are about 10 kV/ms and 100 kV/ms, respectively. Aleiferis et al. [6] related spark energy duration with flame growth rate in a cyclic combustion base for a given spark energy that the one with the longer energy supply of the ignition system demonstrated a better growth rate than the average flame development rate. Arcoumanis and Kamimoto [17] strengthen the same idea by elaborating the benefit of a continued late energy supply by the ignition system specially for a lean local mixture using TCI ignition system. They showed the schlieren images of the early flame kernels employing both TCI and CDI ignition systems for stoichiometric and lean air-fuel ratios. Their result showed that at a similar observation time, the flame size of the lean TCI system was larger than the CDI system. However, for the case of stoichiometric combustion the early flame sizes produced by the two ignition systems showed no differences. This shows that flame kernel created by lean mixture can be weak unless supported by longer ignition energy supply system. Song et al. [48] compared ignition energy level and mass fraction burn rate or combustion rate in a constant volume combustion chamber by varying the dwell time of 1.5, 2.5 and 3.5 ms (the time in which the primary ignition circuit becomes on-state and stores ignition energy at coil and capacitor). They measured an increase in mass burn rate and heat release rate with ignition energy rise, because ignition energy increases with dwell time.

2.5.3 In-cylinder Turbulence and Early Flame Interaction

Flame growth rate in the early development stage is highly influenced by in-cylinder flows surrounding the flame, and the quality of the combustion cycle can also be determined within this short duration of combustion after ignition onset [5], [6].

The cylinder bulk flow which surrounds the spark electrodes at the time of ignition consists of variable turbulent scale eddies. The constituent depends on the macro structure of the intake flow (tumble or swirl), and the magnitude of squish flow generated during the compression process as well. Ting et al. [49] basically compared effect of low frequency large eddies and high frequency small scale eddies on the early developing flames. They related the high frequency small scale eddies effect as a flame-turbulence interaction that can affect combustion rates in the early portion of combustion period, whereas the low frequency large scale eddies could be related to the flame-electrodes/wall interaction that might reduce the early flame size by quenching. They found a high correlation between the high frequency small eddy turbulence at the time of ignition and the flame growth rate. The large scale eddies (eddies larger than flame size) and bulk flow were found to convect the small flame away from spark electrodes. Xiong et al. [7] performed experimental investigation to study the interaction between flame kernels and vortices. The outcome of their investigation was that the vortical flow enhanced flame growth rate highly as it interacted with the early flame (when the flame was considered to be very small). In addition, they found that the vortex strength had significant impact on the early flame growth than the vortex size. On the other hand, Aleiferis et al. [5] showed initial flame growth and wrinkles relations that seemed contradicting with the other works of small scale flow effects on growth rates, such as the works of [49]. However, their study demonstrated the beneficial effects of flame convection in the earliest time due to mostly by the large scale flows and the bulk mean velocity.

Relationships of early flame characteristics with vortical flows near to spark plug were investigated by some researchers experimentally and numerically. Xiong and Roberts [50] investigated the interactions of a vortex toroid by varying equivalence ratio of the core fluid with a flame kernel ignited at a specific equivalence ratio (0.6). The study showed that the consumption rate of the vortex toroid by the flame kernel

depends on the equivalence ratio of the core fluid of the vortex; faster consumption rate with higher equivalence ratio. This would increase the growth rate of the developing flame. Earlier, the same researchers investigated the variable size and strength of laminar vortex effects on flame stretching and the eventual rise in combustion rate [7]. They showed that a threefold rise in flame growth rate was noticed with a vortex interaction of the early flame than without the interaction. On another study of flame kernel-vortex interaction via 2-D direct numerical simulations (DNS), Kolera-Gokula and Echekki [19] illustrated that a strong large vortex can cause flame kernel global extinction. The study was deliberately performed in two interaction regimes i.e. the early-time interaction and the later-time interaction regimes. In the early-time interaction regime a vortex pair with a core size larger than the flame kernel interacted with the kernel and the result showed a global or local extinction of the small flame kernel while, in the later time interaction of the vortex pair with a larger size flame kernel yielded wrinkling effects on the flame front. It was noticed in this study that the flame was stretched and growth rate increases depending on the translational speed of the vortex pair towards the flame in the later regime. Maley et al. [51] also investigated similar flame kernel-vortex interaction processes at varying kernel size and equivalence ratio. They found that when a vortex was interacted with a 5 mm radius (small) flame kernels the result showed that there was a substantial rise in burning rate for a lean mixture; whereas burning rate decreased for the rich mixture. However, the vortex interaction with a larger flame size, 30 mm radius, resulted in a moderate flame growth enhancement for both lean and rich mixture due to flame front wrinkling effects. They did not record any flame quenching due to its interaction with large vortex cores as it was identified in [19].

The lean burn flame characteristics upon variations of turbulence properties via intake swirl/tumble strategy was investigated by Lee et al. [38]. For their study, different port entry angles were used to generate tumble-caused turbulence on a port fuel injection engine with spark plug located vertically on the cylinder axis. They varied the intake tumble strength and identified the turbulence level using LDV (Laser Doppler Velocimetry) and captured flame images using intensified CCD camera. With the most effective tumble entry angle (in terms of turbulence generation and burn rate) they inserted a swirl control valve in the intake port so that a combined

tumble-swirl flow could be introduced into the cylinder. This combined intake flow was found to be more effective in regard to flame development rate coupled with flame convection than pure tumble.

2.6 Summary

Earlier works devoted on the interaction of early flame with turbulent flows of variable scales or the nature of early flame growth with ignition energy variations. Most of these experimental studies were conducted in a rapid-compression-machine (RCM) unit, constant-volume combustion chamber (CVCC) unit or in a specially designed unit to generate size and strength controlled vortices. RCM unit is most appropriate to study single cycle combustion properties in HCCI and stratified combustion. It fails to consider intake swirl level and mixture contamination by previous cycle, for instance. Generally, this unit would be prepared to create more favorable condition for single cycle combustion than the real engine. On the other hand, CVCC units are mostly used to investigate laminar burning velocities of different fuels or to study effects of ignition energy on flame development by excluding the turbulence effects, as its combustion process is undertaken in a quiescent environment.

In relation to early flame study, the works of Aleiferis and his colleagues [5], [6] were the most related to real engine situation than any other works. However, their work was concentrated on the characteristic study and property quantification of early flame rather than the study of character change of the early flame (or its response) with change in engine parameters (such as engine speeds, induction swirl variations and stratification levels). The study also conducted in port-fuel injection with isooctane fuel combustion. Hence, there is still gap of study for other fuel types (such as CNG) that involves the variable engine parameters, and investigating the early flame response for the change of parameters.

The appropriate mathematical tools to retrieve important quantitative information from flame images are still also under study. There is no singled out tools to identify

the different flame contours, to measure levels of wrinkles and distortion. Therefore, the analysis techniques can be an area of opportunity for further investigation.

Hence, the current study aimed to investigate the characteristics of the early flame in an engine which is accessible only by endoscopes and with the consideration of engine parameters change. The flame analysis technique that was considered in this study also followed different approach from the previous ones. It involved chain coding, Elliptic Fourier analysis procedure and other image processing techniques such as thresholding and boundary tracing.

CHAPTER 3

EXPERIMENTAL METHODS AND ANALYSIS TECHNIQUES

3.1 Equipment for Flame and Flow Visualizations

3.1.1 Optical Engine

The engine used for this study was a single cylinder direct injection engine available in the Center for Automotive Research (CAR) lab in the university. This research engine was redesigned and modified by Orbital Engine Company (Australia) to be an optical direct injection for compressed natural gas combustion, hereafter identified as CNG DI, with a compression ratio of 14:1. It consists of two intake and two exhaust valves that are actuated by overhead camshafts, one for each set of valves. The engine specification is detailed in Table 3.1 and shown in Figure 3.1.

Table 3.1   Basic engine specification

Number of cylinders	One
Number of valves	Four
Displacement volume	399.25 cc
Cylinder bore	76 mm
Cylinder stroke	88 mm
Compression ratio	14:1
Size of optical access (endoscopic)	10 mm (diameter)
Exhaust valve open	135 ATDC
Exhaust valve closed	10 ATDC
Intake valve open	12 BTDC
Intake valve closed	132 BTDC

There are two types of pistons available with engine. Since the engine is a direct injection type, stratified combustion can be an important application of it. According to this, the pistons are categorized as stratified and homogeneous combustion pistons

as shown in Figure 3.2. Their category is according to the size of the bowl on the piston crown. The piston with a large eccentric bowl is used for stratified combustion, and the one with a smaller bowl for homogeneous combustion.
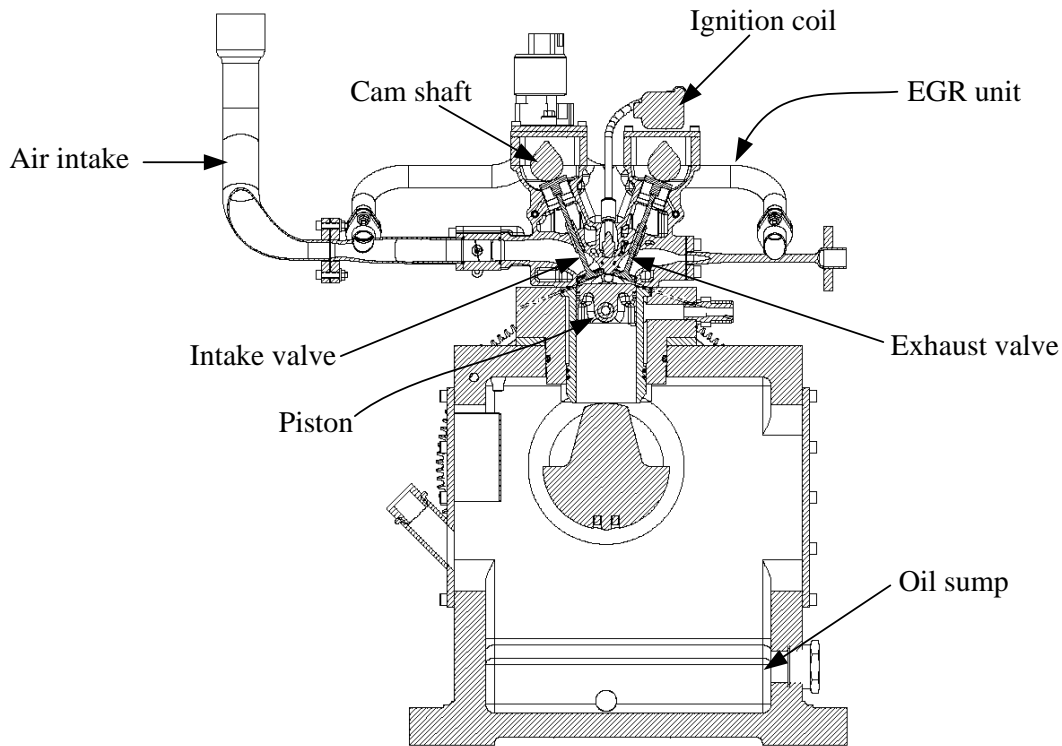
Figure 3.1   Schematic of the CNG DI engine

This CNG DI engine can be considered as an optical engine which has optical access for the visualization and study of in-cylinder processes. Though limited to a single viewing plane, there are two main accesses into the interior of the engine cylinder, namely endoscopic view and optical window view.

(a)   (b)
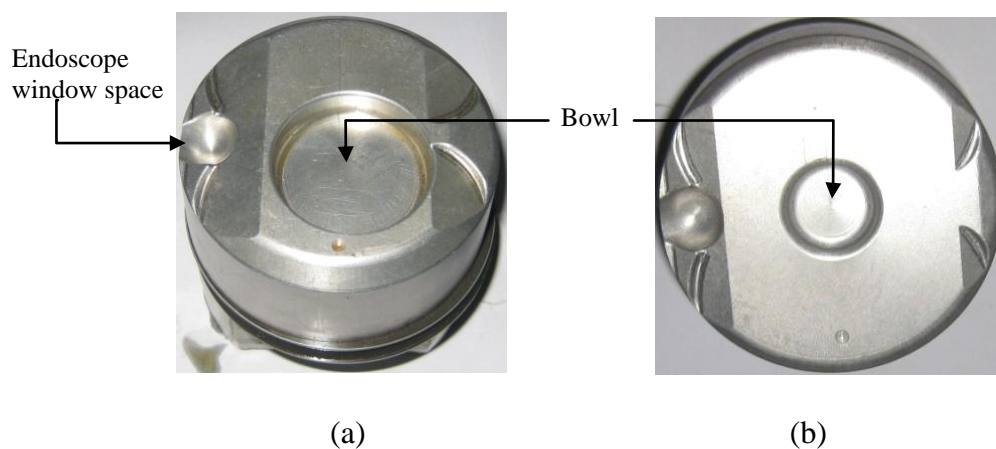
Figure 3.2   Types of piston (a) stratified (b) homogeneous

34

3.1.2   Fuel Injection System

The injection system consists of a high pressure CNG storage tanks (about 200 bars), pressure regulator, flow meter, fuel rail and injector. The pressure regulator is used to adjust the high pressure CNG gas down to injection pressure (that is 18 bars for the current high pressure injector). The Software in the Engine Control Unit (ECU) controls the CNG DI system including injection timing in respect to the crank angles and injection duration according to the desired air/fuel ratios. The composition of the CNG fuel used in the experiment is summarized in Table 3.2

Table 3.2   Typical composition of CNG in Malaysia [52]

Component	Symbol	Volumetric %
Methane	CH_4	94.42
Ethane	C_2H_6	2.29
Propane	C_3H_8	0.03
Butane	C_4H_{10}	0.25
Carbon dioxide	CO_2	0.57
Nitrogen	N_2	0.44
others	H_2O & others	2.00

3.1.3   Ignition System

The ignition system is composed of the DC power supply, ignition coil and an M12 spark plug. Special metals are embedded on the surface of the spark plug electrodes to avoid corrosion and melting of the electrode surfaces that can have contacts with the extremely high temperature plasma arc. These special metals are Iridium alloy tip for the central electrode (the cathode) and Platinum pad for the side electrode (the anode) as shown in Figure 3.3.
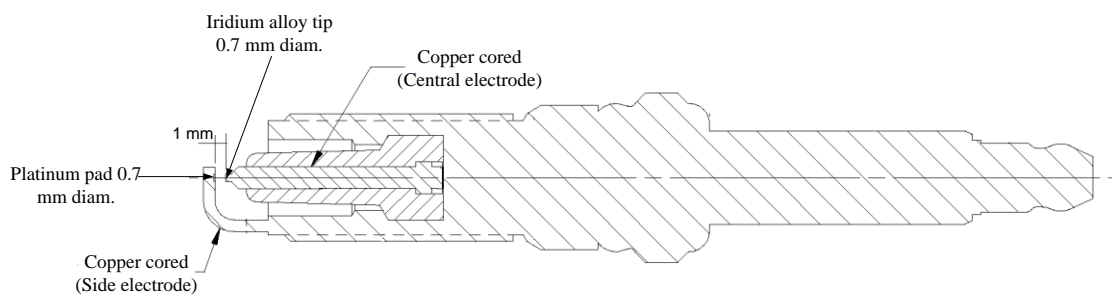
Figure 3.3   Schematic of the spark plug used in the experiment

3.1.4 Endoscopes

The current CNG DI engine combustion chamber can be accessed by endoscopes for viewing and illumination, and it can be named as camera and light (laser) endoscopic access, respectively. These access lines, which have 10 mm bore diameter, are orthogonal to each other. The arrangements of the endoscopic access lines are shown in the schematic of the engine assembly in Figure 3.4. The camera endoscope access sleeve is installed at 30° from the horizontal in between the two intake valves. The AVL KARL STORZ endoscope itself has a 30° steering angle to obtain the vertical plane on focus, and it has a divergence angle of 67°. The endoscope is equipped with cooling line using compressed air at 6 bars to avoid image distortion due to high temperature working conditions, such as flame imaging during combustion process, and combustion chamber window to protect the direct contact of endoscopes and flame, shown in Figure 3.5.
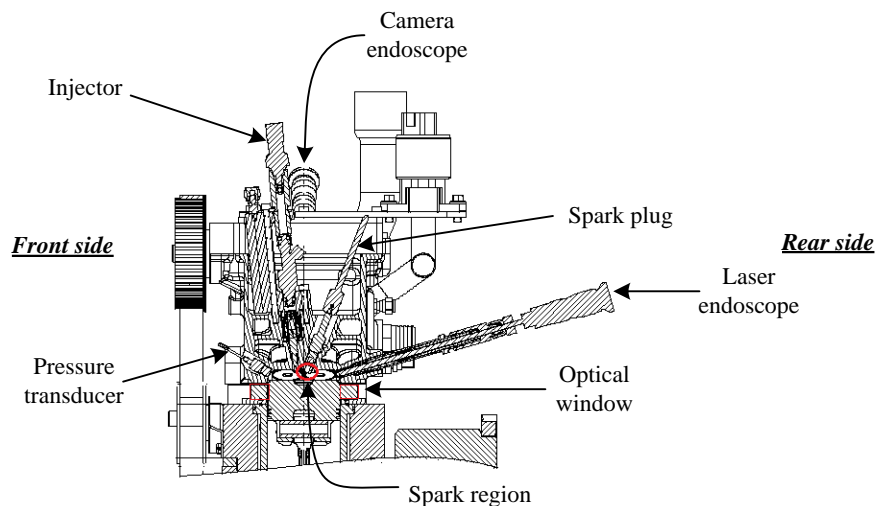
Figure 3.4   The CNG DI engine with the optical access

On the other hand, the light sheet endoscope was placed orthogonally from the camera endoscope (on the rear side of the engine assembly, Figure 3.4) and at 16° installation angle from the horizontal plane. It has 26° divergence angle and 0° steering angle. Both endoscopes are provided with sleeves and round ended combustion chamber windows.
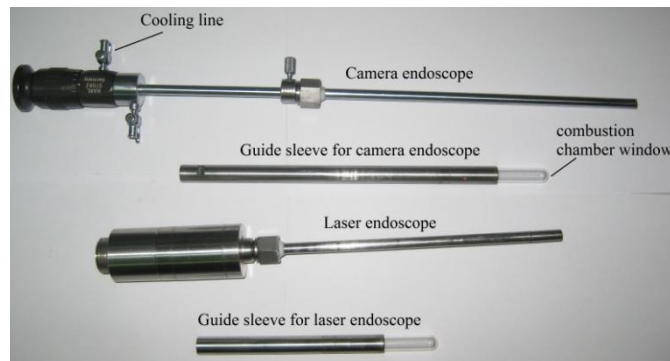
Figure 3.5   Endoscopes and guide sleeves

3.1.5   Imaging Device

Charge-Coupled Device (CCD) camera was utilized in this study of flame and flow visualization. It is identified as a 12bit 80C60 HiSence PIV/PLIF camera. The camera is equipped with a 60 mm Nikon lens and Hamamatsu CA2098 image intensifier. Image intensifier is a compulsory tool to magnify the intensity and increase the gain of the weak luminescence of the flame to be captured. With the endoscopic visualization process, the 60 mm Nikon lens is not applicable. Instead R. Wolf having 27 mm fixed focal distance lens was employed. This lens has also a device to grip the endoscope in one side and a threaded part to be fixed to the camera or image intensifier on the other side as shown in Figure 3.6. The 60 mm Nikon lens was utilized only for PIV applications for the investigation of intake flow structures.

Figure 3.6   Flame imaging camera assembly

The CCD chip in the camera is a type of progressive scan interline with 1280 x 1024 pixels. The chip has vertical drain overflow diodes that can provide efficient anti-blooming allowing up to 1000 times overexposure. The camera has a high

dynamic range quality, which is greater than 60 dB, that can provide a high sensitivity for a wider range of light intensity levels. This makes the CCD camera to be utilized for the visualization of weak luminescence flame images at the cost of image processing programs. The other important feature of this camera is its capability of double frame recordings. This double-frame recording is a very powerful mode of operation for cross correlation PIV processing. It is still possible to switch into the single-frame mode of operation when it is necessary, such as in the process of auto-correlation in PIV and general image capturing in the case of flame imaging. The maximum frame rate of the camera in the single-frame mode of operation is only 9 Hz, which is going to be half of it in double-frame operation. When the camera is working in a double-frame mode of operation, it will capture two images for a single shot. The time settings of the two frames are limited by the camera capabilities. The second frame is exposed to light at a much longer period than the first frame. The first frame integration time is variable and yet limited to a minimum integration timing of 132.1 µs, whereas the second frame has a fixed integration time of around 110 ms. When the camera is working under a continuous wave laser or room light the second frame will be brighter than the first due to its longer exposure to light. In that case lenses at appropriate wavelength should be used or the experiment should be performed in a dark room. In most practical case applications (such as PIV or PLIF systems) laser pulses will be used. In such case there should be a timely synchronization between camera frames and laser pulses as shown in Figure 3.7. If necessary (for instance, in IC engine) the camera shot and laser pulses can be synchronized with the process. This can be effective by producing a signal from the process to trigger the data acquisition system (the camera and/or laser system).
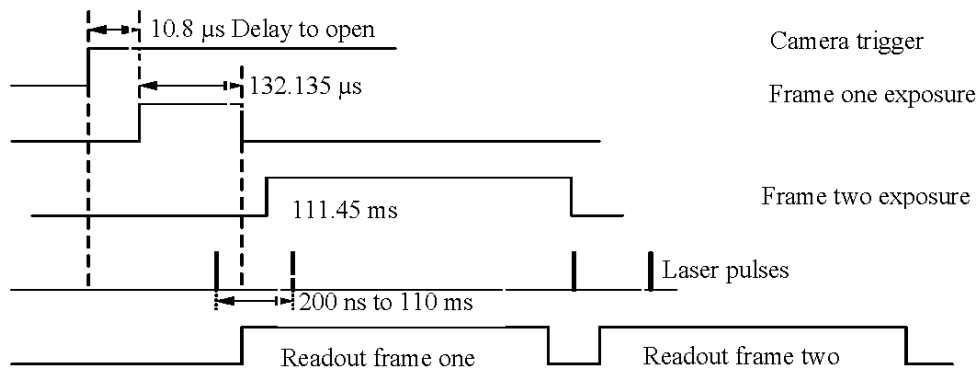
Figure 3.7   Double-frame camera timing and Nd: YAG laser Q-switch pulse firing for cross-correlation PIV data acquisition

3.1.6   Illumination System

High power pulsed laser is a very common illumination system in PIV applications. For the PIV experiment in this study, the New Wave research product of a Q-switched double-pulsed Nd: YAG Gemini 200 laser was utilized. This laser generator has a maximum repetition rate of 15 Hz. It consists of two laser heads responsible for the emission of the two laser pulses (Figure 3.8). The primarily emitted laser is an infrared radiation of 1064 nm wavelength. Since photographic films and CCD cameras are more sensitive to blue/green spectrum the infrared radiation of the laser will be frequency doubled using the second harmonic generator to get the 532 nm green radiations, or a four-fold increase of the frequency using the forth harmonic generator to get the 266 nm ultraviolet radiation. The 532 nm green light is the most applicable in PIV imaging. The Nd: YAG Gemini 200 15 Hz laser generates green light wavelength having laser energy of 200 mJ. In the experiment, the pulse width was set at 10 μs that gave each pulse a power of 20 MW. The summarized specification of the laser is given in Table 3.3.
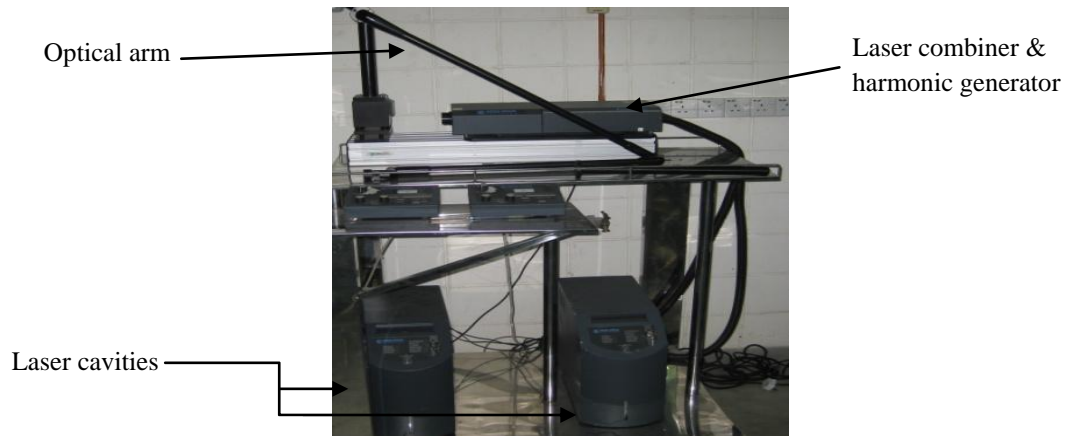
Figure 3.8   The laser system

Table 3.3   Basic specification Gemini 200 Nd: YAG dual head laser

Repetition rate (Hz)	15
Energy (mJ) @532 nm	200
@355 nm	45
@266 nm	40
Pulse-to-pulse energy stability ($\pm\%$)	
@532 nm	5
@355 nm	7
@266 nm	8
Beam diameter (mm)	5.5
Pulse width (ns)	$3 - 5$
Divergence (mrad)	< 2
Beam pointing stability (urad)	< 200
Jitter ($\pm$ns)	0.5

3.1.7 Seed Generator

Velocity and turbulence analysis of fluid flows using PIV system requires seeding of the flowing fluid with appropriate seed particles. In actual sense, the PIV system is used to measure the velocity of the particles in the fluid. Therefore, there should be some criteria expected from the seed particles in order their flow might represent the velocity of the fluid. The particles used as PIV seeding must be able to follow the

flow, must have a good light scattering capability, should be compatible with environment and health codes, should have non-corrosive and non-abrasive characteristics and convenient to generate. Their size should be small enough to track the flow and large enough to scatter sufficient light to be detected by the CCD camera.

The selection of seeding device is based on the choice of appropriate seeding material for a specific experimental setup. Generally, for gaseous flows solid and liquid seeding particles can be used and for liquid flows solid seed particles can be applied. For the current air flow application, olive oil micro-bubbles (particle size 1 μm peak in PDF size distribution) was used as seeding particles; and the seeding device selected was the Laskin nozzle aerosol generator shown in Figure 3.9.
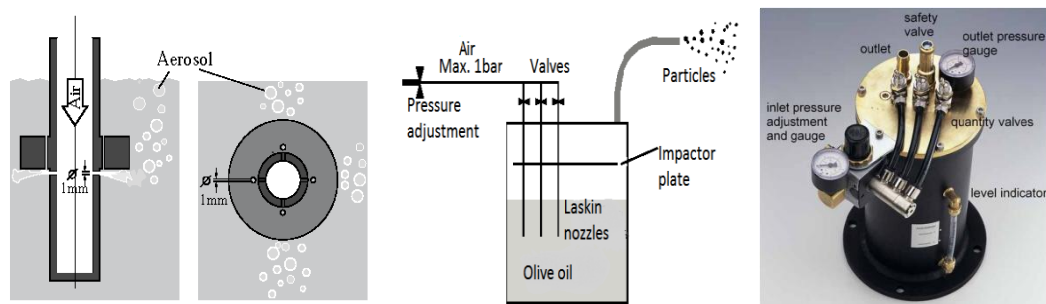
Figure 3.9   The Laskin nozzles seed generator

3.2   Cylinder Head Assembly for Intake Flow Characterization

The level of swirl during induction was investigated in a separate setup outside the engine due to the inaccessibility of swirling flow data in the engine cylinder. The detail experimental setup, flow data collection procedure and analysis techniques are discussed in this section.

3.2.1   Experimental Setup

In-cylinder flow is composed of highly turbulent flows with large number of length and time scales. These flows are very unstable due to the swirling and tumbling induction and piston motion. Hence, cyclic variability is apparent and turbulent flow can be observed at any engine speed. When the intake flow separates from the valve seats it produces shear layers with velocity gradients and recirculation patterns [14].

41

This occurrence has the capability to generate high level of turbulence in the engine cylinder.

The intake port of the engine was originally designed for a tumble intake flow generation capability. Later on, it was modified by inserting two butterfly valves in the divided port to create and vary swirling motion of the induction air via valve closure angles. This valve is known as swirl control valve (SCV)

The CNG DI single cylinder engine has an endoscopic optical access for the in-cylinder process measurements. Regarding early flame investigation, endoscopic access can be used (perhaps the only option) to obtain flame information from the combustion chamber. However, the investigation of in-cylinder flow and turbulence was very difficult on the existing engine due to lack of visualization range when endoscopic system is used. Hence, another technique had to be devised to visualize and analyze the air flow characteristics and swirl level as it was introduced into the cylinder.

The new setup consist of the actual engine cylinder head, an optical cylinder liner made of acrylic glass of 3 mm thick having the same dimensions as the actual engine cylinder, a mirror setup at 45^0 for swirl plane visualization through the bottom of the cylinder, a metallic structural frame to support the head and the cylinder, a blower for air supply and PIV system for data acquisition and analysis, as shown in Figure 3.10.

The PIV system is a whole field velocity and turbulence measurement technique that traces the motion of seeded particles in the flow. This flow measurement system requires a thin slice of the flow field to be illuminated by a laser light sheet. In the current study the illumination source was a frequency double-pulsed Q-switch Nd: YAG laser. The light was directed into the optical cylinder using an optical linkage arm and lenses to get a laser sheet. Particles in the flow within the light sheet scatter the light. A CCD camera placed at the right angle to the light sheet detects the scattered light and stores the data for further processing.
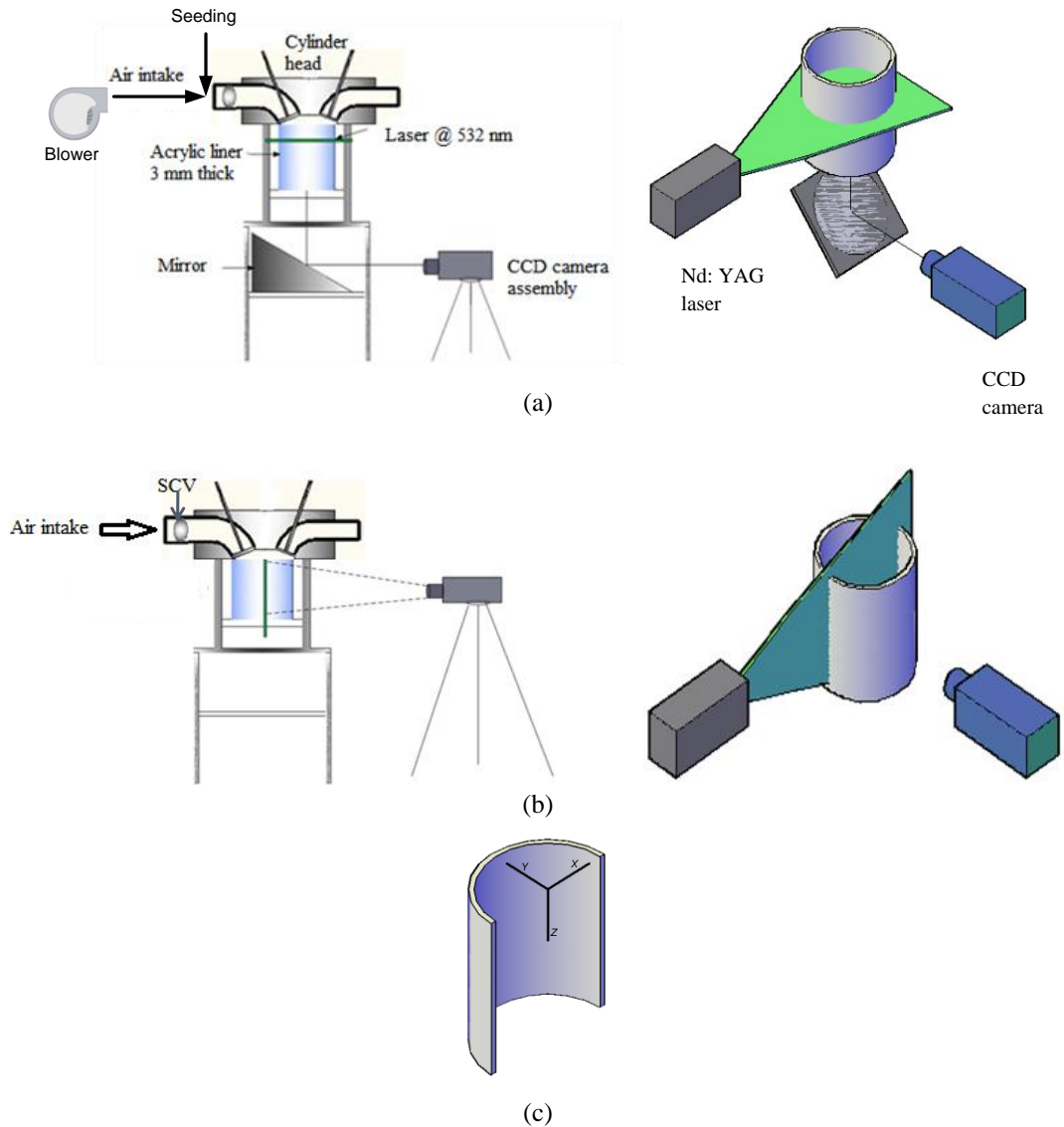
Figure 3.10   Setups for (a) swirl plane PIV imaging, (b) tumble plane PIV imaging and (c) flow coordinate axes in the cylinder

3.2.2   Intake Flow Analysis Technique

The analysis of flow behaviors during induction on this new setup for the variable induction strategy was accomplished by varying the valve openings at different valve lifts. A valve locker was fabricated and used to maintain the opening at the variable valve lift positions. When the valve reaches the maximum opening position, it was measured to be 7 mm for the lift from the seat. Therefore, the valve opening was divided into seven hold points so that flow data could be captured every 1 mm lift. The procedure was first to set the valve lift (from 1 mm to 7 mm, every 1 mm

increase), then varying the swirl control valves (SCV) closure angle and capture PIV images on the swirl planes (two swirl planes i.e. near to valve seats and midway in the cylinder) and tumble plane as well.

For this study, three swirling intake conditions were considered by closing the SCVs at varying angles. The starting point of the induction strategy was at 10° close up of both SCVs to introduce an inclined tumble intake into the cylinder (not purely tumble due to the 10° closure of the swirling valves). This can be taken as Case-I induction. The next induction strategy was to set one of the SCVs at 50° closed position and leaving the other at previous position (10° closed) so that the intake flow can have a higher swirl level than the previous one. This strategy can be taken as Case-II induction process. The last strategy of induction was to set one of the SCVs at 90° closed position and the other one was left at 10° closed position. This can be considered as Case-III induction process. According to the swirl angle adjustment, the three induction cases were identified as medium tumble, medium swirl and high swirl inductions, respectively. However, it did not mean that Case-III induction could be at a higher swirl level than Case-II. The induction setup was summarized in Table 3.4.

Table 3.4 Swirl control valve adjustment angles and their designation

Induction type	Intake flow	SCV adjustment angle [deg]	
		left	right
Case-I	Medium tumble	10	10
Case-II	Medium swirl	50	10
Case-III	High swirl	90	10

3.2.2.1 Pre-processing and Cross-correlation

PIV images of the flow in a double frames single shot mode were captured at each SCV settings and intake valve positions. These sequential image frames were sub-sampled into smaller regions and the resolution of such sub-sampling can be defined as interrogation area. Provided that a flow is present in the illuminated plane, an average spatial shift of seeding particles can be observed from one sample of image frame to its counterpart in the second image frame within the interrogation area samples. This spatial shift may be described with a linear digital signal processing model as shown in Figure 3.11. The function *I(m,n)* describes the intensity of light

within the interrogation area of the first image at time *t*, and *I'(m,n)* expresses the light intensity in the corresponding interrogation area on the second image, where *(m,n)* describes the pixel position in the interrogation area. In the digital signal processing model, *I'(m,n)* can be considered as the output of an image transfer function *d(m,n)*, taking *I(m,n)* as an input.
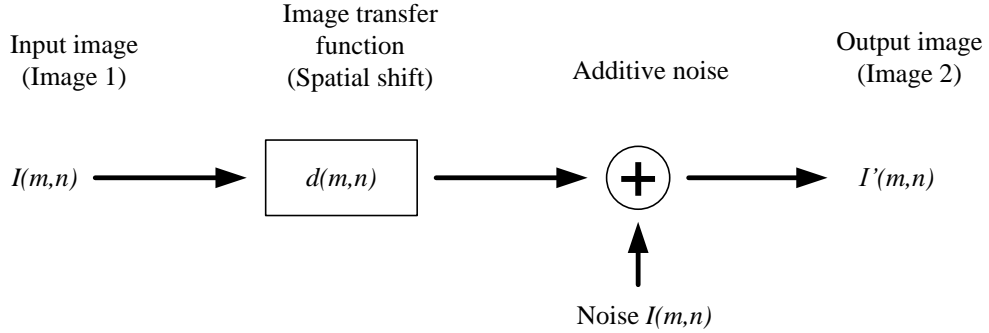
Figure 3.11   Image transfer function idealized by linear digital signal processing model

Cross-correlation between the intensity values of the two images can be performed using Fourier transform technique, and the Fast Fourier Transform (FFT) algorithm can speed up the process. Hence, cross-correlation was effectively done for the collected PIV images using the Dantec FlowManager software which is based on FFT algorithm.

The PIV images may suffer from intensity signal variations throughout the correlation plane. This can strongly affect the correlation output and the brighter particles might dominate the correlation peak. Before the application of cross-correlation on the image pairs, image enhancement techniques were implemented to minimize correlation errors as suggested by Raffel et al. [37]. In this study, background subtraction and masking of unwanted regions are applied on the raw image as a pre-image processing technique. To employ the background subtraction, one common image was first identified by averaging the pixel intensity values of all images of similar parameter (in the current study, a total of 30 image pairs were considered). Then, this common image was finally subtracted from all 30 images. Finally, a mask was applied to avoid the unwanted region in the correlating images or to disregard regions with strong laser flare. The images following this procedure are depicted in Figure 3.12.

There is also another signal enhancement process to avoid cyclic noises created by phantom particles and their correlations especially near to the edge of interrogation area. In this case a window function can be used as a filter to the FFT algorithm. For this study, a Gaussian weighting function, given by Equation 3.1, was used [53]. This function can multiply intensity values of each pixel in the interrogation area (depending on the position of the pixel in the area) before the FFT correlation applied, and suppresses the influence of edge signals on the areal average. This would reduce the bias errors and improve signal-to-noise ratios of the PIV measurement.

$$w(m,n) = exp\left[-\left[\tfrac{1}{k}\right]^2\left(\left(\tfrac{2m}{M}\right)^2 + \left(\tfrac{2n}{N}\right)^2\right)\right] \qquad (3.1)$$

where (M,N) is interrogation area size.

(m,n) pixel position in the interrogation area, *(0,0)* being at the center.

k is width of the window.
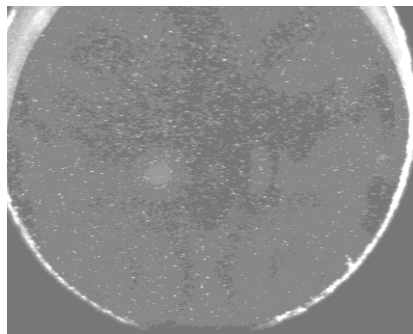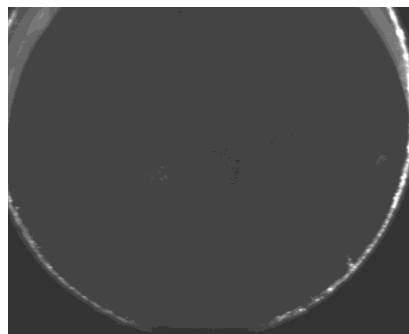
(a) Raw un processed   *(b) Mean pixel intensity*

(c) Image (b) subtracted from (a)   (d) Masked unwanted regions and edges

Figure 3.12   Pre-processing of PIV images

Another function, narrow width low-pass filter function, was also applied on the output of the correlation process in the frequency domain prior to inverse FFT and

peak vector detection. The low-pass filter function given in Equation 3.2 was used for this purpose, and it would be suitable to remove the high frequency noise generated by the camera.

$$w(u,v) = \begin{cases} 0 & for\ (u,v) = (0,0) \\ \exp\left(-k^2 \frac{u^2+v^2}{U.V}\right) & otherwise \end{cases} \qquad (3.2)$$

where (u,v) spatial frequencies

$\qquad (U,V)$ size of frequency domain

3.2.2.2 Post-processing and Derivation of Flow Parameters

After identifying the raw velocity vectors by cross-correlation, erroneous vectors (outliers) can be easily visualized. These outlier vectors might have different size and/or different direction from their neighbors, as demonstrated in Figure 3.13 (a). Therefore, the raw vector fields should pass through a validation procedure in order to obtain a new value for the outliers from their neighbors.

3.2.2.2.1 Moving Average Validation

The rational for this technique to be used is based on the idea that flows have continuity and they change slowly. Therefore, there should be relations between a vector and its neigh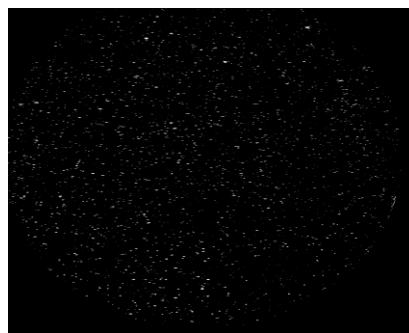bors. If a vector is so much different from its neighbors it might be possible to make a conclusion that it is outlier. In the moving average validation method, the average of neighborhood vectors which can be calculated by Equation 3.3 should be compared to the target vector under consideration. Therefore, the vector would be acceptable if it is within the acceptable range when compared with the average of the neighborhood vectors. If it is not in the acceptable range it would be considered as an outlier and then substituted by a new calculated vector by interpolation. The algorithm for the moving average validation process is given as follows,

1. Define the rectangular grid area, *m by n*, (*5 x 5* window size was chosen in this analysis) and all vectors in area have the same weight

2. Set acceptance factor, α, for the vector to be validated

3. Identify the average velocity U_{avg} from the neighborhood velocity vectors $U(i,j)$ with a grid size defined earlier for a vector positioned at *(x, y)*

$$U_{avg} = \frac{1}{mn} \sum_{i=x-\frac{n-1}{2}}^{x+\frac{n-1}{2}} \sum_{j=y-\frac{n-1}{2}}^{y+\frac{n-1}{2}} U(i,j) \tag{3.3}$$

4. Identify validation check number, *β*, by first identifying the maximum deviation of the vectors in the grid area from the average velocity of Equation 3.3 and then multiply it by the acceptance factor α.

$$\beta = \alpha \max_{x,y} \| U(x,y) - U\_avg \| \tag{3.4}$$

5. The vector to be validated can be rejected if its deviation from the average is greater than the validation check number, *β*

$$\| U(x,y) - U_{avg}(x,y) \| > \beta \tag{3.5}$$

6. If the vector is rejected a new substitute vector can be generated using iterative interpolation technique.

3.2.2.2.2 *Moving Average Filter*

Filter function is always applied on a validated vector data and used to minimize noise which might affect some derivation results, such as vorticity. Moving average filter was used in the current flow analysis. It is a technique of substituting a vector by the average of its neighboring vectors (Equation 3.3). Figure 3.13 shows that the vortices identified from the validated vectors (but unfiltered) were different from the vortices derived from the validated and filtered one. The high frequency noises were observed to affect the circulating core structure and increased the magnitude of circulation as well compared to the filtered field as shown in Figure 3.13 (e) and (f). The filter function was applied on vector fields before the average statistical values were calculated. Then, the ensemble averaged velocity fields including the variance were identified from the total PIV data captured at specific parameter (30 vector fields for every specific parameter)
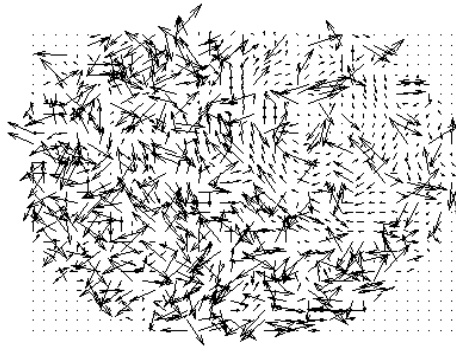
(a)   Raw velocity vector field   *(b) Velocity field validated by moving average*
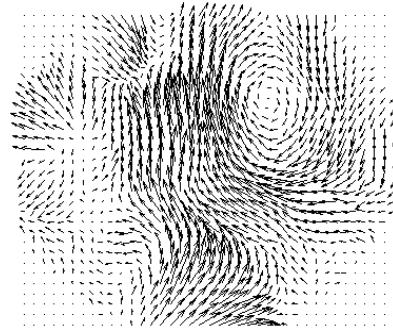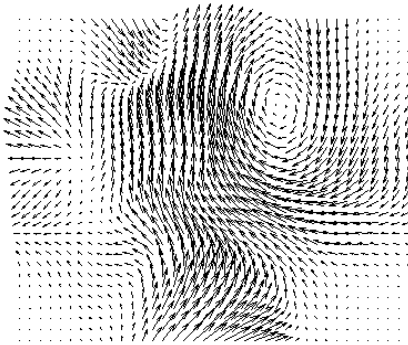
(c)   Low-pass Filterd velocity field after validation   *(d) Ensemble averaged velocity vector field*
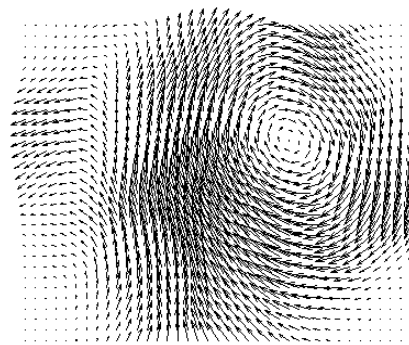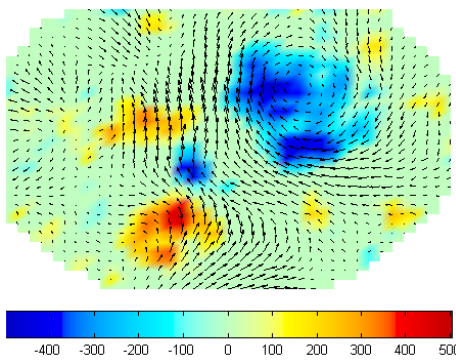
(e)   Vortex identified from (b)   *(f) Vortex identified from (c)*
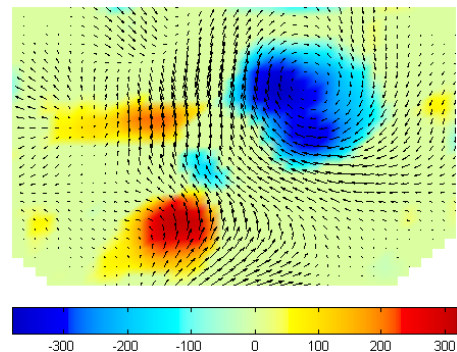
Figure 3.13   Velocity vector fields and vorticity map of filtered and unfiltered vectors

3.2.2.2.3 Swirl Strength Identification

The swirl strength can be identified and be located in the flow field utilizing the local velocity gradient tensor and the corresponding eigenvalue [54], [55]. The local velocity gradient tensor g for two dimensional flows can be given by;

$$g = \begin{bmatrix} \dfrac{\partial u}{\partial x} & \dfrac{\partial v}{\partial x} \\ \dfrac{\partial u}{\partial y} & \dfrac{\partial v}{\partial y} \end{bmatrix} \tag{3.6}$$

where u and v are the x and y velocity components, respectively.

The imaginary part of the eigenvalue of the gradient tensor given in Equation 3.6 can exactly locate a swirling vortex in the flow field.

$$\begin{bmatrix} \dfrac{\partial u}{\partial x} - \lambda & \dfrac{\partial v}{\partial x} \\ \dfrac{\partial u}{\partial y} & \dfrac{\partial v}{\partial y} - \lambda \end{bmatrix} = 0 \tag{3.7}$$

where λ is eigenvalue.

So, solution for λ can be given by

$$\lambda = \frac{1}{2}\left(\frac{\partial u}{\partial x} + \frac{\partial v}{\partial y}\right) \pm \frac{1}{2}\sqrt{\left(\frac{\partial u}{\partial x} + \frac{\partial v}{\partial y}\right)^2 - 4\left(\frac{\partial u}{\partial x}.\frac{\partial v}{\partial y} - \frac{\partial u}{\partial y}.\frac{\partial v}{\partial x}\right)} \tag{3.8}$$

Region of the flow field which has negative values for the expression in the square root of Equation 3.8 would show the presence of swirling vortex. That means, in the region where $4\left(\frac{\partial u}{\partial x}.\frac{\partial v}{\partial y} - \frac{\partial u}{\partial y}.\frac{\partial v}{\partial x}\right) > \left(\frac{\partial u}{\partial x} + \frac{\partial v}{\partial y}\right)^2$, there could be a swirling vortex. Therefore, the magnitude of the swirl strength can be identified precisely by the imaginary part of the eigenvalue λ_i as elaborated in [54].

$$\lambda_i = \frac{1}{2}\sqrt{\left|\left(\frac{\partial u}{\partial x} + \frac{\partial v}{\partial y}\right)^2 - 4\left(\frac{\partial u}{\partial x}.\frac{\partial v}{\partial y} - \frac{\partial u}{\partial y}.\frac{\partial v}{\partial x}\right)\right|} \tag{3.9}$$

Equation 3.9 does not provide any information about the direction of the swirling vortex. The direction can be recovered by analyzing the surrounding velocity field as suggested in [37] or multiplying λ_i by the sign of local in-plane vorticity as used in [55]. The local vorticity ω_z can be identified from Equation 3.10

$$\omega_z = \frac{\partial v}{\partial x} - \frac{\partial u}{\partial y} \tag{3.10}$$

Hence, the magnitude and direction of swirl strength is given by,

$$\lambda_s = \lambda_i \frac{|\omega_z|}{\omega_z} \tag{3.11}$$

3.3 Early Flame Development Experimental Setups and Analysis Methods

The main task of this study was to investigate an early flame development of a CNG fuel in a direct injection combustion engine. The flame data was directly captured from the engine and analyzed consequently. The experimental setup and detail analysis techniques are discussed as follows.

3.3.1 Flame Imaging Experimental Setup

The early flame visualization is realized via direct imaging of the flame using its own luminosity. This visualization technique was selected from some options based on availability and measurement accessibility. Technically, the available diagnostic tools in the current research center (CAR) of UTP were capable of achieving laser tomography for the flame imaging. These are 1) flame region identification using the Planar Laser-Induced Fluorescence (PLIF) method by imaging exited radicals of combustion gas products at appropriate laser wavelength, such us OH at 266 nm, and 2) application of two-dimensional Mie scattering method to image seed particles in the flow outside the flame region because of the burning up of the seed particles in the flame region. The application of these methods for early flame imaging in which the small flame wandering around by the flow in the cylinder is very difficult. The laser sheet must intersect the flame in order to get the flame boundary. Having a laser sheet at specific location and small flame wandering here and there depending on the nature of the flow, it will be very difficult to implement laser tomography for this specific study. Therefore, the direct imaging of the flame was realized using endoscopic CCD camera arrangement. Even though there was an option of visualizing in-cylinder processes via optical window, it was found not applicable for early flame imaging due to the position of the spark plug well above the visualized region of the cylinder. Therefore, an experimental setup was prepared as shown in Figure 3.14.
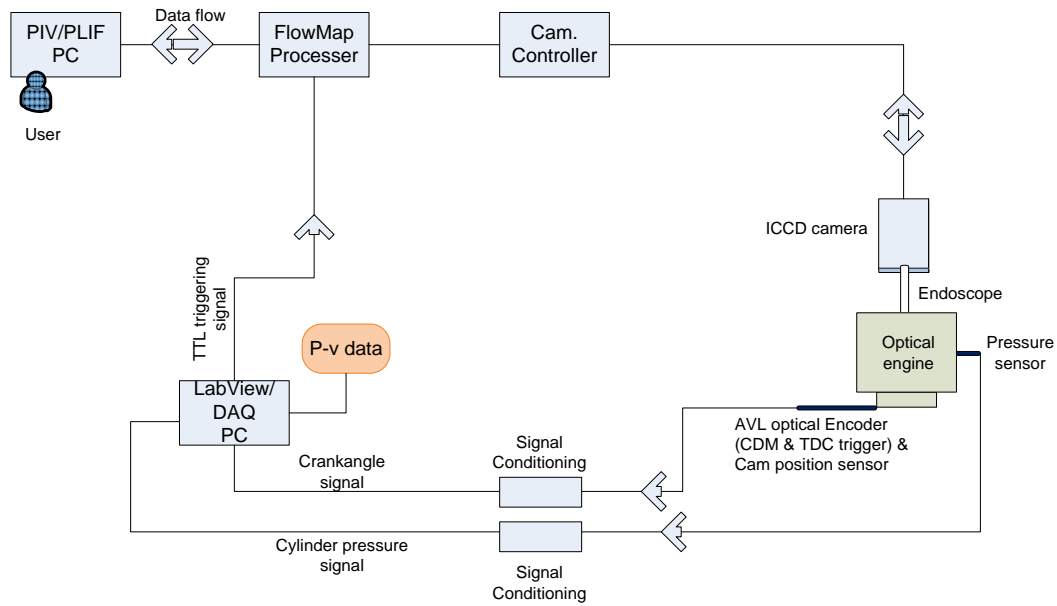
Figure 3.14   Experimental setup for flame imaging

3.3.2 Data Acquisition System

The endoscopes and the camera with the image intensifier were fixed on the engine to capture early flames starting from the ignition moment every 2° CAs for about 30° CA degrees. Therefore, the imaging system must be synchronized with the combustion process in the cylinder. Timing for process controlling purpose in engine is crank angles. The Engine Control Unit (ECU) works with this principle by collecting signals from the crank angles and camshaft signal as well. The optical crank angle encoder generates signal ticks every 0.5^o CA and sends them to a 10 MHz National Instruments Data Acquisition (NI-DAQ) system. A total of 720 signal ticks can be generated in one revolution and one of them is a TDC trigger signal to locate the TDC point. In the current engine system, the TDC signal is located at 126.5^o CA before the actual TDC position of the piston in the cylinder.

The other important signal is the camshaft signal which is generated by an encoder fixed on the camshaft wheel every cycle. This camshaft signal appears at 30.5^o CA after compression TDC. Three distinct types of signals were collected from the engine system via encoders and used by the DAQ system. These are the crank angle marker (CDM) signal for every 0.5^o CA, TDC signal for every revolution and

camshaft signal for every cycle. There is still another type of signal from the engine unit, a signal generated by water cooled piezoelectric pressure transducer (Kistler 6061B). The piezoelectric crystal generates electric charges in pico-coulomb related to the distortion level caused by cylinder pressure. The charge signal is converted into voltage signal in a charge amplifier. Signal calibration takes place in the NI DAQ system and the analog signal is converted to digital one to quantify the pressure developed in the cylinder. This signal can be used to calculate heat release and fuel burn fractions in the combustion process.

A LabView program was prepared to utilize the signals and generate useful information from the engine system. Pressure transducer, CDM and TDC trigger signals were used for the generation of pressure/volume data from the engine, whereas cam position and CDM signals were used to generate TTL signals for external triggering of the camera at any crank angle.

3.3.3 Flame Analysis Technique

Flame images where collected at every 2° CA from the start of ignition to 10° BTDC. The intensified CCD camera was set to operate on single-frame mode. The frame integration time of the camera was adjusted to be 300 µs. The full pixel area of the camera, that is 1280 pixels x 1024 pixels, was utilized. The TTL trigger signal generated using LabView program and NI-DAQ system was received by the synchronization board of Dantec FlowMap processor that triggered the camera at the preset crank angle. The data capturing rate was limited by the maximum frame rate of the CCD camera. The maximum frame rate of the camera working on a single-frame mode is 9 Hz. Therefore, the rate of flame capturing was set at every two cycles for 1500 rpm and 1800 rpm engine speeds, and every three cycles for 2100 rpm engine speed.

A total of 30 flame images were captured at every required crank angle in order to get the average properties of the developing flame for that specific crank angle. The flame development period was considered to be the first 30° CA (about 3 ms duration) combustion time after ignition onset. Aleiferis et al. [5] described the development

period to be within 30° to 40° CA after ignition onset because the flame can perform growth within this period due to the turbulence-induced change of flame shape such as wrinkling and distortion, and due to heat losses to the electrodes.

Flame images captured from combustion cylinders have high probability of accompanying noises of different types in relation with flame capturing process (shot noise) and from the nature of the camera in relation with its dynamic range. Therefore, image filtering was considered as a pre-processing step to reduce the effect of this random and unrelated information from the flame.

3.3.3.1 Gaussian Filter

The Gaussian averaging operator can be used as an image filtering by smoothening small details from the flame images. The Gaussian function, G, at x and y is controlled by the variance, σ^2, of the operator, as given in Equation 3.12. This Gaussian kernel operator was applied for filtering the high frequency noises from the image. The Gaussian kernel for a 2-D representation can be given by;

$$G(x, y; \sigma) = \frac{1}{2\pi\sigma^2} e^{-\frac{x^2+y^2}{2\sigma^2}} \qquad (3.12)$$

where σ determines the width of the Gaussian kernel or the standard deviation. It is the inner scale of the kernel. The larger the standard deviation the more the image gets blurred. For the current study σ was set to be 1.5, and for a square window, the values of x and y set to be $6*\sigma$, that would be a 9 x 9 matrix.

$$x = \begin{bmatrix} -4 & -3 & -2 & -1 & 0 & 1 & 2 & 3 & 4 \\ -4 & -3 & -2 & -1 & 0 & 1 & 2 & 3 & 4 \\ -4 & -3 & -2 & -1 & 0 & 1 & 2 & 3 & 4 \\ -4 & -3 & -2 & -1 & 0 & 1 & 2 & 3 & 4 \\ -4 & -3 & -2 & -1 & 0 & 1 & 2 & 3 & 4 \\ -4 & -3 & -2 & -1 & 0 & 1 & 2 & 3 & 4 \\ -4 & -3 & -2 & -1 & 0 & 1 & 2 & 3 & 4 \\ -4 & -3 & -2 & -1 & 0 & 1 & 2 & 3 & 4 \\ -4 & -3 & -2 & -1 & 0 & 1 & 2 & 3 & 4 \end{bmatrix}$$

$$y = \begin{bmatrix} -4 & -4 & -4 & -4 & -4 & -4 & -4 & -4 & -4 \\ -3 & -3 & -3 & -3 & -3 & -3 & -3 & -3 & -3 \\ -2 & -2 & -2 & -2 & -2 & -2 & -2 & -2 & -2 \\ -1 & -1 & -1 & -1 & -1 & -1 & -1 & -1 & -1 \\ 0 & 0 & 0 & 0 & 0 & 0 & 0 & 0 & 0 \\ 1 & 1 & 1 & 1 & 1 & 1 & 1 & 1 & 1 \\ 2 & 2 & 2 & 2 & 2 & 2 & 2 & 2 & 2 \\ 3 & 3 & 3 & 3 & 3 & 3 & 3 & 3 & 3 \\ 4 & 4 & 4 & 4 & 4 & 4 & 4 & 4 & 4 \end{bmatrix}$$

Inserting the x and y matrix into Equation 3.12 results in the weighting coefficients,

$$G = \begin{bmatrix} 0.0001 & 0.0003 & 0.0008 & 0.0016 & 0.0020 & 0.0016 & 0.0008 & 0.0003 & 0.0001 \\ 0.0003 & 0.0013 & 0.0040 & 0.0077 & 0.0096 & 0.0077 & 0.0040 & 0.0013 & 0.0003 \\ 0.0008 & 0.0040 & 0.0120 & 0.0234 & 0.0292 & 0.0234 & 0.0120 & 0.0040 & 0.0008 \\ 0.0016 & 0.0077 & 0.0234 & 0.0456 & 0.0569 & 0.0456 & 0.0234 & 0.0077 & 0.0016 \\ 0.0020 & 0.0096 & 0.0292 & 0.0569 & 0.0711 & 0.0569 & 0.0292 & 0.0096 & 0.0020 \\ 0.0016 & 0.0077 & 0.0234 & 0.0456 & 0.0569 & 0.0456 & 0.0234 & 0.0077 & 0.0016 \\ 0.0008 & 0.0040 & 0.0120 & 0.0234 & 0.0292 & 0.0234 & 0.0120 & 0.0040 & 0.0008 \\ 0.0003 & 0.0013 & 0.0040 & 0.0077 & 0.0096 & 0.0077 & 0.0040 & 0.0013 & 0.0003 \\ 0.0001 & 0.0003 & 0.0008 & 0.0016 & 0.0020 & 0.0016 & 0.0008 & 0.0003 & 0.0001 \end{bmatrix}$$

Convolution is the technique to identify a new pixel values from the neighbor pixels using a weighting coefficients over all the pixels of the image to be filtered. In this study the Gaussian filter G is the weighting coefficients. To perform convolution using this kernel first G must be rotated 180°. Then, image pixel values are multiplied by the flipped coefficients and added to get overall sum. That gives the new value for the center pixel in the filtered image. For edge pixels, zero padding can be used to place those pixels at the center of the filter kernel.

3.3.3.2 Image Binarization

Image binarization is a process of thresholding or segmenting an image into an object and a background according to the gray level of the pixels using a specific threshold value. It is an effective tool to separate the object from its background with the pixels value found to be $(x, y) = \begin{cases} 1 & if\ f(x,y) \geq T \\ 0 & otherwise \end{cases}$, with a given threshold value T.

The important step in binarization is to identify the appropriate threshold value that can separate the foreground (or the object) from the background. Sezgin and Sakur [56] made a comprehensive evaluation of around 40 thresholding techniques by

categorizing them into six groups according to the information the techniques are exploiting. They also compared the thresholding performance of the different techniques. The criteria they investigated for every thresholding methods were their misclassification error, edge mismatch, relative foreground area error, modified Hausdorff distance and region non-uniformity. They found out that out of the many techniques available, the histogram based Ostu thresholding method was in the first six best performed groups and they also observed that this technique had been the most referenced and applied technique.

Ostu thresholding method was first introduced by N. Otsu in 1979 [57], and has been used for decades for image segmentation process in many areas such as weld defect identification of radiographic images [58] and plant leaf classification [59]. The Ostu thresholding technique uses the gray level statistics of the image and requires setting of some criteria to achieve the segmented binary image. In this study, the Ostu thresholding method was applied due to its better performance as discussed in [56] and its simplicity to implement an efficient algorithm for multiple images in automatic segmentation process.

The Histogram-based Ostu thresholding method depends on the statistical distribution of gray level values of the image pixels. The derivation of the algorithm started by representing image pixels intensity by *L* gray levels, and that can be given in the range [1, 2, 3, …, i, i+1, …, L]. The normalized gray level histogram of pixels can be considered as a probability distribution function and then the appropriate statistical parameters, such as mean levels, class occurrences and variances were identified. Assuming that the number of pixels in level *i* is denoted by h_i and the total number of pixels is denoted by *N*. The probability distribution of the pixels' gray level can be given by Equation 3.13:

$$P_i = \frac{h_i}{N}, \quad P_i \geq 0, \quad \sum_{i=1}^{L} P_i = 1 \tag{3.13}$$

Since the main aim of thresholding is segregating image pixels into classes, an arbitrary threshold valve *k* is set and the pixels are classified according to their gray levels. Suppose classes C_0 and C_1 are formed such that C_0 may contain pixels having gray level values range *0 to k* and C_1 contains values in the range *k to (L-1).* Then, the

probability of class occurrences (ω), class means (μ) and class variances (σ^2) for both classes can be given by:

$$\omega_0 = \sum_{i=0}^{k} P_i \; ; \qquad \omega_1 = \sum_{i=k+1}^{L-1} P_i \; = 1 - \omega_0 \tag{3.14}$$

$$\mu_0 = \sum_{i=0}^{k} \frac{iP_i}{\omega_0} \; ; \qquad \mu_1 = \sum_{i=k+1}^{L-1} \frac{iP_i}{\omega_1} = \frac{\mu_T - \mu_k}{1 - \omega_0} \tag{3.15}$$

$$\sigma_0^2 = \sum_{i=0}^{k} (i - \mu_0)^2 P_i \; ; \quad \sigma_1^2 = \sum_{i=k+1}^{L-1} (i - \mu_1)^2 P_i = \sigma_T^2 - \sigma_0^2 \tag{3.16}$$

$$\mu_T = \sum_{i=0}^{L-1} iP_i \; ; \qquad \sigma_T^2 = \sum_{i=0}^{L-1} (i - \mu_T)^2 P_i \tag{3.17}$$

where: μ_T and σ_T^2 are stands for total mean and variance, and $\mu_k = \sum_{i=0}^{k} iP_i$

The next step would be the identification of the appropriate threshold value k to segment pixels into their class. The technique devised by Otsu [57] utilized the approach of maximization of between-class variance to identify the threshold value. Between-class variance, σ_B^2, can be identified via Equation 3.18:

$$\sigma_B^2 = \omega_0(\mu_0 - \mu_T)^2 + \omega_1(\mu_1 - \mu_T)^2 \tag{3.18}$$

Therefore, the optimum threshold value, k^*, can be given by:

$$\sigma_B^2(k^*) = \text{Max}\,\sigma_B^2(k), \qquad for \; 1 \le k \le L \tag{3.19}$$

3.3.3.3 Flame Boundary Tracing

The pixels of the binary flame images identified by the Ostu thresholding method have logical expression that can be black for object and white for background, or can be quantized as 1 for object (foreground) and 0 for background. For further flame analysis the boundary vertices must be retrieved from the binary images. A Moore-neighbor tracing technique with Jacob's stopping criterion was applied to retrieve the boundary vertices of the flame images. The algorithm is simple and can be implemented on Matlab platform. It works by scanning the binary image starting from left bottom up and to the right along the columns until the first black pixel is found and is set as the first vertex of the boundary. Then, returning back to the last previous

white pixel and trace clockwise or counterclockwise (direction must be consistent) around the Moore neighborhood of the black pixel identified earlier until another black pixel is found. The algorithm terminates when the first pixel is met for the second time. Finally, N x 2 vertices can be collected to define the outer contour of the flame for further analysis; where N is the total number of points that describe the contour.

3.3.3.4 *Chain Coding and Elliptic Fourier Representation of Flame* Contours

Chain codes are used to characterize a boundary by a connected sequence of straight line segments of specified length and direction. Chain codes are widely used as standard input format for image shape analysis algorithms, such as in Fourier analysis technique. H. Freeman [60] was the first to create this code and the principle was based on the idea that any continuous curve can be represented by straight line segments and angles describing directions of the segmented lines. He reached to a conclusion that any desired precision of curve prediction by the chain code can be obtained with a coarse angle quantization and arbitrarily small standard distances of the line segments.

The Freeman chain-code, named after the inventor, was composed of 4-connected and 8-connected codes. In this study, the 8-connected grid was utilized to code the flame boundary for the purpose of generating important inputs for Elliptic Fourier Analysis (EFA) program. The codes that represent the segmented lines are given by 0 1 2 3 4 5 6 7, and each code represents a specific direction of traversing to the next pixel throughout the contour until it returns to the starting pixel as illustrated in Figure 3.15. The segment size can be taken to be the step to the next pixel on the flame contour, and its length equals to either 1 or $\sqrt{2}$ pixels.
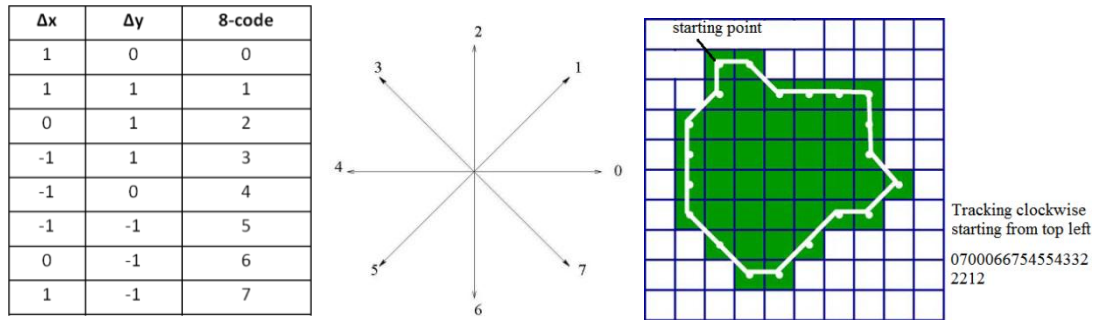
Figure 3.15   Freeman chain with eight connection grid and codes representing the boundary of a binary image

The output of the chain code can be inputs into the EFA code. Elliptic Fourier function was first introduced by Kuhl and Giardina in the 80's [61]. Most of the applications were in the field of plant and animal species identification and classifications [62], [63] and human anatomy studies [64]. Basically, the coefficients of the elliptical Fourier analysis are function of the shape of the boundary under consideration. The coefficients can be size invariant so that they define shape character in spite of size variations of an object. This code is very effective for data reduction by reducing the boundary points to be considered without affecting the ultimate shape and it is also able to avoid the details of the boundary by changing the harmonic levels.

Elliptic Fourier coefficients maintain description of object boundaries or curves in a two-dimensional space which defines the complex plane [65]. Each pixel in the image space is represented by a complex plane with the first coordinate to be real and second coordinate to be imaginary. Therefore, the complex plane representation of image contours as function of arc length *t* can be defined by Equation 3.20.

$$c(t) = X(t) + jY(t) \tag{3.20}$$

Based on the general complex plane representation of curves by Equation 3.20, it is possible to identify the Elliptic Fourier coefficients by performing Fourier expansions of this equation. After some detail analysis of the Fourier expansion process as discussed in [65], *X* and *Y* coordinate representations were identified.

$$X_N(t) = A_0 + \sum_{n=1}^{N} a_n cos\left(\frac{2n\pi t}{T}\right) + b_n sin\left(\frac{2n\pi t}{T}\right) \tag{3.21}$$

$$Y_N(t) = C_0 + \sum_{n=1}^{N} c_n \cos\left(\frac{2n\pi t}{T}\right) + d_n \sin\left(\frac{2n\pi t}{T}\right) \qquad (3.22)$$

where, the arc-length t is the step required to traverse one pixel along the closed contour, $t_{p-1} < t < t_p$ for $1 \le p \le k$. k is the total number of codes describing the boundary contour. n is the number of Fourier harmonics. T is the basic period of the chain-code, that is $T = t_k$. A_0 and C_0 are the bias coefficients, at $A_0 = 0$ and $C_0 = 0$ the center of the region enclosed by the contour to be at the origin of the axis. N is the total number of Fourier harmonics needed to generate an accurate approximation of the flame boundary.

Increasing the harmonic levels will increase the representation of details of the boundary of the object. Lower frequencies which contain the general feature of the boundary shape can be indexed by the lower harmonics and the total number of Fourier coefficients used to describe the boundary will be reduced in a similar manner. This technique was found to be efficient to approximate the mean flame contour in the study by avoiding the details of the curves. On the other hand, the high frequency details of the flame contour structure are revealed by higher harmonic analysis, which is important to reconstruct the turbulent flame contour in this study.

For every level of harmonic, the x and y values of the codes that can reconstruct the boundary were identified from Equations 3.21 and 3.22. In these equations, there are four unknown coefficients, a_n, b_n, c_n and d_n, and they can be identified from Equations 3.23 to 3.26 for the nth harmonic as elaborated in [61]. The bias coefficients, A_0 and C_0, in Equations 3.21 and 3.22 can be taken as the center of the flame surface or can be set to zero to make it translation invariant.

$$a_n = \frac{T}{2n^2\pi^2} \sum_{p=1}^{k} \frac{\Delta x_p}{\Delta t_p} \left[\cos\left(\frac{2n\pi t_p}{T}\right) - \cos\left(\frac{2n\pi t_{p-1}}{T}\right) \right] \qquad (3.23)$$

$$b_n = \frac{T}{2n^2\pi^2} \sum_{p=1}^{k} \frac{\Delta x_p}{\Delta t_p} \left[\sin\left(\frac{2n\pi t_p}{T}\right) - \sin\left(\frac{2n\pi t_{p-1}}{T}\right) \right] \qquad (3.24)$$

$$c_n = \frac{T}{2n^2\pi^2} \sum_{p=1}^{k} \frac{\Delta y_p}{\Delta t_p} \left[\cos\left(\frac{2n\pi t_p}{T}\right) - \cos\left(\frac{2n\pi t_{p-1}}{T}\right) \right] \qquad (3.25)$$

$$d_n = \frac{T}{2n^2\pi^2} \sum_{p=1}^{k} \frac{\Delta y_p}{\Delta t_p} \left[\sin\left(\frac{2n\pi t_p}{T}\right) - \sin\left(\frac{2n\pi t_{p-1}}{T}\right) \right] \qquad (3.26)$$

$$\Delta t_p = \sqrt{\Delta x_p^2 + \Delta y_p^2} \tag{3.27}$$

$$t_p = \sum_{i=1}^{p} \Delta t_i \tag{3.28}$$

where Δx_p and Δy_p are the spatial changes in the respective axis identified from the chain code at point p of the flame contour. Δt_p is the step change that is required to travel from point *p-1* to p of the chain code. t_p is the total number of steps to travel up to point p in the chain code. The Elliptic Fourier analysis code receives inputs from the Freeman chain code analysis.

The coefficients do not contain redundant information and they can also uniquely describe shapes of closed contours. These coefficients represent dimensions of each ellipse on every level of harmonic, as demonstrated in Figure 3.16.
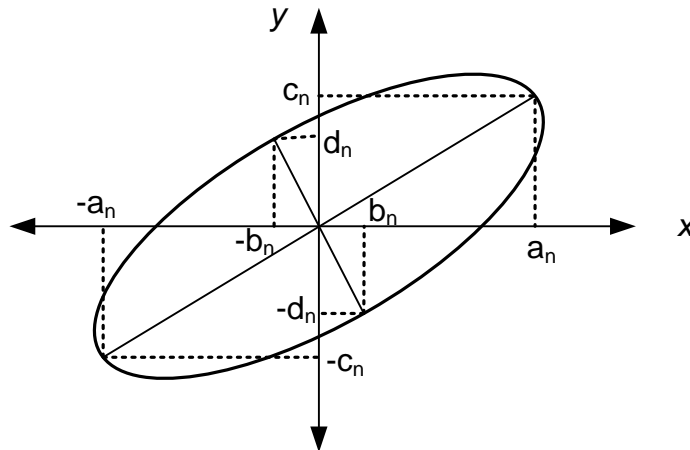

Figure 3.16   Schematic of harmonic ellipse and Fourier coefficients

The x- and y-coordinates are computed separately (using Equations 3.21 to 3.26) and the shape of the object can be recreated by rejoining these coordinates for identical value of *t*, as shown in Figure 3.17. If each harmonic is plotted separately, ellipses of different sizes will be produced. Summing of these ellipses as described in the Fourier series representation will converge to the polygon that serves as the observed shape as portrayed in Figure 3.18 for a typical flame contour.
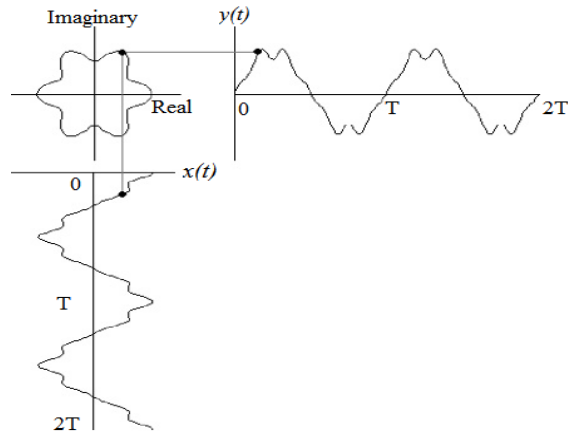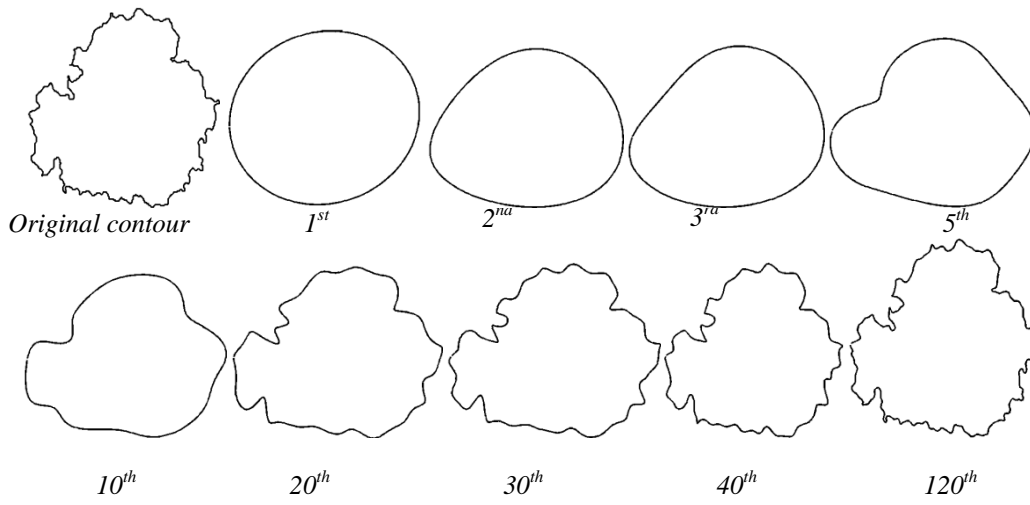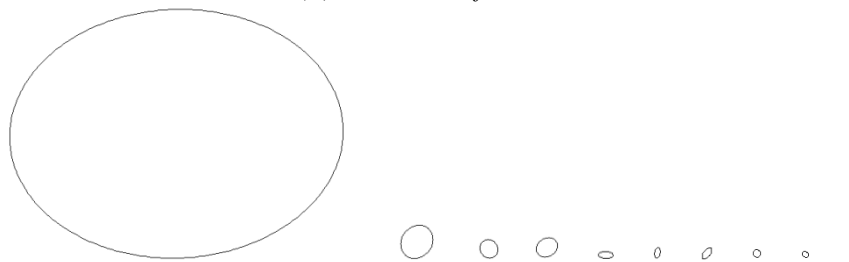
Figure 3.17   The complex curve representation from the two coordinates

| Original contour | 1st | 2nd | 3rd | 5th |

| 10th | 20th | 30th | 40th | 120th |

(a)   Generated flame contours

(b)   The first 10 harmonic ellipses to generate the flame contour in (a)

Figure 3.18   Flame contours from the outlines of Elliptic Fourier analysis at variable harmonics

The other advantage of this technique is that it can be invariant to rotation, size change, translation and starting point so that they can describe characteristics related to shapes only. Starting point invariant can be implemented into the technique by first, identifying the angle, θ_1, between the starting point and the first semi-major axis

along the same direction of contour rotation via coefficients of the Fourier analysis resulted from the first harmonic level, and then rotating the coefficients to get zero phase shift [66].

$$\theta_1 = \frac{1}{2} arctan \left[\frac{2(a_1 b_1 + c_1 d_1)}{a_1^2 + c_1^2 - c_1^2 - d_1^2} \right] \quad 0 \leq \theta_1 \leq 2\pi \tag{3.29}$$

The new corrected coefficients for starting point adjustment can be identified by Equation 3.30:

$$\begin{bmatrix} a_n^* & b_n^* \\ c_n^* & d_n^* \end{bmatrix} = \begin{bmatrix} a_n & b_n \\ c_n & d_n \end{bmatrix} \begin{bmatrix} cos\theta_1 & -sin\theta_1 \\ sin\theta_1 & cos\theta_1 \end{bmatrix} \tag{3.30}$$

The rotation invariant feature can be applied to the analysis to align the semi-major axis of the first harmonic with the positive x-axis. The rotational angle,φ_1, was first identified and the semi-major axis was rotated to make it parallel to the positive x-axis of the first quadrant.

$$\varphi_1 = arctan \left[\frac{Y_1^*(0)}{X_1^*(0)} \right] = arctan \left(\frac{c_1^*}{a_1^*} \right) \tag{3.31}$$

Where $Y_1^*(0)$ and $X_1^*(0)$ were identified by applying Equation 3.30 into Equation 3.21 and Equation 3.22 at *t=0*. Then, the rotation invariant coefficients can be identified by Equation 3.32 as follows:

$$\begin{bmatrix} a_n^{**} & b_n^{**} \\ c_n^{**} & d_n^{**} \end{bmatrix} = \begin{bmatrix} cos\varphi_1 & sin\varphi_1 \\ -sin\varphi_1 & cos\varphi_1 \end{bmatrix} \begin{bmatrix} a_n^* & b_n^* \\ c_n^* & d_n^* \end{bmatrix} \tag{3.32}$$

In order for the analysis to be size invariant, the coefficients are divided by the magnitude of the semi-major axis,R^*, of the first ellipse.

$$R^* = \sqrt{a_1^{*2} + c_1^{*2}} = a_1^{**} \tag{3.33}$$

Setting the bias terms A_0 and C_0 to zero, resulted the Elliptic Fourier coefficients to be invariant to translation. If the coefficients are invariant to all the above mentioned parameters, they will be in a position to describe only the shape of the contour. In other words, the coefficients can vary only with the change in the shape of the closed contour. This can give option to investigate early flame shape change from

its spherical shape in the beginning of combustion via their Elliptic Fourier coefficients.

It was discussed earlier and shown in Figure 3.18 that the variable harmonic level reconstruction of flame contours can yield different levels of contour details. These variable levels of harmonic contour regeneration will provide different amplitudes of elliptic Fourier coefficients depending on the details of the contour represented in the regeneration. These amplitudes (*A*) of elliptic Fourier coefficients can be identified by,

$$A = \frac{1}{2}\sqrt{a_n^2 + b_n^2 + c_n^2 + d_n^2} \tag{3.34}$$

as discussed in [63]. Using the amplitudes, we can set the cutoff harmonic level for the construction of mean flame contour. High amplitude harmonics describe the general feature of the flame contour, whereas low amplitude harmonics outline the very details of the contour. In this study, the cutoff value for harmonic levels to identify the mean flame contour was set to be the one that has the nearest amplitude to one. For instance, the amplitudes of coefficients for the regenerated flame contours given in Figure 3.18 for the 1th, 2nd, 3rd, 5th, 10th, 20th, 30th, 40th and 120th harmonic levels were identified to be 61.86, 6.70, 2.58, 2.84, 0.48, 0.42, 0.26, 0.09 and 0.02 in pixels, respectively. For this particular flame, the mean contour can be identified at the 6th harmonics having amplitude of 0.91, and it is shown in Figure 3.19 (b) that the mean flame contour as superimposed on the turbulent flame contour.
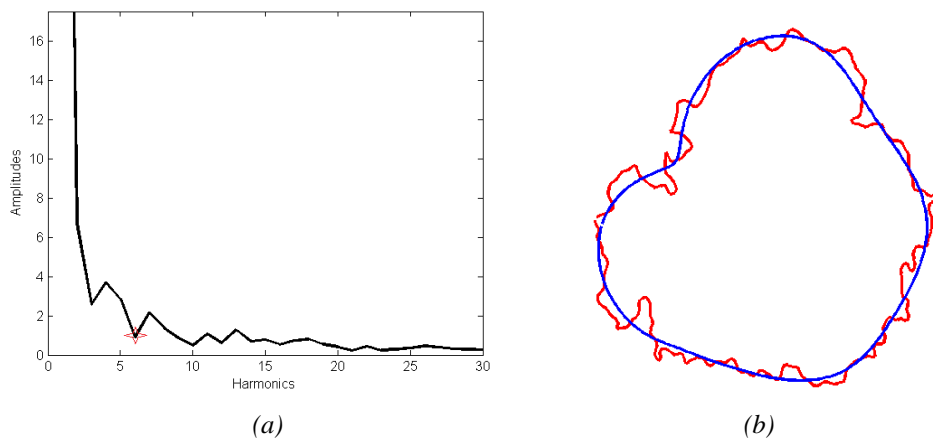

(a)   *(b)*

Figure 3.19   (a) Harmonic cutoff value (b) turbulent and mean flame contour superimposed

3.3.3.5 Derived Parameters to Measure Flame Development Characteristics

The main objective of the study is quantitative characterization of the early flame of a CNG combustion in an overall-lean stratified and homogeneous mixtures based on the morphological analysis of the flame contour via Elliptic Fourier functions and image processing techniques. The selected parameters for flame contour analysis were:

1) **Flame growth rate**; the ratio of equivalent flame radii and time have been used for flame growth rate calculation in [5], [23]. The same technique was applied in the study. Hence, flame growth rate can be defined by,

$$S_g = \frac{dr}{dt} \tag{3.35}$$

where r is radius of a circle having the same area to the mean flame region.

2) **Flame distortion;** flame distortion is a measure of large scale flow effect on the flame surface. At the beginning of combustion phase, the shape of a typical SI combustion flame is nearly spherical. Figure 3.20 shows early flame images of a medium swirl intake induction at 1800 rpm stratified combustion captured at 0.17 ms and 1.84 ms after ignition onset. It can be easily observed that the flame became distorted and wrinkled as well within less than 2 ms.
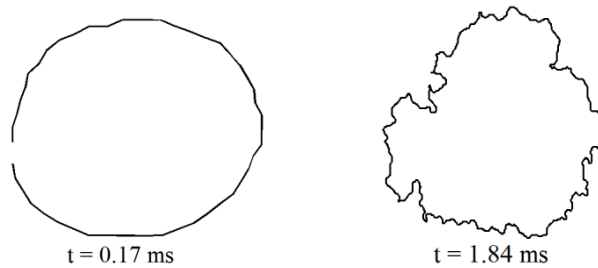
t = 0.17 ms   t = 1.84 ms

Figure 3.20   Flame contours at different timings after ignition onset (sizes are not properly scaled for illustration purpose)

Flame distortion is a large scale effect on the flame surface as it was discussed earlier, whereas the flame wrinkles can be taken as small scale flow influence on it. These small scale effects can be disregarded to measure distortion only due to large scale flow effects. Therefore, the flame distortion level can be measured by the ratio of mean flame contour perimeter and an equivalent circle perimeter, as given in Equation 3.36.

$$F_d = \frac{mean\ flame\ perimeter}{equvalent\ circle\ perimeter}$$

(3.36)

where mean flame perimeter is distance measured along the mean flame contour and the equivalent circle perimeter is given by $2\pi r$.

3) **Flame front wrinkles; s**mall scale eddies can distort flame curvature locally or able to wrinkle flame fronts. Wrinkles on flame surfaces can increase the reaction surface area and generally results high combustion rate. The level of wrinkles commonly identified by measuring the displacement of each turbulent contour segment from its position on the mean flame contour as shown in Figure 3.21. A computer code is prepared to identify the displacement of a point from the mean flame contour to the turbulent flame contour. The number of measured distances depends to the number of points that defines the contour. These distances give the chance to know how far the local curvatures get distorted by the small scale eddy interactions with the flame front. The standard deviation of these measured distances can be regarded as the measure of flame front wrinkledness levels [5].
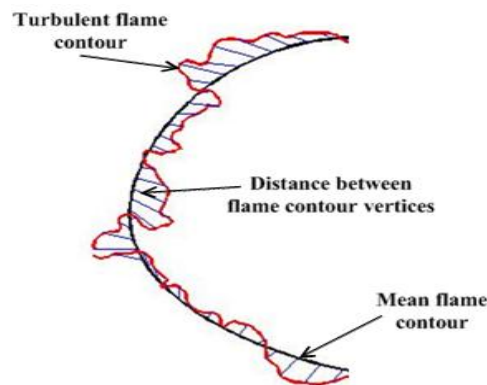

Figure 3.21   Displacement of turbulent flame contour from mean contour

4) **Flame centroid displacement;** it is the measure of convection of the early flame by wandering large eddies and by the mean bulk flow. It is measured by the Euclidian distance between the spark center and the flame centroid. This distance is very important in the early portion of flame development period when the flame is very small. During this stage, it is advantageous for the flame to be away from the spark electrodes to avoid quenching.

3.3.4 Fuel Mass Burn Analysis

The engine performance analysis can be calculated from cylinder pressure data. Piezoelectric pressure transducer installed on the cylinder head with the sensing element inside the cylinder was used to measure the pressure at variable crank angle by assuming uniform pressure throughout the cylinder. Heat release and fuel mass burn fractions are also identified via the cylinder pressure data.
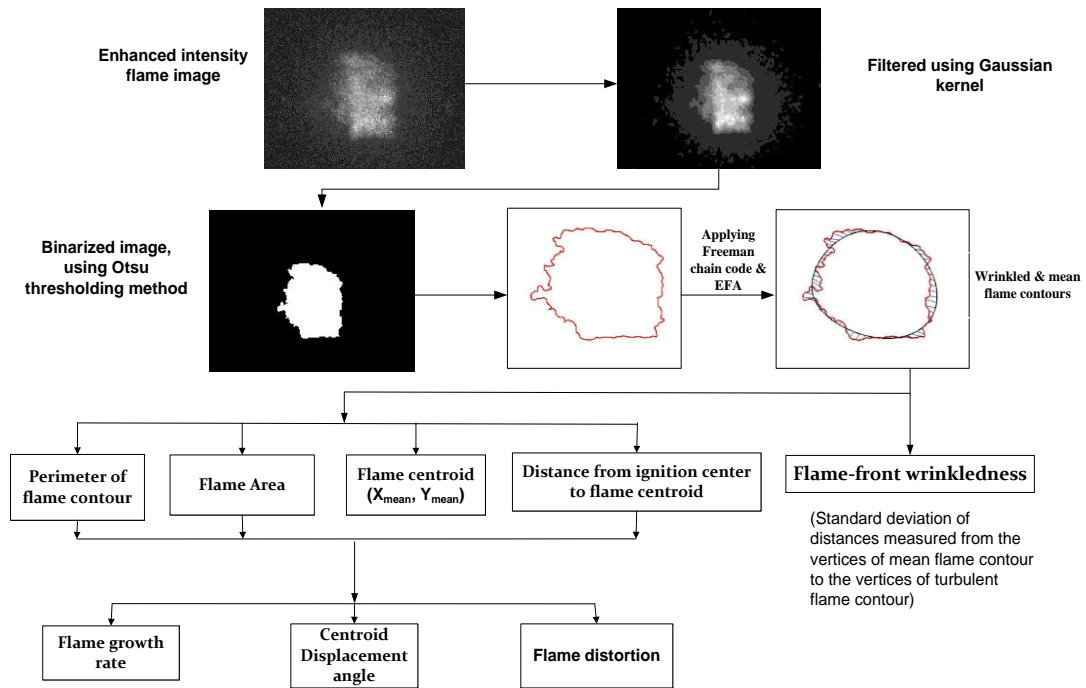

Figure 3.22   Flame image processing algorithm

Rassweiler and Withrow model was applied to identify the fuel mass fraction burned at any crank angle during combustion via the cylinder pressure data [67]. The pressure in the cylinder can be raised by two ways; by compression process and/or by combustion. In order to identify the fuel fraction burned it is very important to obtain the portion of the cylinder pressure raised due to the combustion process only. Therefore, the fuel mass burn fraction at the end of the ith time interval can be given by,

$$F_{bf} = \frac{\sum_0^i \Delta p_c}{\sum_0^N \Delta p_c} \tag{3.37}$$

where Δp_c the portion of incremental cylinder pressure due to combustion. The incremental pressure can be identified from the total increment measured by the pressure transducer.

$$\Delta p = \Delta p_c + \Delta p_v \tag{3.38}$$

where Δp_v is the incremental pressure due to volume change (or compression process)

The total cylinder pressure increment of Equation 3.38 can also be expressed from the pressure difference between consecutive intervals.

$$\Delta p = p_{i+1} - p_i \tag{3.39}$$

From Equations 3.38 and 3.39 the combustion contribution on pressure rise can be found as follows,

$$\Delta p_c = \Delta p - \Delta p_v \tag{3.40}$$

Assuming a polytrophic compression process, Δp_v can be expressed as

$$\Delta p_v = p_i \left(\frac{v_i}{v_{i+1}}\right)^n - p_i \tag{3.41}$$

where n is polytropic index, and v is cylinder volume. Therefore, cylinder pressure rise due to combustion can be given by,

$$\Delta p_c = p_{i+1} - p_i \left(\frac{v_i}{v_{i+1}}\right)^n \tag{3.42}$$

CHAPTER 4

RESULTS AND DISCUSSIONS

4.1 Introduction

The objective of this research is to investigate early flame characteristics at variable engine parameters. The parameters considered in this study were engine speeds, air/fuel mixture formation (level of stratification or homogeneity) and intake air swirl level variations. It was discussed earlier that early flame development process can be affected by local air fuel mixture condition at the time of ignition and turbulence level of the flow surrounding the developing flame. To make an exhaustive investigation, it requires simultaneous capturing of the developing flame, identification of local air/fuel ratio near spark electrodes and imaging of the turbulent flow field surrounding the spark electrodes. Acquiring all these information on the current CNG DI engine setup was very challenging and some of them might be impossible. Taking into account the conditions and availability of experimental facilities, possible strategies were devised to accomplish the set objectives. First, as many as thirty flame images were captured in every 2 or 3 cycles at a specific crank angle and averaging the acquired information from each to represent the flame at that specific crank angle. As discussed in chapter 3, this can be done by endoscope and intensified CCD camera assembly using the PIV system at a single frame operation mode. Secondly, the air fuel stratification/homogeneity condition was controlled by adjusting fuel injection timing. Early injection (before intake valves are closed) would give stratified mixture, and late injection (keeping the 30° minimum crank angles between the end of injection and the start of ignition to give a minimum required time for mixing) would give stratified mixture. The stratification is further assisted by the piston with a large bowl. The third strategy would be the adjustment of swirl control valve closure angles in order to vary induction swirl levels, and the measurement of the flow was achieved

in a separate setup using the actual cylinder head and a transparent cylinder capable for swirl plane visualization. It is obvious that the nature of the turbulent flow during combustion is the direct result of the tumble and swirl flow structures during induction. In fact, the shape of combustion chamber and piston type can also have tremendous influence on the level of turbulence generated near TDC during compression process [68]. For a pancake type engine the turbulence level is insensitive to the level of swirl at induction and the turbulence intensity can be approximated to be half of the mean piston speed [41].

4.2 Intake Flow Analysis

Intake flow analysis of the engine was performed in different setups using the engine cylinder head and a transparent acrylic glass as discussed in Chapter 3 and illustrated schematically in Figure 3.10. The swirl control valve (SCV) can be positioned at different angle so that the air flow will have different level of swirl when it is introduced into the cylinder. The positions of the adjustable flap in the SCVs for the three different cases of adjustments are shown in Figure 4.1. The left side flap was adjusted and pinned to the appropriate angle, whereas the right side was fixed at the normal design swirl angle (10°). PIV data were collected on both swirl and tumble planes after adjusting the induction swirl levels.
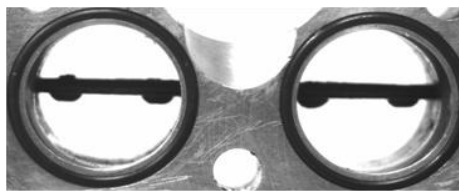
(a) Case-I 10^0 closure of both SCVs (design angle)   *(b) Case-II 50^0 closure (left) and 10^0 closure(right)*
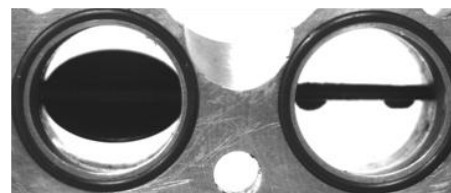
(b) Case-III 90^0 closure (left) and 10^0 closure (right)

Figure 4.1   Left and right adjustments of SCV angles in the divided port as viewed from the intake side

4.2.1 Swirl Plane Analysis

The swirling flows were created around the valve stem inside the port due to deflection of the flow by the adjustable disc in the SCV. This can be observed by the streamlines and swirl strength maps of the air flow just downstream from the valves shown in Figure 4.2. The left side valve was the one with SCV adjusted at variable closing angles to vary swirling flows and the right side valve was with the SCV fixed at 10^0 closure angle as illustrated in Figure 4.1. The created swirling flows were observed in Figure 4.2 (b) and (c) just downstream of the left valves in medium swirl and high swirl adjustments. The medium tumble induction adjustment is a tumble intake with some degree inclination towards the swirl plane. Though small vortices might show up, there was no clearly observed swirling flow structure near to the intake valves or further downstream (that explained later) in the cylinder for Case-I induction strategy (medium tumble adjustment).

(a) Medium tumble induction

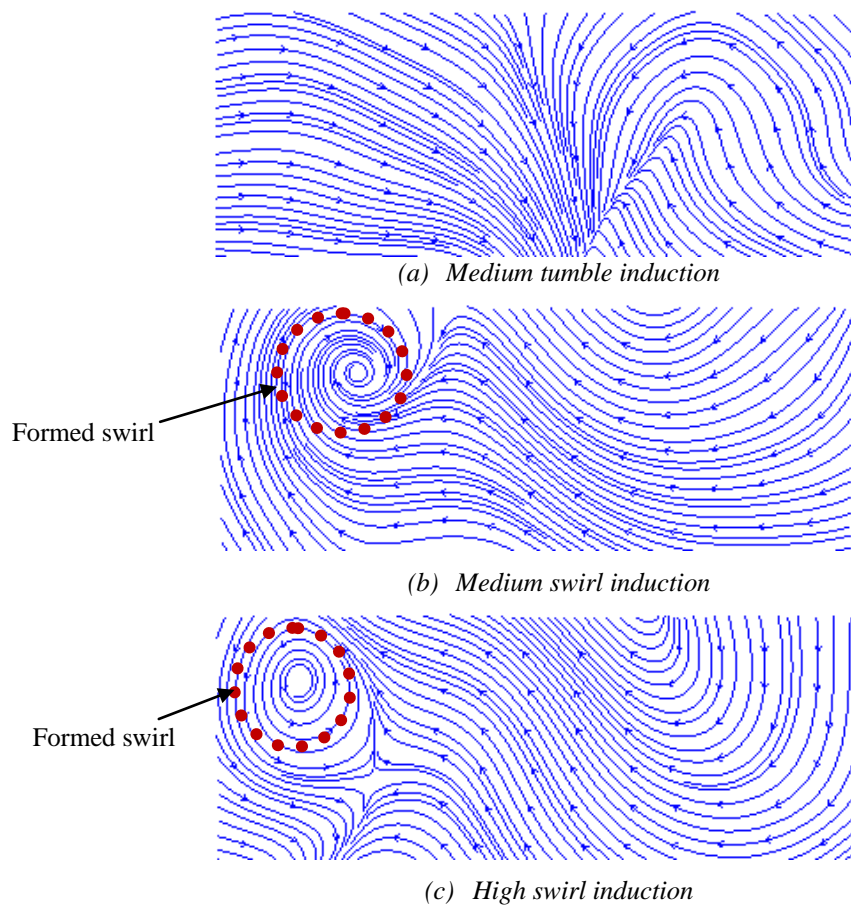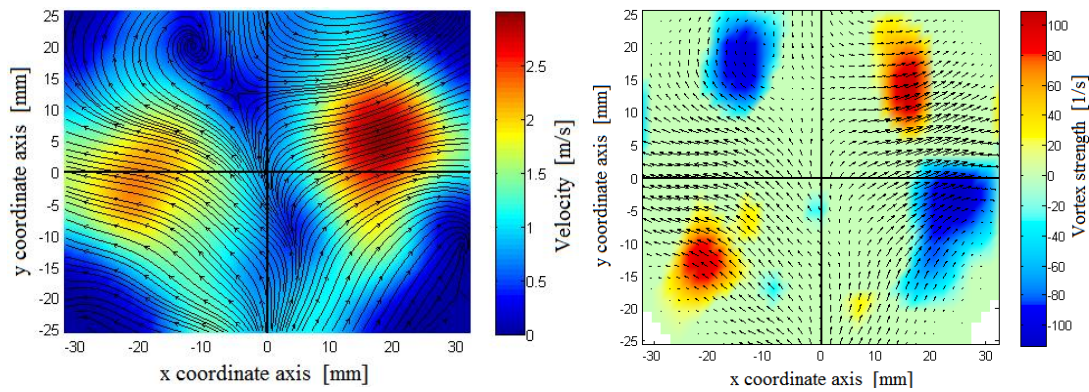*(b) Medium swirl induction*

(c) High swirl induction

Figure 4.2   In-cylinder flow streamlines generated from PIV data at the three different swirl inductions on a swirl plane 10 mm downstream from the valve seats

71

The medium tumble intake as described earlier was a 10^0 closing of the SCV that gives the tumble flow some degree of inclination. Figure 4.3 shows flow characteristics at swirl planes of 10 mm and 40 mm downstream from valve seats for the medium tumble induction. In this figure, it was noticed that small scattered vortices (clockwise and counter clockwise vortices) were created and observed on the swirl plane even at this low swirl angle adjustment of the SCV. These vortices were locally circulating flows at different regions of the sampling plane identified from the local velocity gradient tensor using Equations 3.6 to 3.11. However, there was no clearly identified coherent swirling structure in this induction strategy even further downstream of the flow as shown in Figure 4.3.
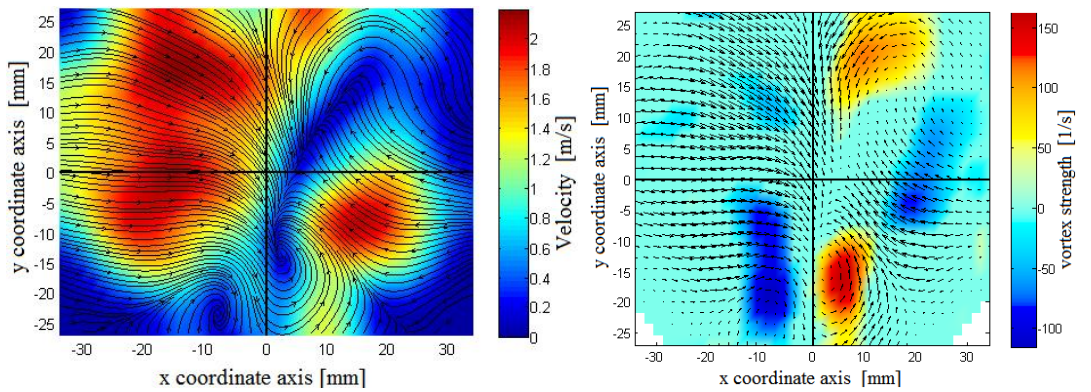
(a) Streamlines and located vortices at 10 mm downstream from valve seats

(b) Streamlines and located vortices 40 mm downstream from valve seats

Figure 4.3 Streamlines (left) and vortices (right) for a medium tumble induction at two different swirl planes
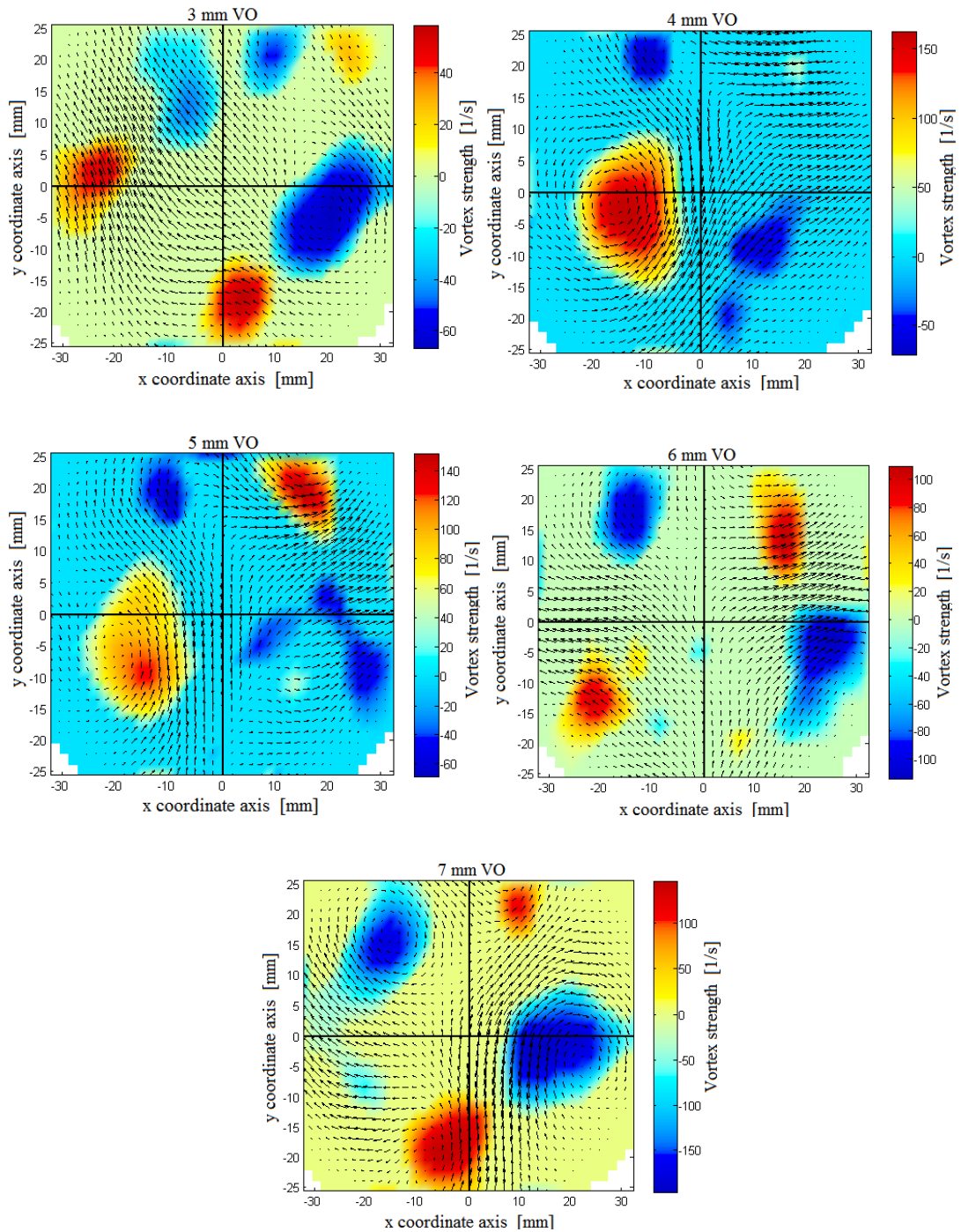
72

Figure 4.4   Vortices created on a swirl plane 40 mm downstream from valve seats in medium tumble induction at variable valve lifts

Up to 2 mm valve open, no PIV signals captured due to the very low flow of air through valves into the cylinder at all swirl induction levels. Figure 4.4 shows that at 3 mm opening, more than one small clockwise and counter clockwise vortex cores were noticed (a core size of about 5 mm radius). With higher valve lifts, the number

of vortices observed on the swirl plane seemed dropped and at full valve opening, clearly distinguished strong and large vortex core were observed. In the actual engine flow, valve lift moments happen in a single induction. Hence, there would be formations of many small-sized vortex cores on the swirl plane of the medium tumble induction process. There could be also possibilities that vortex cores of the same direction could be amalgamated into a bigger and stronger single vortex.

In the other two cases of induction strategies, medium and high swirl angle adjustments, the swirling structures on the swirl plane were organized and clearly observed in all valve lift positions. Smaller diameter of circulation was observed near to the valve seat on the side of the adjustable SCV portion. This circulating flow increased its core size downstream in the cylinder and it was also tilted to the other side of the cylinder, as shown in Figure 4.5. The shape of the circulating flows was different from each other. The swirling flow of medium swirl induction was compact and seemed circular as it was observed downstream of the flow, whereas the swirling flow structure for the high swirl adjustment was somehow elliptical.

(a) Swirl plane at 10 mm from valve seat for medium swirl (left) and high swirl (right)

(b) Swirl plane at 40 mm from valve seats for medium swirl (left) and high swirl (right)
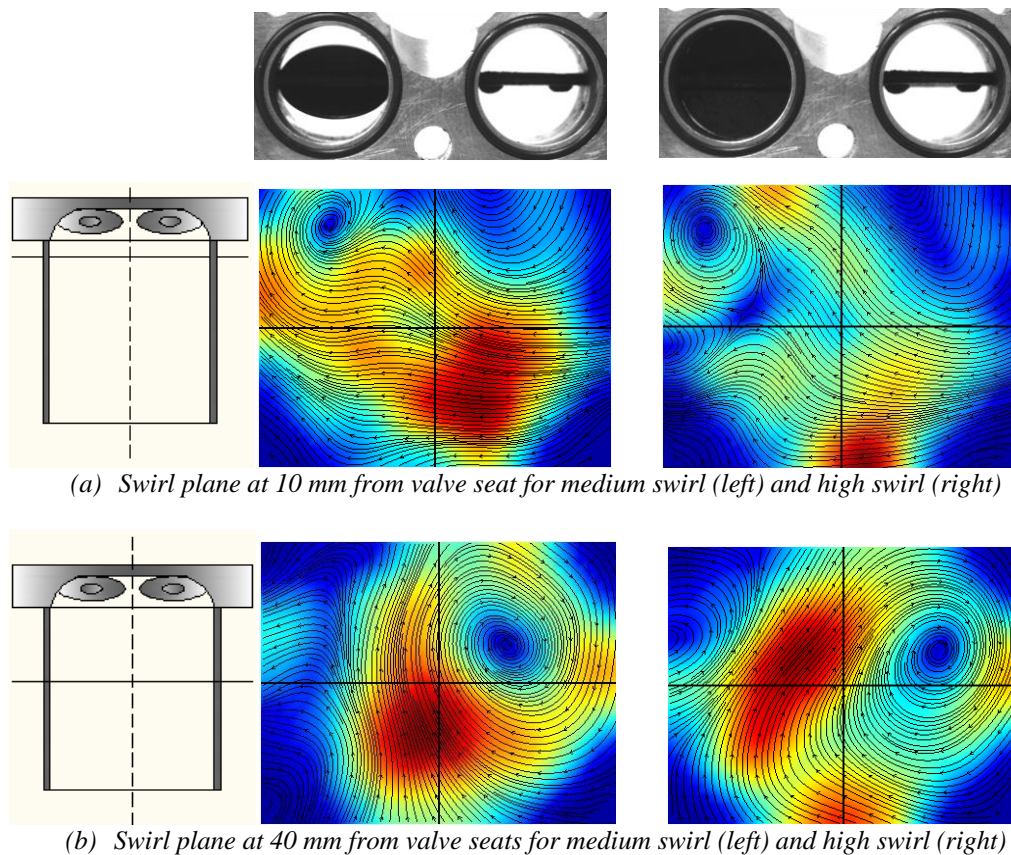
Figure 4.5   Flow Streamlines for medium and high swirl induction at two levels of swirl with schematics showing plane positions in the cylinder and adjustable portion of SCV

74

Swirl velocity fluctuation profiles are shown in Figure 4.6 (a) to (c) measured on the swirl plane (40 mm down from valve seats) along a line (y=0) for the variable induction cases at different valve lifts, while Figure 4.6 (d) shows the same velocity profile at maximum valve lift (7 mm). The legends in the figures indicate induction type and level of valve opening. (For instance, MT4 means medium tumble at 4 mm valve opening). In all cases strong periodic fluctuations on swirl velocity were observed due to the existence of vortices on the flow plane. The magnitude of the swirl velocity increased with valve lifts in all induction cases. The lower and upper peaks of the velocity profiles shown in the figures demonstrated the existence of vortices on the measurement plane as velocity magnitude dropped from the periphery towards the swirling core center. The profiles might be useful to identify the number of swirling vortices and their core sizes as well. Based on this, the swirl core size can be taken to be the distance between the maximum and the minimum velocity measured along the core (minimum velocity measured at the center of the core) as discussed in [69]. So, in this case, as it was shown in Figure 4.6 (d), the high swirl induction adjustment acquired the highest swirl core size, compared to the medium swirl induction strategy. In the case of medium tumble induction there was no distinct swirling motion, but disintegrated and scattered vortices. The four high and low peaks of velocity values in the case of medium tumble induction, as shown in Figure 4.6 (d), indicated at least two strong and smaller vortex cores on both sides of the cylinder axis existed. Hence, this might lead to a conclusion that the size of swirling cores created by swirling induction increased with the increase of SCV closure angle.
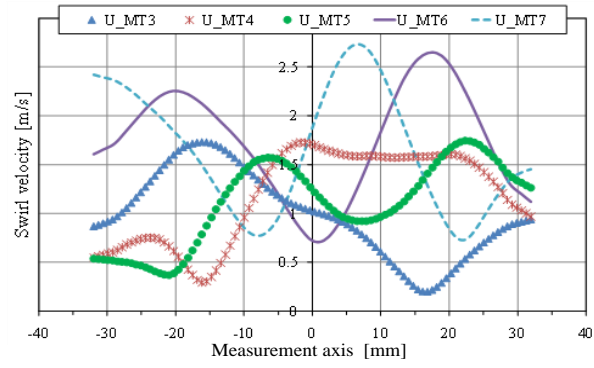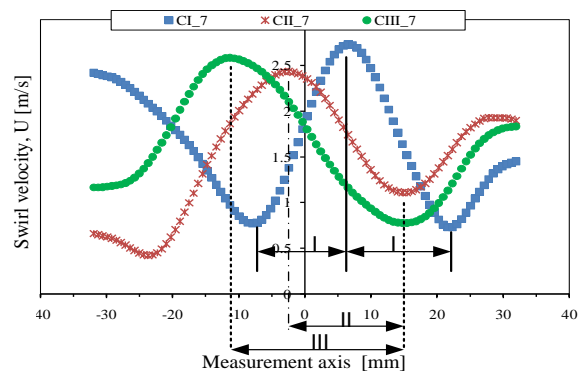
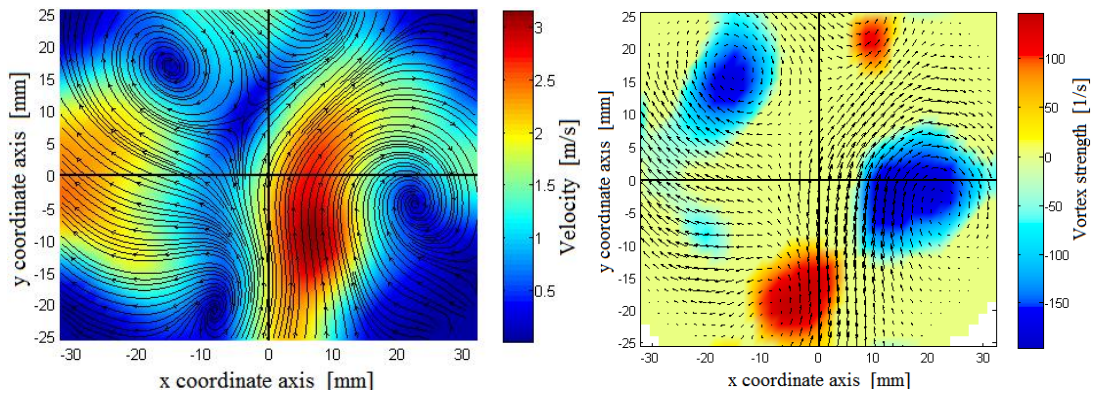*(a) Medium tumble induction*
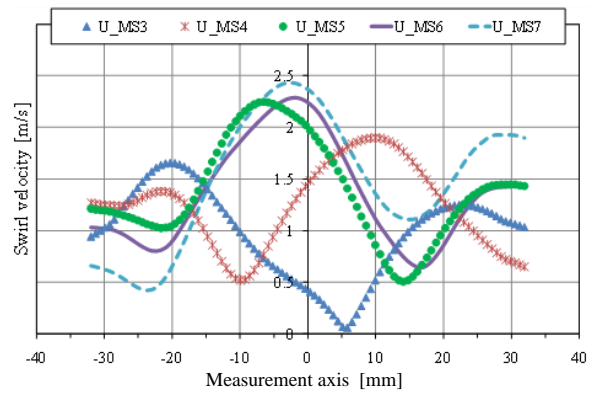
(b) Medium swirl induction
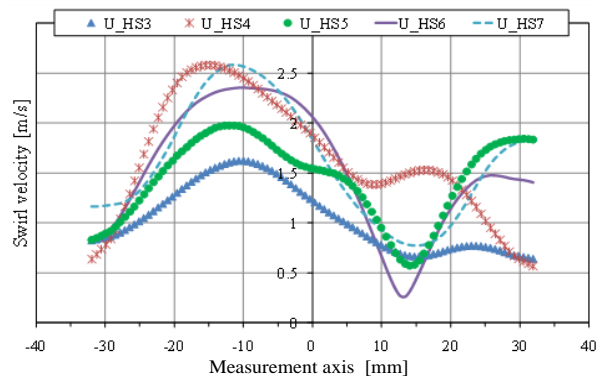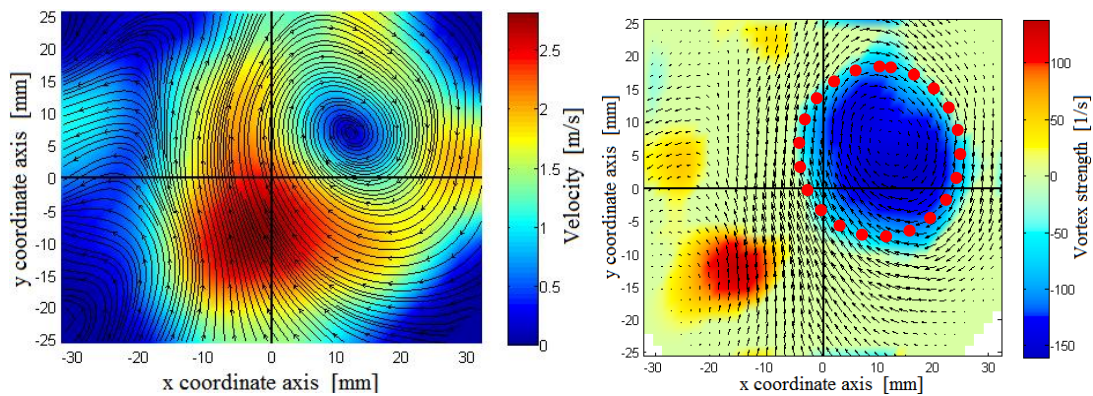

(c) High swirl induction

(d) The three induction cases at maximum valve lift (7 mm)

Figure 4.6   Velocity profile along a line y = 0 on a swirl plane of 40 mm down from valve seats in the cylinder for the three different induction cases extracted from the vector fields

76

Figure 4.7 depicts streamlines and swirl strength map at the maximum valve lift (7 mm) for the three induction strategies. The swirling cores can be observed visually for the second and third induction cases. In this case, medium tumble induction showed strong and compact core with 2.7 m/s velocity at the periphery of the core. The core size was larger in the case of high swirl induction, but the swirl strength was dispersed and weaker along the major axis of the ellipse-like swirl structure. The core center had an offset from the center of the ellipse along the major axis. Since the swirl angle adjustments of the two intake ports were different, as demonstrated in Figure 4.1 (c), the swirl core created by the high swirl angle adjustment portion of the inlet valve was weakened and eroded by the relatively strong tumble intake flow from the other portion of the inlet valve. The strength of the strain might decide the survival of the vortex. The strain parameter can be identified from the ratio of the strain deformation characteristics time and the vortex rotation characteristics time, and the faster of the two may decide the feature of the swirling vortices. On the other hand, as shown in Figure 4.7, the almost circular and closed stream lines made the vortex created by the swirling flow of medium swirl adjustment more compact. Even though the core centers of both cases had the same swirl strength, the regions covered by this strong swirl was different. In the high swirl induction, the swirl strength decreased faster along the core from the center towards the periphery.
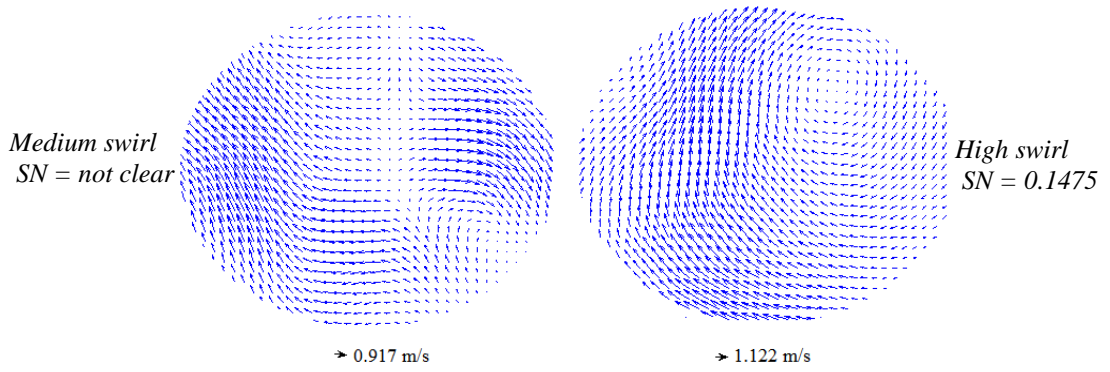
(a) Medium tumble induction
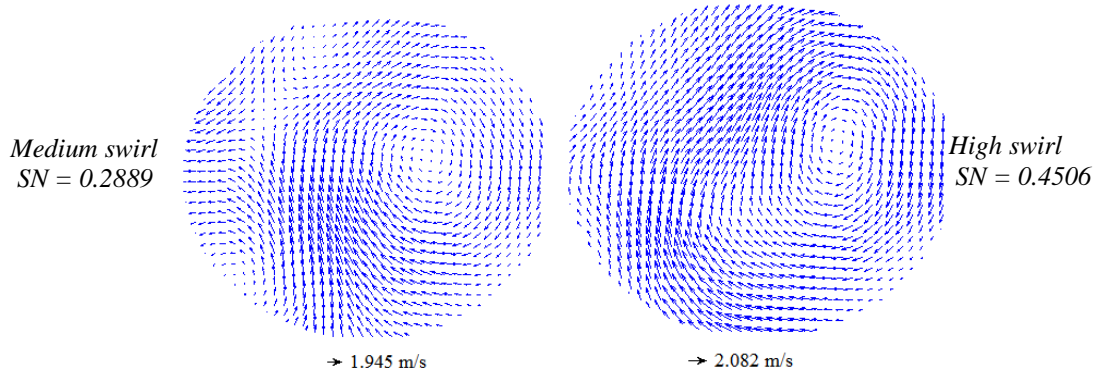
(b) Medium swirl induction
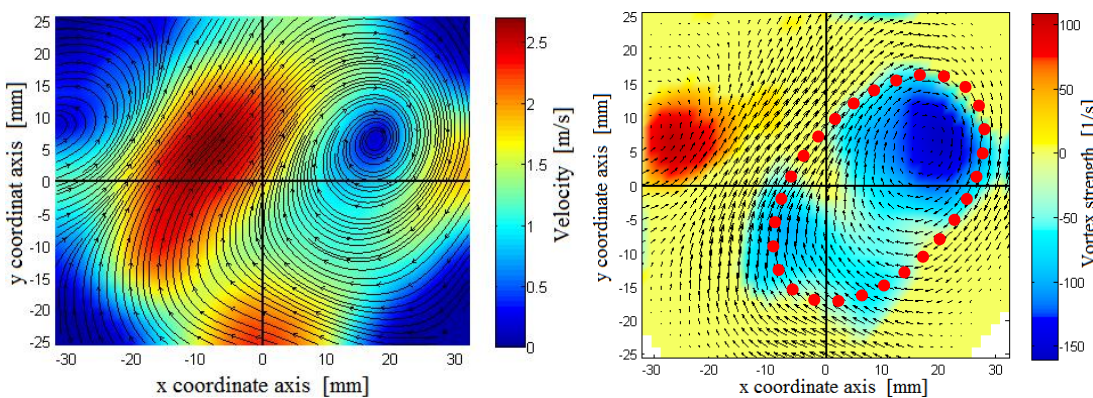
(c) High swirl induction

Figure 4.7   Stream lines and color bars for velocity magnitudes (left-side plots) and velocity vector field arrows and color bars for vortex location (right-side plots) at different induction cases
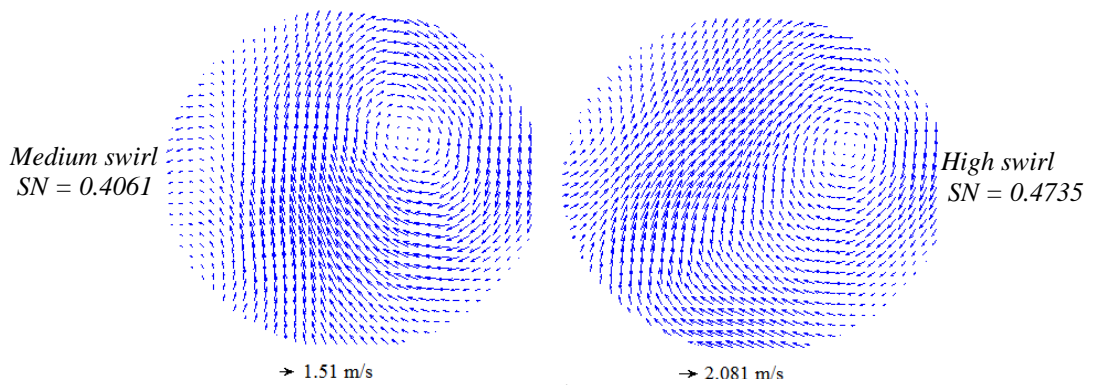
The swirl number, which is a dimensionless number used to characterize swirl intensity, was identified from the ratio of tangential and axial moments of momentum as discussed in [70]. The swirling axis considered was the axis that passes through the center of the swirl core. It is shown in Figure 4.8 that swirl intensity increases with valve opening. The high swirl valve adjustment induction case has shown the highest swirl intensity level.
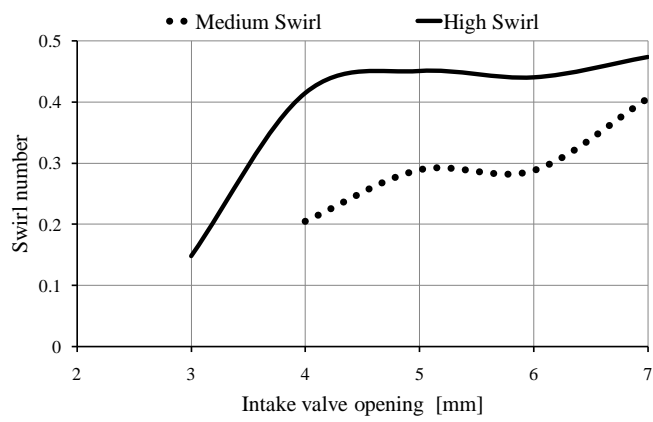
Medium swirl
SN = not clear

High swirl
SN = 0.1475

→ 0.917 m/s   → 1.122 m/s

(a)   3 mm valve opening

Medium swirl
SN = 0.2889

High swirl
SN = 0.4506

→ 1.945 m/s   → 2.082 m/s

(b)   5 mm valve opening

Medium swirl
SN = 0.4061

High swirl
SN = 0.4735

→ 1.51 m/s   → 2.081 m/s

*(c)   7 mm valve opening*

(d)   Swirl number verses intake valve opening

Figure 4.8   Swirl number verses intake valve opening

Root-mean-square (RMS) values of the velocity can indicate the level of turbulence in the cylinder. The velocity fluctuations (temporal and spatial) were observed in the RMS analysis of the variable induction cases. The RMS values were calculated from the total repeated velocity data of the flow at each set parameter. These values gave information on how the velocity fluctuated temporally at specific point and spatially as well on the measurement plane. Figure 4.9 shows the u and v RMS velocity fields on the swirl plane of the three different induction cases near to the middle of the cylinder (40 mm down from valve seats). In the medium tumble induction case, Figure 4.9 (a), high RMS was recorded along the vertical center of the sampled plane (from the side of the intake valves towards the side of exhaust valves), whereas in the other two induction cases, high RMS values dominated the left side of the cylinder where SCV has the highest closure angle of the two positioned. In fact, the center of the swirl core was located on the right side of the cylinder axis on this specific sampled plain. This indicates that the region with high velocity magnitude could be a region of high RMS values. The RMS values of the y-component velocity in Figure 4.9 (v_{RMS}) show the presence of strong velocity fluctuations on that axis v over the sampled regions in all cases of inductions. The v component of the swirl velocity is greater in magnitude than the u component as well. This high velocity values of the y-component occurred due to the direction of the bulk intake flow because of the tumble angle of the port which has 21.4^{o} inclinations from the vertical z-axis as shown in Figure 4.10.   On the other hand, the maximum value of velocity fluctuation on the swirl plane under consideration was seen declining with increasing SCVs closure angles. For the first induction case (medium tumble induction) the maximum recorded RMS value was 2.5 m/s, for the medium swirl induction case it was 2.2 m/s and the high swirl adjustment case it was found to be 1.6 m/s. This was directly related to the declined flow velocity due to resistance for the flow in relation to the adjustment of SCVs which eventually could affect the volumetric efficiencies of the induction process. The other reason perhaps is that intake flow at medium tumble adjustment consisted of many clockwise and counterclockwise rotating vortices. This could lead to high velocity fluctuations both spatially and temporally on the swirl plane. The medium and high swirl intake flows, on the other hand, can be characterized by their coherent swirling structure with relatively lower fluctuation.
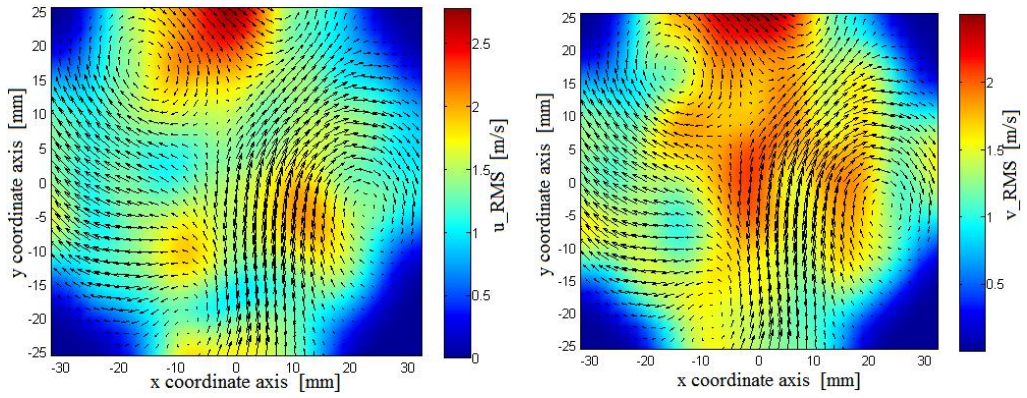
(a) Medium tumble induction
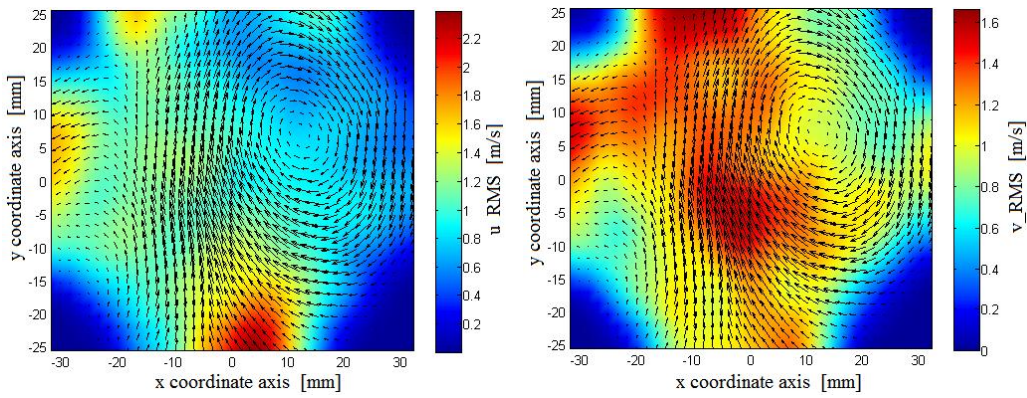
(b) Medium swirl induction
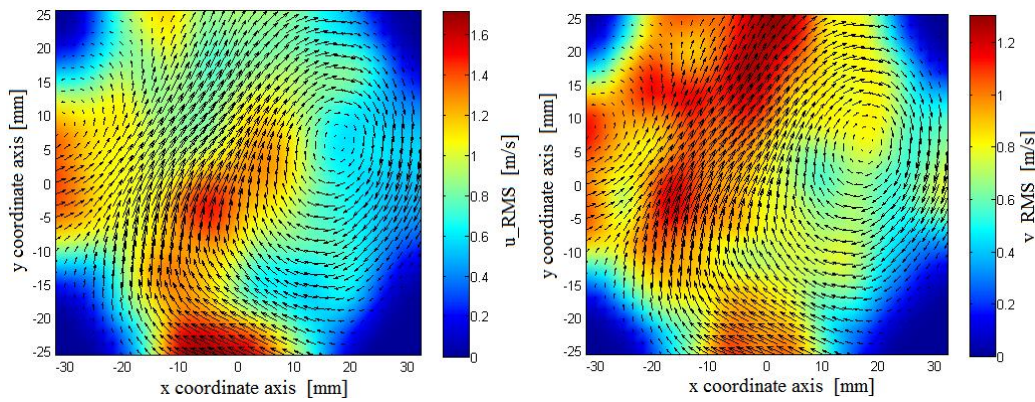
(c) High swirl induction

Figure 4.9 RMS fields of the x and y velocity components (the colored field) and velocity vector fields (the arrows) for the variable induction cases at 7 mm valve
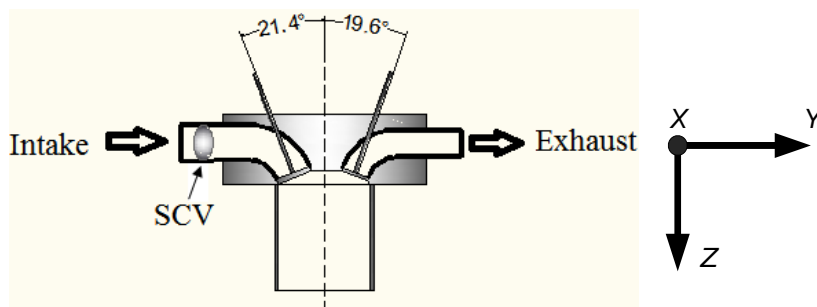

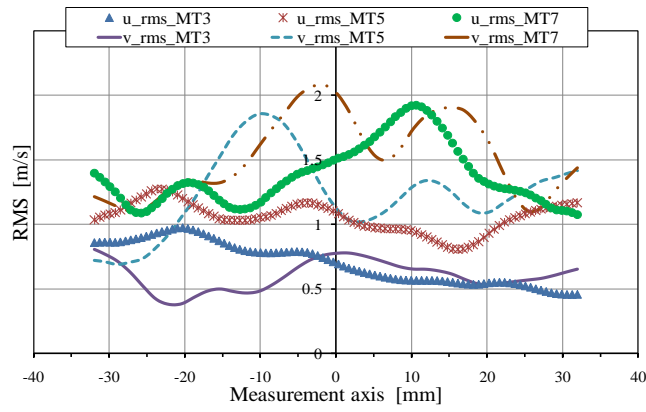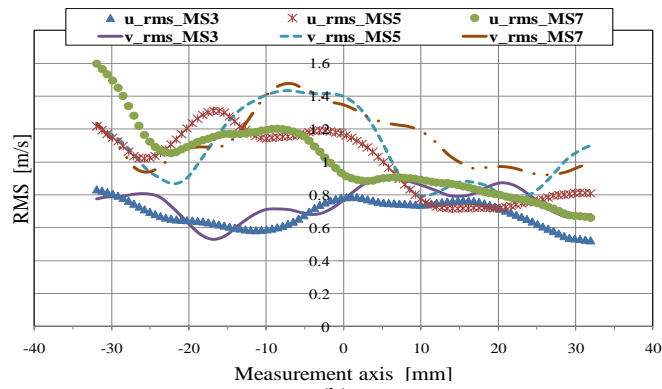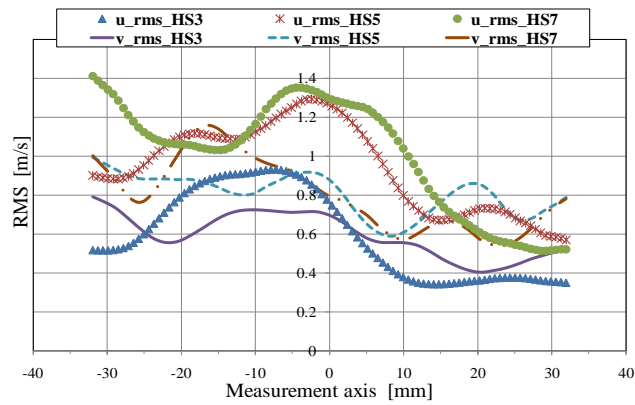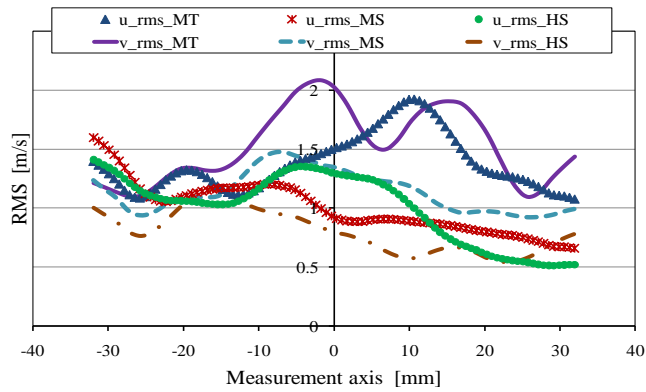*Figure 4.10 Intake and exhaust valves position in the head-cylinder assembly*

(a)

(b)

(c)

(d)

Figure 4.11   RMS values along a line y = 0 on a swirl plane located 40 mm down from the valve seats in the cylinder

82

The RMS values at 40 mm downstream from the valve seat on the swirl plane sampled along a line ($y=0$) were plotted in Figure 4.11. Its value for both velocity components in the radial direction of the sampled plane showed variations. At 3 mm intake valve lift, the variation along the sampling line was not much for medium tumble but with more opening of the intake valves its magnitude and spatial fluctuation became high. On the other hand, medium swirl and high swirl inductions showed RMS values of u and v velocity components on the swirl plane that has higher values on one half of the cylinder and lower on the other half. The higher values were recorded on the side of the valve with the adjustable SCV, and lower values on the swirling core center region side. Flow RMS values are related with the velocity magnitude and the level of turbulence as well. Therefore, this flow analysis indicates that the turbulence level of the medium tumble induction is the maximum of all the three induction levels. Medium tumble induction might have the highest turbulence decomposition in the early stage of compression. The structure of the tumble flow can be susceptible for easy decomposition during compression. Arcoumanis et al. [71] observed in their study of in-cylinder flow in a combined swirl/tumble induction that the tumble structure was broken down in 90° to 60° BTDC during compression process, whereas the swirl flow structure still existed at 20° BTDC. The works of [14] and [40] also discussed on the higher rate of decomposition of the tumbling flow structure during compression process. Geometrically the cylindrical combustion chamber can be convenient for a swirling flow structure so that it can persist longer during compression process. Depending on the swirl strength and its compactness observed in the current study, the medium swirl could stay longer than the high swirl induction case that had weak periphery and elliptic swirling core. The nature of rate of decomposition for the high swirl seems to be in between the medium tumble and the medium swirl induction case.

4.2.2 Tumble Plane Analysis

On another observation, the intake flow structure of Case-I induction strategy on the tumble plane was observed to exhibit coherent circulating flow structures about an axis perpendicular to cylinder axis. These tumble flow structures had clockwise

rotational direction in all cases of valve opening as shown in Figure 4.12. The vortex core created by the tumble circulation seemed moving from the center of the cylinder axis at lower valve lifts towards the left side of the cylinder at the higher valve lifts. At 3 mm valve lift more than one weak vortex cores were observed. The more the valve lift the lower the number of vortices and the stronger the circulation became. This tumble flow structure can be easily disintegrated into smaller eddy sizes during compression process in the engine; similar observation was also reported by Heywood [14].
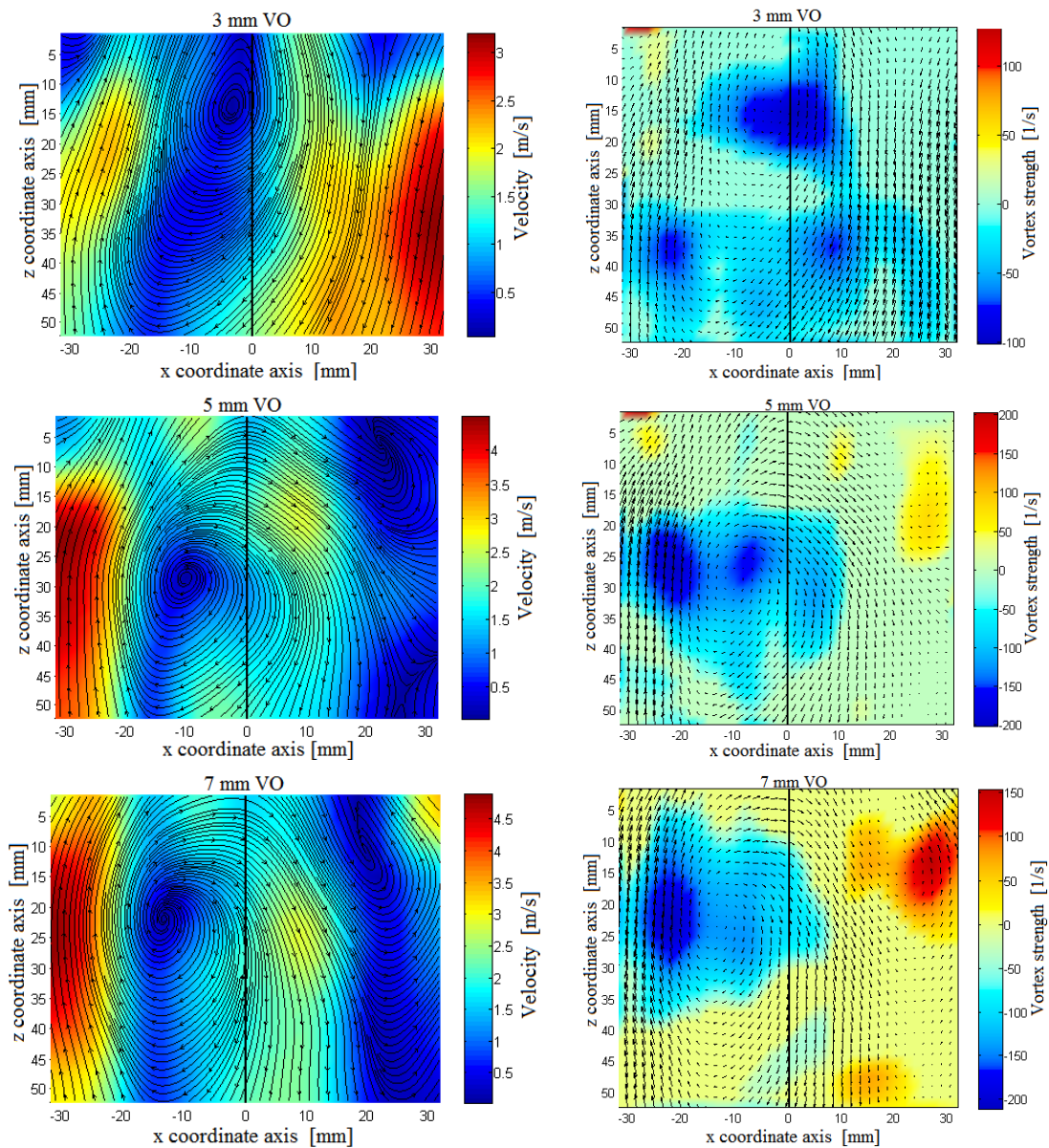

Figure 4.12   Streamlines (left) and vortex strength (right) of medium tumble induction on a tumble plane at 3 mm, 5 mm and 7 mm valve opening

The results of the flow analysis for both swirl and tumble planes were compared in Figure 4.13 to 4.15. The velocity profiles that are shown in Figure 4.13 indicate that the maximum velocity values were recorded in the tumble plane in all induction cases, and the medium tumble induction was the maximum of all. This was obvious that the mean bulk flow should be axially down in the cylinder. For medium tumble intake, Figure 4.13 (a), the velocity profiles for both planes were similar, whereas on the medium and high swirl inductions there was a swirling flow on the swirl plane (the horizontal plane of the cylinder) that could reduce the flow velocity on the tumble plane. That can be seen in Figure 4.13 (b) and (c). Up to a maximum of 3.5 m/s velocity was recorded on the tumble planes of medium swirl and high swirl, and up to 5 m/s for the medium tumble.
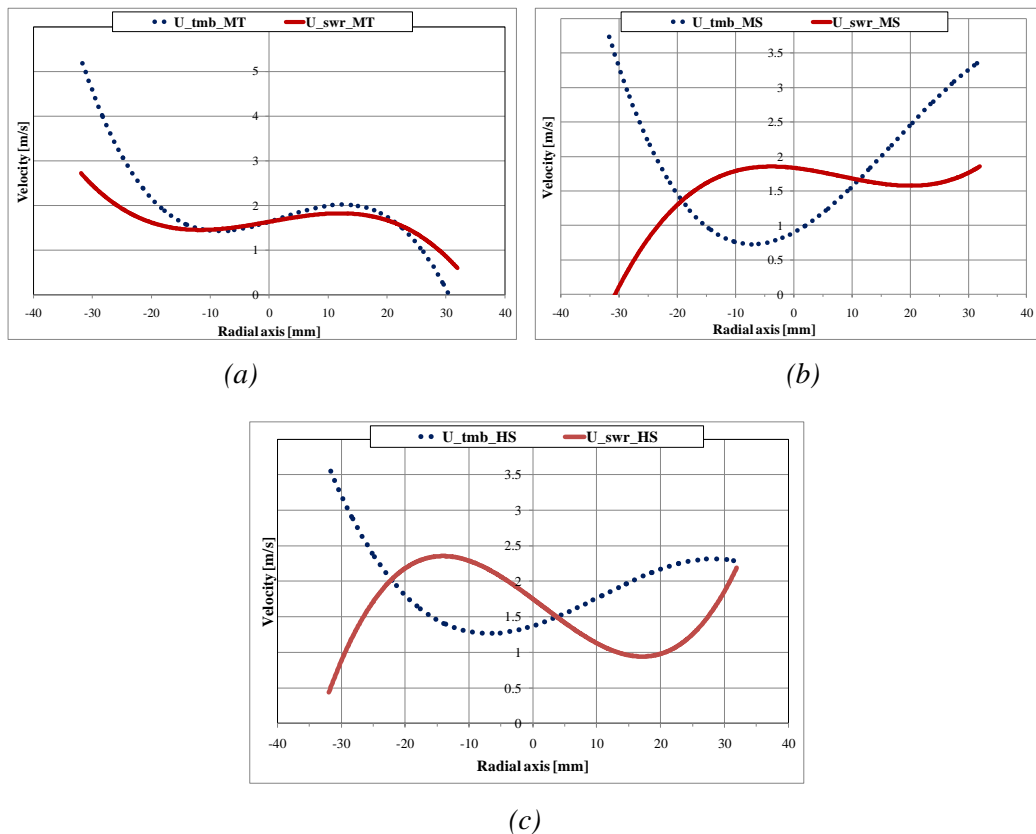

(a)   *(b)*

(c)

Figure 4.13   The swirl and tumble velocity at 40 mm downstream in the cylinder extracted along a common line for both planes on the x-axis

(a)

(b)

(c)
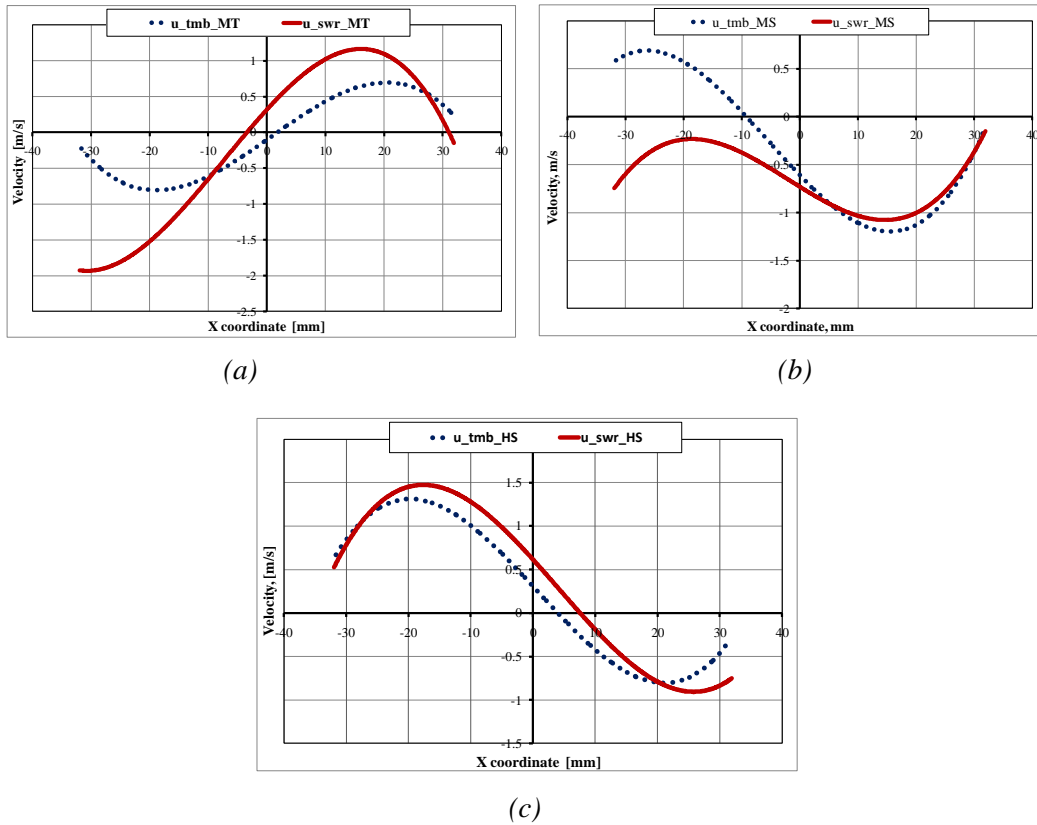
Figure 4.14 x-coordinate velocity component on both swirl and tumble planes

The x-axis is a common coordinate axis for both swirl and tumble measurement planes. Therefore, x-component of the average velocity on the swirl and tumble plane should be the same. This was shown in Figure 4.14. The discrepancy between u_swirl and u_tumble on all induction strategies seemed dependant on the u_{RMS} values of both planes shown in Figure 4.15.   Hence, the u velocity component for high swirl induction case (with lower RMS values of all induction cases) showed more similar velocity records on both swirl and tumble planes. Since the data acquisition took place at different time on the planes, there could be calibration and imaging errors too.

(a)

(b)

Figure 4.15   u component RMS values for (a) swirl plane (b) tumble plane

86

4.2.3 PIV Measurement Validation
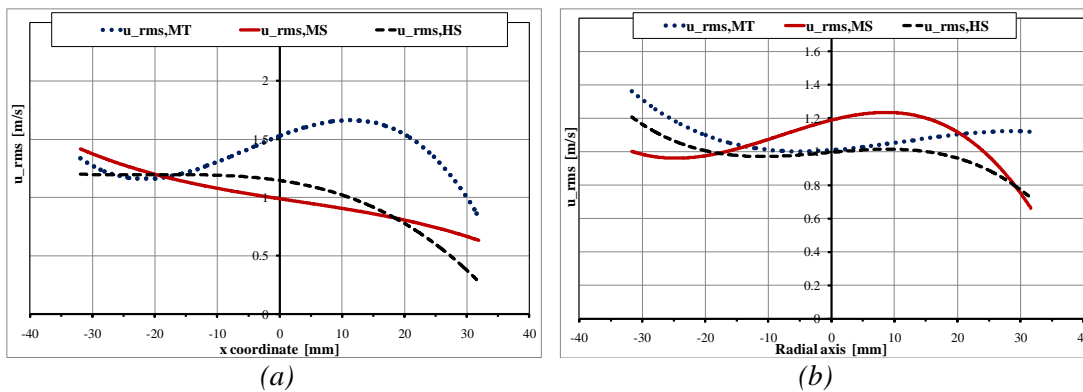
The PIV measurement system needs to be validated for its accuracy. For this purpose, a simple measurement validation procedure was performed using a small disc with a diameter of 70 mm, having a black background and uniformly scattered white dots shown in Figure 4.16. The disc was pinned to a shaft rotating at 1494 rpm. The displacement of the dots and their linear velocity vector, while rotating, was measured and analyzed using a PIV setup with a similar procedure to the one used for the induction flow analysis, and generates velocity vectors portrayed in Figure 4.16b. The velocity values along a line that passes through the center of the measurement plane were extracted from the PIV measurement. In a similar fashion, the velocity values on the same line were identified analytically as a function of rpm and radius using Equations 4.1 and 4.2. Figure 4.17 shows the velocity values extracted from the PIV measurement and analytical calculation, for which:

$$U = r\omega \tag{4.1}$$

$$\omega = \frac{N\pi}{30} \tag{4.2}$$

where N is rotational speed in rpm, r is radial distance

The two measuring techniques were compared using the root-mean-square deviation (RMSD) that was calculated from the two sets of velocity values. The RMSD value was identified using Equations 4.3 and 4.4, and it was found to be 0.45 m/s. The normalized RMSD value indicates that the PIV system showed 91% measurement accuracy when compared with the direct calculation method.

$$U_{cal} = \begin{bmatrix} U_{1,1} \\ U_{1,2} \\ . \\ . \\ . \\ U_{1,n} \end{bmatrix} \qquad U_{PIV} = \begin{bmatrix} U_{2,1} \\ U_{2,2} \\ . \\ . \\ . \\ U_{2,n} \end{bmatrix} \tag{4.3}$$

$$RMSD(U_{cal}, U_{PIV}) = \sqrt{\frac{\sum_{i=1}^{n}(U_{1,i}-U_{2,i})^2}{n}} \tag{4.4}$$

(a)   (b)
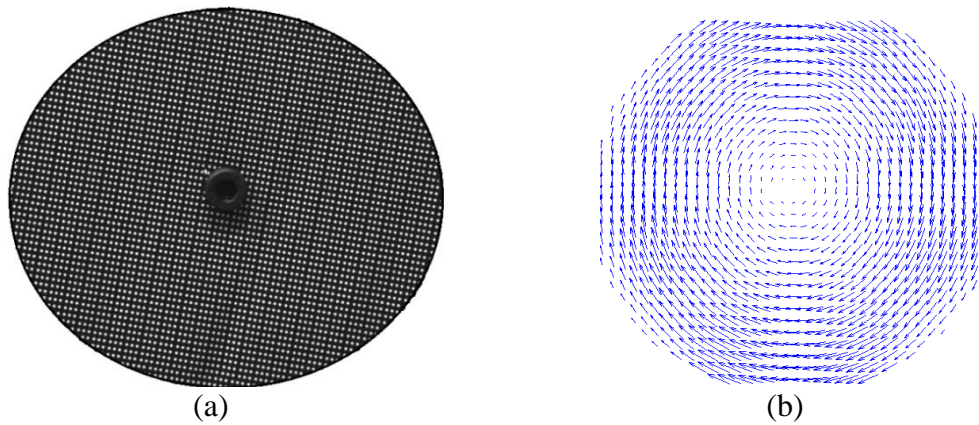
Figure 4.16   PIV validation system (a) rotating disc, and (b) velocity fields on rotating disc generated by PIV system
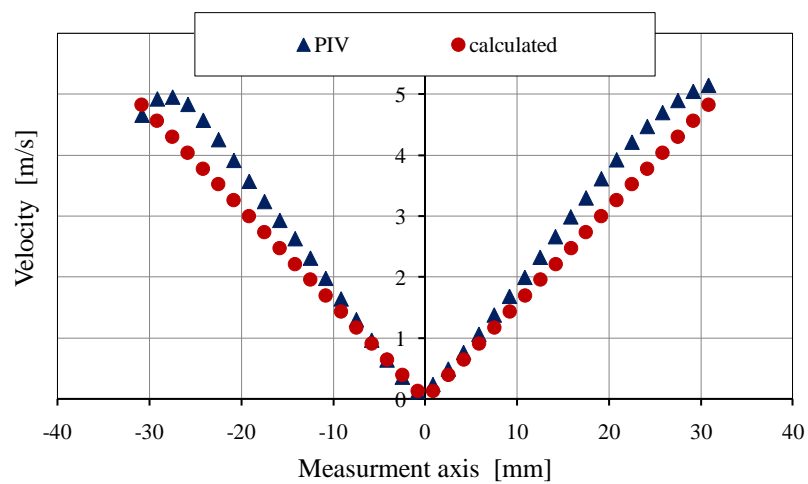
Figure 4.17   Velocity along radial lines identified using PIV and analytical methods

4.3 Early Flame Analysis and Discussion

The flame characteristics considered for analyses are flame wrinkles level, flame distortion level, position and displacement of the flame relative to spark center. Finally, flame growth rate which is mainly the result of the aforementioned parameters is discussed. The analysis is observed under major category of stratified and homogeneous combustion cases. Engine speeds and induction swirl variations are the adjustable parameters.

88

4.3.1 Stratified and Homogeneous Combustion

Stratification of air-fuel mixture is the formation of rich or stoichiometric air-fuel mixture near to spark plug electrodes at ignition timing, and farther away from the spark center the mixture can be leaner or no fuel at all. The stratified mixture can be achieved via fuel injection late in the compression process. The objective of stratification in a direct injection engine is to operate the engine at overall lean combustion in part load unthrottled condition that can not be achieved in a lean homogeneous combustion. This operation is able to improve the BSFC (brake specific fuel consuption) of the engine, and reduce molecular dissociation due to its lower cycle temperature. On the other hand, homogeneous air/fuel mixture can be achieved via injection of the fuel earlier than the intake valve closing time.

In the current study, both stratified and homogenous combustion modes were considered. Injection timing for the stratified combsution was set at 90° BTDC, and for the homogeneous combustion 180° BTDC. For an ignition timing of 38.5^{o} BTDC the selected injection timings were believed to create the necessary stratification or homogeniety in the cylinder at the time of ignition.

4.3.2 Flame Wrinkles

Flame surface wrinkles characteristic with varying engine speed at the different induction and combustion mode were analyzed. Figure 4.18 shows level of wrinkles (measurement was discussed in Section 3.3.3.5) at medium tumble induction for the variable speeds of stratified and homogeneous combustion modes. In this induction strategy, flame wrinkles were shown to be a function of motor speeds. The highest engine speed i.e. 1200 rpm showed the highest wrinkling effect. At all motor speeds under consideration the value of standard deviation (STD) for wrinkles measure increased and reached the maximum before it started to decline. Where the engine was at the highest speed, it was faster to reach the maximum wrinkling level within the development period. In this specific combustion case, the wrinkles level was the lowest at the lowest speed i.e. 1500 rpm. The maximum STD recorded at this induction case was 0.23 mm, which was at 1800 and 2100 rpm. Hence, it is evident

that in medium tumble stratified combustion higher engine speeds increases flame surface wrinkles.
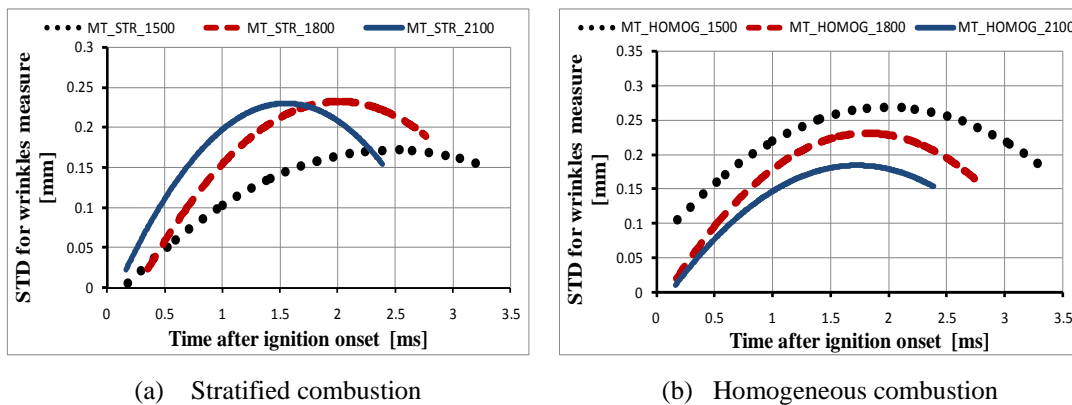

| (a)   Stratified combustion | (b)   Homogeneous combustion |

Figure 4.18   Flame wrinkles level for medium tumble at different engine speeds

The flame wrinkle characteristics for homogeneous combustion case of the same medium tumble induction were completely different from the stratified one as indicated in Figure 4.18 (b). In this case, the lowest engine speed was in favor of better wrinkling than the higher speeds. The trends of the curves were the same for both combustion modes, but the homogeneous combustion showed higher level of wrinkles than the stratified case, that was at 1500 rpm. At the speed of 1800 rpm, the wrinkling behavior was almost the same in both combustion modes, whereas at 2100 rpm the STD values dropped. The maximum recorded STD for wrinkles measure in the homogeneous combustion case was 0.27 mm, which is higher than the one recorded in stratified case. Hence, it can be concluded that an increase in engine speed does not favor a better flame wrinkling in a medium tumble induction homogeneous combustion.

The local air/fuel ratio at the vicinity of the spark electrode in the stratified combustion was near stoichiometric, whereas in the case of homogeneous combustion the local air/fuel ratio was the same with the overall ratio. The measured overall air/fuel ratios for stratified and homogeneous combustion were 2.0 and 1.4, respectively. It can be observed that the early flame of a stratified combustion grew in a richer air/fuel mixture compared to the homogeneous combustion case. Arcoumanis and Kamimoto [17] elaborated that lean mixture can exhibit higher degree of wrinkledness because the burn rate can be lower than the wrinkles rate due to

turbulence effect. On the other hand, Heim and Ghandhi [72] investigated in-cylinder flow characteristics at variable engine speeds and showed that engine speeds and turbulence intensities had linear relationships. The rise in engine speeds can increase in-cylinder turbulence intensity, and the intensity level of the turbulent flow increases degree of wrinkledness [49]. Therefore, the wrinkles level of the early flames shown in Figure 4.18 could be the result of the tradeoffs between the mixture leanness and the level of turbulence created due to engine speed variation at fixed induction condition. It can be seen from the results that the maximum wrinkles level observed on the early flames was shown in the homogeneous combustion case at 1500 rpm. In the case of stratified combustion where the local air/fuel ratio in the spark electrodes region was constant, an increase in the engine speed was shown to increase the level of wrinkles (Figure 4.18 (a))

In a medium tumble induction, the effect of change in motor speed on flame wrinkling capability was dependant on the mode of combustion (stratified or homogeneous). And it was discussed that the increase in motor speed favored higher wrinkling in stratified combustion case, whereas in the homogeneous combustion case the reverse happened. Next, effect of speed change on the two combustion modes by varying the induction strategy would be discussed; first, medium swirl and then, high swirl. In this case the medium swirl and high swirl definitions are as discussed in Section 3.2.2.

Figure 4.19 (a) shows the STD values of stratified combustion medium swirl induction case. The high engine speeds still favor better wrinkles just like in the medium tumble of the same stratified combustion. The only variation in this case is the magnitude of wrinkles dropped especially for the highest speed (1200 rpm). Formation of wrinkles at 1500 rpm engine speed is not affected by the change in swirl level of the induction.
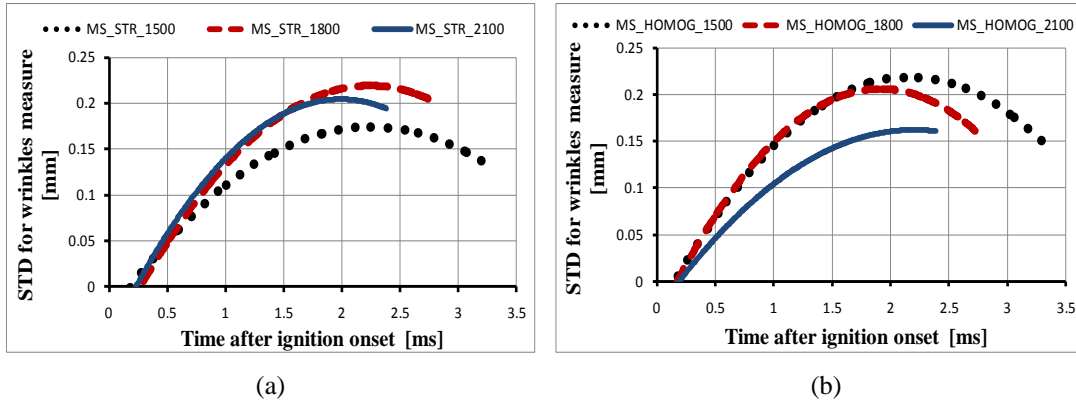
Figure 4.19   Flame wrinkles level for medium swirl (a) stratified combustion (b) homogeneous combustion

The STD values for homogeneous combustion mode of a medium swirl induction case are shown in Figure 4.19 (b). In this case, the lower speeds were still in favor of high wrinkles; but, similar to the stratified case discussed earlier, the maximum recorded STD values dropped. The first two speeds (1500 and 1800 rpm) show similar wrinkles characters up to 2 ms after ignition timing. When the speed is further increased to 2100 rpm, the STD values drastically dropped. Hence, from Figure 4.18 and 4.19 it was understood that the change of induction strategy from medium tumble to medium swirl did not change the effect of speed variation on flame surface wrinkles for the respective combustion modes, but the maximum STD values recorded dropped from the former value for both combustion modes. This could be related to the level of turbulence intensity created at the time of combustion or near to TDC during compression process. It is discussed in Section 4.2 that the medium swirl induction process created a large and strong swirling core relative to the medium tumble and high swirl inductions, which was shown in Figure 4.7. Decomposition (or decaying) rate of the swirl core created in the medium swirl induction was lower compared to the other two cases in the compression process as observed also by [14] and [40]. Hence, the formation of small scale turbulence that can be responsible for early flame wrinkling might be lower in medium swirl induction case.

Figure 4.20 shows the high swirl induction case of the stratified and homogeneous combustion flame wrinkles behaviors. For the case of stratified combustion in Figure 4.20 (a), the high speeds (1800 rpm and 2100 rpm) flame wrinkling capabilities were reduced from the previous induction strategies; whereas for speed of 1500 rpm case, the value remained unchanged with the change of induction swirl level. On the

other hand, flame wrinkles behavior in high-swirl induction homogeneous combustion process shown in Figure 4.20 (b) demonstrated that the formation of wrinkles were insensitive to engine speed variation in the early time of combustion (up to 1.3 ms after ignition onset). Subsequently, the low engine speeds continued to be dominant in flame surface wrinkling just like the other homogeneous combustion mode of the variable induction cases. Generally, the influence of speed variations on early flame wrinkling were dependant on the mode of combustion. The level of wrinkles increased with engine speeds in the stratified combustion mode. As in the case of homogeneous combustion, it was the opposite; early flame wrinkles level decreased with the rise in engine speed.
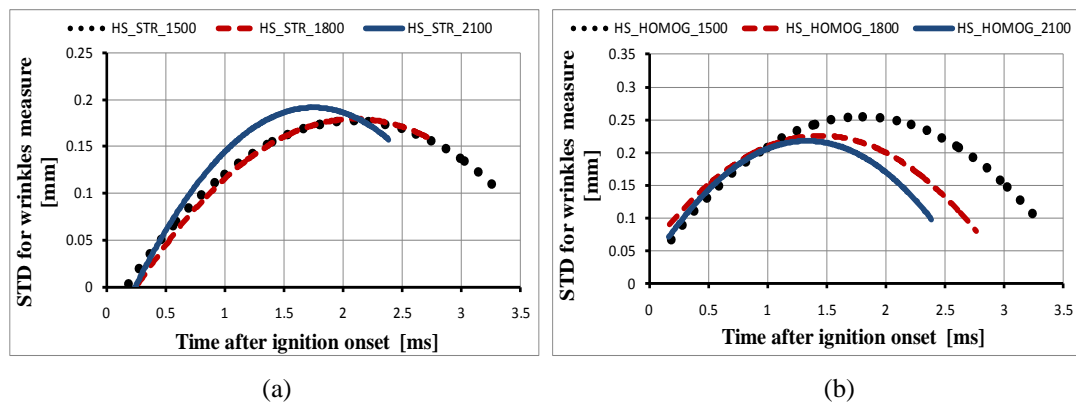

(a)   (b)

Figure 4.20   Flame wrinkles level for high swirl (a) stratified combustion (b) homogeneous combustion

It is also important to see variable swirl level inductions influence wrinkles formation by setting engine speeds. The level of wrinkles measured in STD for both combustion modes at 1500 rpm was plotted in Figure 4.21 for the variable induction cases. As it was discussed earlier, the wrinkles formation at this engine speed was not affected by intake flow properties in the case of stratified combustion, whereas in homogeneous mixture combustion, medium swirl induction showed the lowest ability to wrinkle flame fronts relative to the other induction systems.

In the case of 1800 rpm and 2100 rpm engine speeds, medium tumble inductions favored higher wrinkles formation in stratified combustion and high-swirl induction favored high formation of wrinkles in homogeneous combustion as demonstrated in Figure 4.22 and 4.23. At all engine speeds of homogeneous combustion medium swirl induction had the least capability to wrinkle flame surfaces compared to the other

induction strategies. That means medium swirl induction with large, strong and compact swirling core had a low rate of turbulence decomposition. Flame front wrinkles are highly favored by high turbulence intensity and small scale flows, which are the results of turbulence decomposition (decaying)
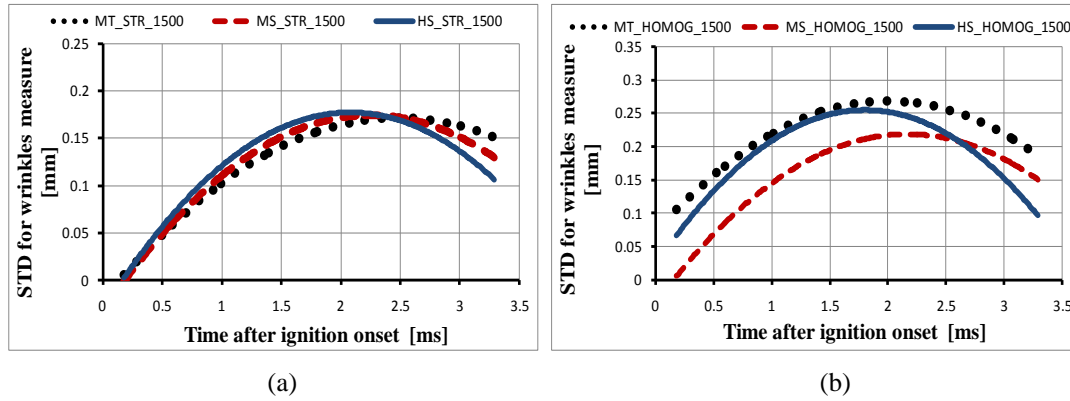

Figure 4.21   Flame Wrinkles level at 1500 rpm for (a) stratified combustion (b) homogeneous combustion
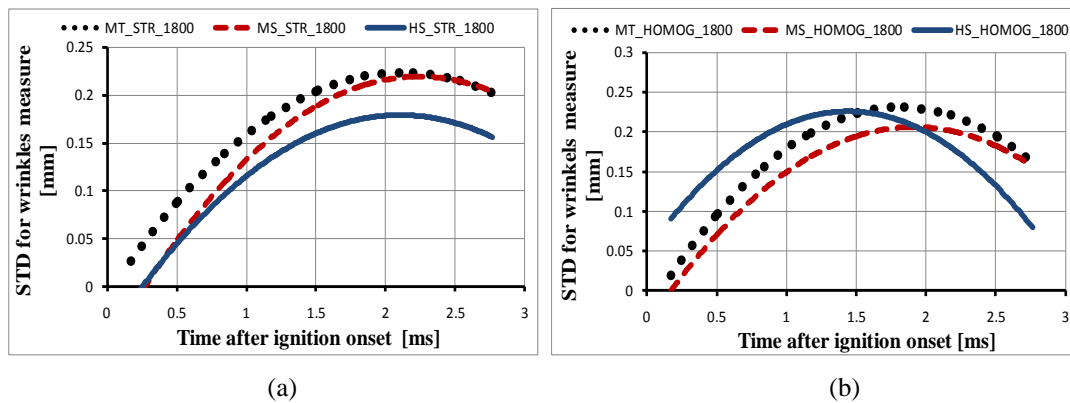

Figure 4.22   Flame Wrinkles level at 1800 rpm for (a) stratified combustion (b) homogeneous combustion
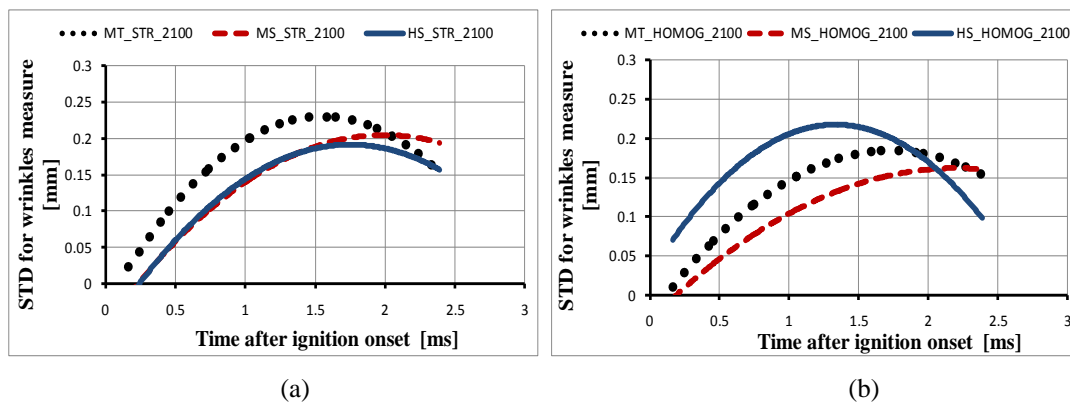

Figure 4.23   Flame wrinkles level at 2100 rpm for (a) stratified combustion (b) homogeneous combustion

The effect of engine speeds and variable intake flow strategies on flame wrinkling capability was analyzed using the standard deviation of measured turbulent contour segment displacements from the mean flame contour. It was generally observed that the effect of change in engine speeds and change in intake flow characteristics on the formation of wrinkles on flame surfaces was dependent on the mode of combustion. Generally, in a stratified combustion mode formation of flame wrinkles were favored by rising the engine speeds and using medium tumble induction strategy, whereas in the case of homogeneous combustion process the rise in engine speed did not favor better wrinkling at all and working at high-swirl induction generally showed a high wrinkles formation possibility. Medium-swirl was the least capable for the formation of flame wrinkles in this homogeneous combustion process.

4.3.3 Flame Distortion

Flame distortion is a measure of global change of the flame structure or shape. Early flame can be distorted due to its interaction with large scale flows, local quenching of the flame surface having contact with cold surfaces such as spark electrodes and or the hydrodynamic strain effects of the in-cylinder bulk flow [73]. In this study, distortion was measured by the ratio of mean flame perimeter to the perimeter of a circle having equivalent radius similar to the works of [5], [23], [74]. Here the mean flame contour perimeter was considered for the calcualtion instead of the turbulent flame in order to avoid the over lapping consideration of local curvature changes due to wrinkling. Wrinkles are the effects of small scale interactions with the flame front, but distortion is large scale effects.

Distortion of the early flame was measured and plotted in Figure 4.24 to 4.26 for various engine speeds. The general observation results showed that by increasing engine speed, flame distortion in all cases of inductions and combustion modes was also increased. Engine speeds affect flame distortion strongly in stratified combustion mode than in the homogeneous one. A higher rate of distortion was obtained within 1.5 ms after ignition timing especially at medium swirl and high swirl cases. It is clear that the mean bulk flow increases with engine speed and so does the distortion.

Medium swirl 1200 rpm (the highest speed) exhibited the highest degree of distortion. Previously, it was also discussed that the large and compact swirl core created in medium swirl induction would have the lowest rate of turbulence decomposition relative to the other cases. Due to this, large scale flows might dominate the flow at ignition timing in the vicinity of spark plug compared to the other induction cases.
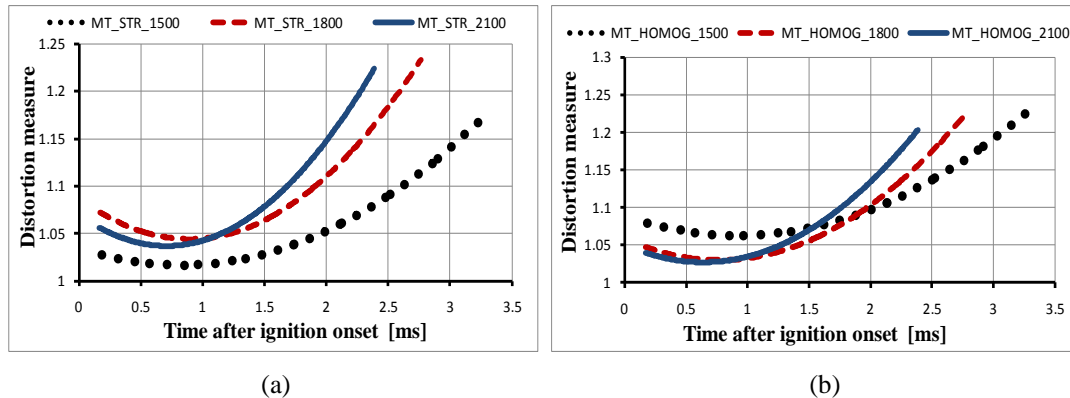

Figure 4.24   Flame distortion for medium tumble induction (a) stratified combustion (b) homogeneous combustion
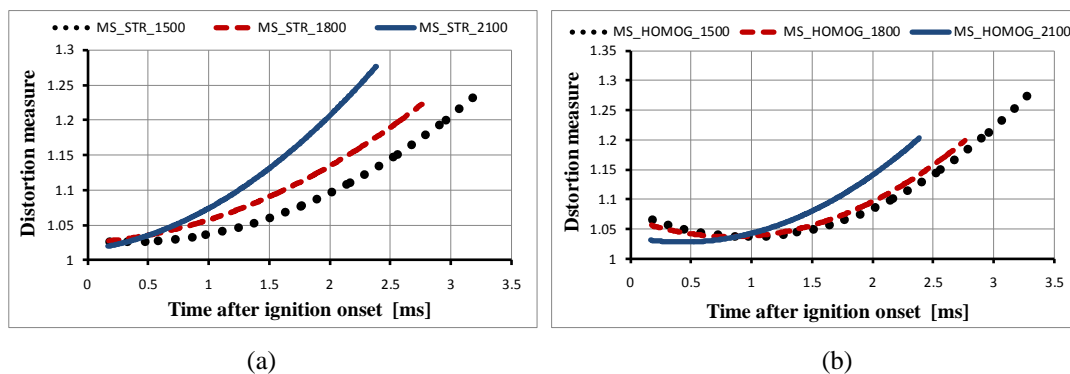

Figure 4.25   Flame distortion for medium swirl induction (a) stratified combustion (b) homogeneous combustion
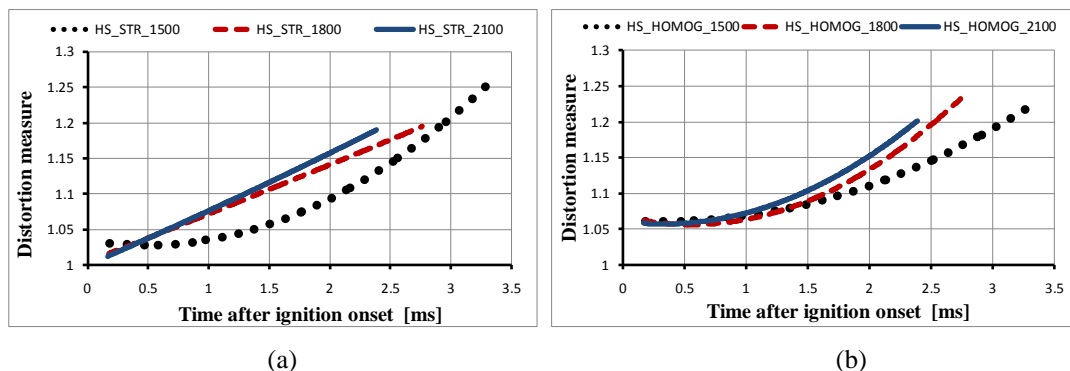

Figure 4.26   Flame distortion for high swirl induction (a) stratified combustion (b) homogeneous combustion

The change of flame distortion on a specific engine speed but variable induction flow characteristics were also analyzed and plotted in Figure 4.27 to 4.29 for both combustion modes. Medium tumble induction exhibited the least flame distortion magnitude than the medium swirl and high swirl induction cases in stratified combustion mode, whereas the medium swirl and high swirl inductions showed nearly the same behavior regarding distortion of the flame. The nature of distortion in homogeneous combustion process showed little variation from the stratified one yet the general trend was the same. In all engine speeds, high-swirl intake flow case favored a higher distortion than the other induction cases in the homogeneous combustion mode with higher speeds (1800 rpm and 2100 rpm). Generally, flame distortion was relatively facilitated by medium swirl and high swirl induction cases almost at equal degree in stratified combustion mode. In the case of homogeneous combustion the effect of high swirl induction on distortion was seen high. It was observed too that medium tumble induction had lower contribution regarding flame distortion when compared to the other inductions. The medium tumble induction macro structure was observed in the previous section that it exhibited a coherent circular flow on the tumble plane and multiple vortices on the swirl plane. It was also discussed that tumble inductions are susceptible for faster turbulence decomposition compared to the swirl inductions. Hence, the small scale flows that could be the results of the decomposition might have low tendency of distorting the flame.
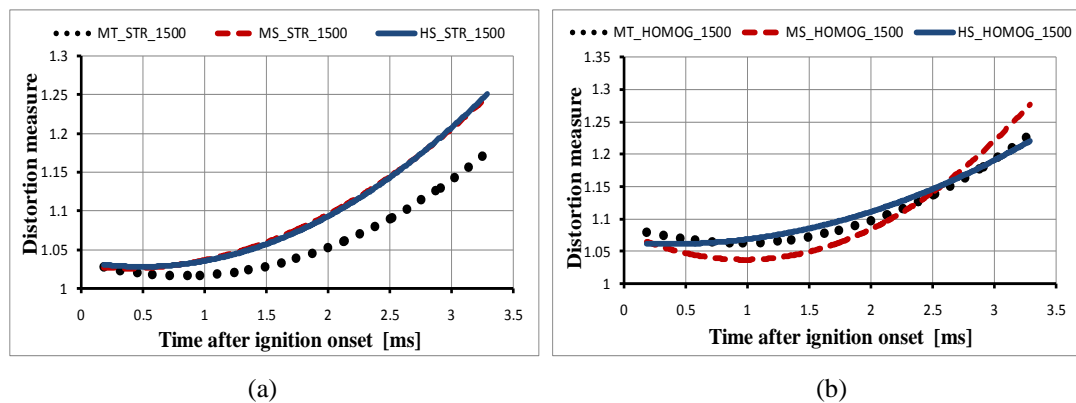

(a)	(b)

Figure 4.27   Flame distortion at 1500 rpm (a) stratified combustion (b) homogeneous combustion
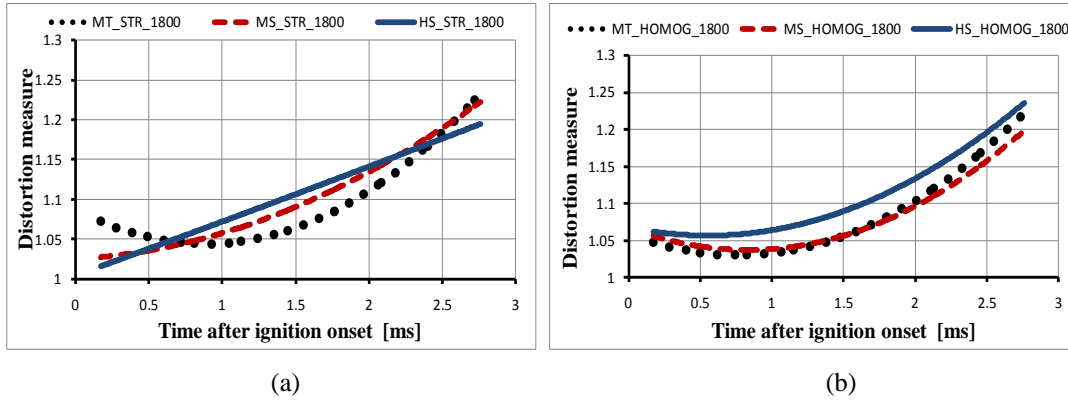
Figure 4.28 Flame distortion at 1800 rpm (a) stratified combustion (b) homogeneous combustion
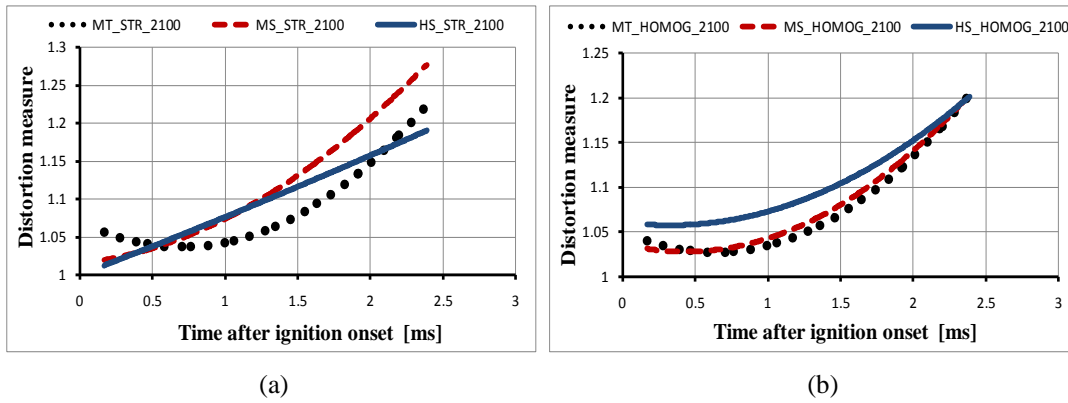

Figure 4.29 Flame distortion at 2100 rpm (a) stratified combustion (b) homogeneous combustion

4.3.4 Flame Position and Displacement

Flame displacement is the distance measured between the spark center and flame center. The spark center was taken to be the center of the gap between the spark electrodes. The ignition kernel can be displaced from the spark center in its earliest stage, as early as the arc phase [17]. The displacement from spark center can be affected by the bulk flow velocity and by the random motion of the large scale turbulent eddies as well. The direction of the displacement can be in the mean bulk flow direction. Squish flow might have its own influence on displacement of the early flame. As it was discussed in [14] and [40], squish can be intensified with increasing swirl level and with elevated mean piston speed. The direction of this squish flow during compression process is generally radial and down word (opposite to piston motion direction). However, since the bowl in the current piston has an offset center (8.4mm) from the cylinder axis, as shown in Figure 4.30, the squish flow direction might be diverted to the direction of the bowl center. This probably be the case when

98

the piston approached TDC the flame centers displaced to the direction of the bowl center, to the right. The displacement of the flame, especially in the early stage of flame development, is helpful to avoid or reduce local or global quenching of the small flame ball by eliminating the chance of contact with the spark electrodes.

The displacement and positions of the flame center in reference to the spark center, which was taken to be the center of the coordinate axes, was plotted against time in Figure 4.31 to 4.36 for stratified and homogeneous combustion modes at varying engine speeds and variable induction cases. The position of flame centers and their displacement from the spark center were observed to be affected by the induction process. In the medium tumble induction case, the first flame images of each engine speed captured at 0.15 ms after ignition onset were found displaced 3 to 5.5 mm from the spark center in both combustion modes as shown in Figure 4.31. The displacement in the stratified combustion case showed a linear displacement curve with time and the flame center came nearer to the spark center when flame size increased. In the case of homogeneous combustion, there was little variation in the displacement of flame center within 1.8 ms after ignition timing as shown in Figure 4.31 (b). The exact position of the flame centers were plotted in Figure 4.34 to 4.36 taking axes centers to be the position of the spark center. The x and y coordinate axis used in these figures was the same axis shown in Figure 4.30. It was observed that early flames of tumble induction were located on the left down position from the spark center for both combustion modes. The displacement of the flame was more of radial. This radial displacement of flame center was up to 3:1 to its axial displacement.
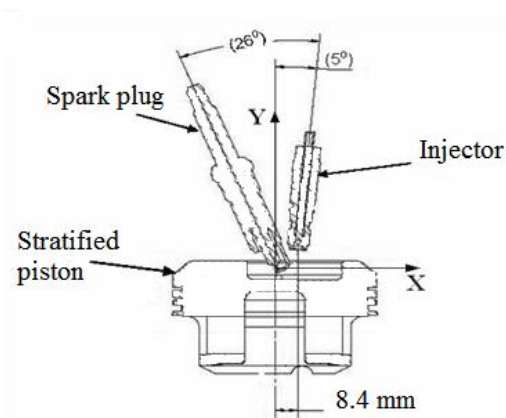

Figure 4.30   Schematics of stratified piston at TDC inside engine cylinder

On the other hand, Figure 4.32 to 4.36 portray that flame center positions and displacements for medium swirl and high swirl intake conditions showed different trend from the previous induction system at both combustion modes for all engine speeds under considerations. The space between electrodes of the spark plug is 1 mm. The very early flame images captured at 0.15 ms after ignition timing for the medium swirl and high swirl induction cases were within 1 mm distance as shown in Figure 4.32 and 4.33. This nearness of the early flames to the electrodes made the flames susceptible to heat losses and quenching (global or local) due to contacts with the relatively colder electrodes. The radial displacement in these inductions was 3 to 4 folds greater than the axial displacement. The other important phenomenon noticed in the medium and high swirl induction cases was that with the flame development time, the flame centers were pushed or displaced towards the right and upward position compared to flame center positions of medium tumble case as shown in Figure 4.34 to 4.36. Generally, the displacement to the right side of the spark center was a function of rise in swirl level at intake process. All flame date captured at medium and high swirl conditions in the homogeneous combustion process had flame centers positioned at the right side of spark center. These flame centers were less scattered than their stratified counterpart. The induction flow structure investigated in earlier sections using PIV system showed the medium and high swirl induction adjustments were capable of forming coherent and strong swirl flows. Zhao et al. [40] mentioned that the swirling flows continue to rotate up to even the end of compression process. The presence of a large bowl-in-piston will have effects on swirl flows during compression process. Heywood [14] discussed about this effect that swirl velocity within the bowl increased as TDC approaching, and outside the bowl it was decreasing. In this study, the bowl axis in the piston has an offset from the cylinder axis as shown in Figure 4.30. This can create an offset swirl flow towards the left portion of the cylinder. This could be the reason for the early flame to be convected to the left portion of the cylinder in medium and high swirl induction cases as depicted in Figure 4.34 to 4.36.
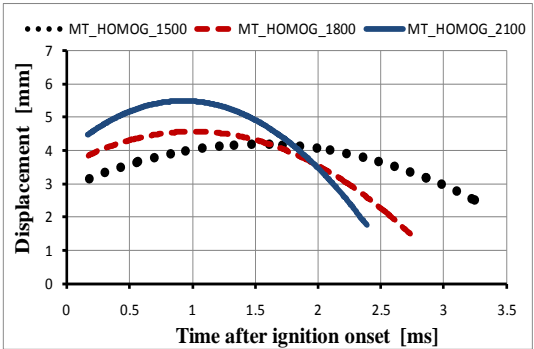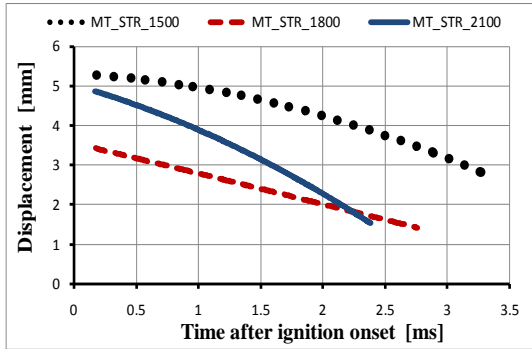
(a)   (b)

Figure 4.31   Flame displacement from spark center at medium tumble induction (a) stratified combustion (b) homogeneous combustion
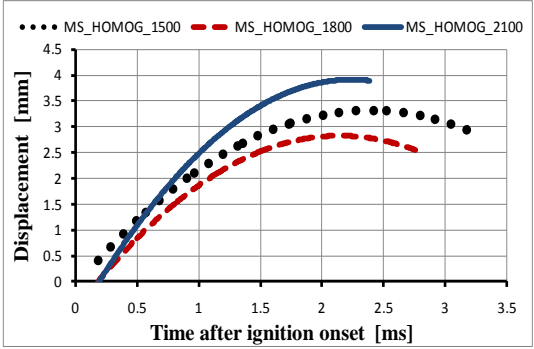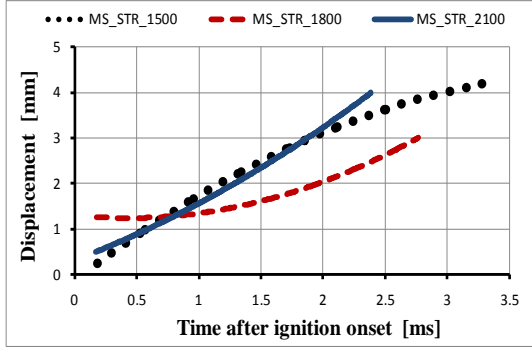
(a)   (b)
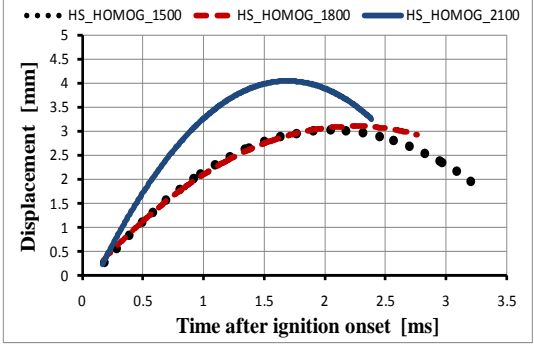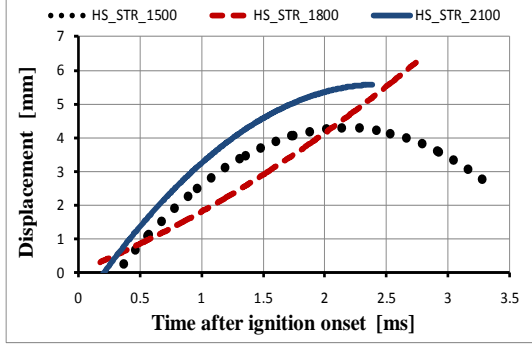
Figure 4.32   Flame displacement from spark center at medium swirl induction (a) stratified combustion (b) homogeneous combustion

(a)   (b)

Figure 4.33   Flame displacement from spark center at high swirl induction (a) stratified combustion (b) homogeneous combustion

Figure 4.34   Flame centroid position relative to spark center at 1500 rpm (a) stratified combustion (b) homogeneous combustion

Figure 4.35   Flame centroid position relative to spark center at 1800 rpm (a) stratified combustion (b) homogeneous combustion

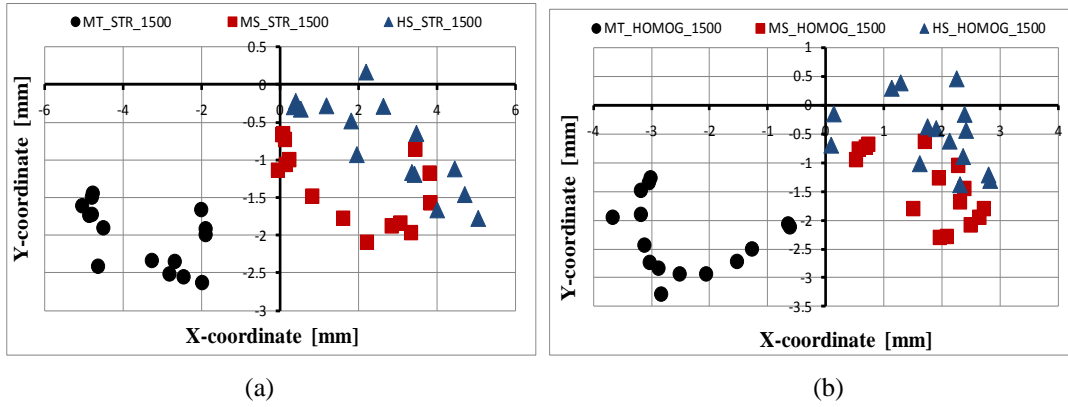*Figure 4.36   Flame centroid position relative to spark center at 2100 rpm (a) stratified combustion (b) homogeneous combustion*
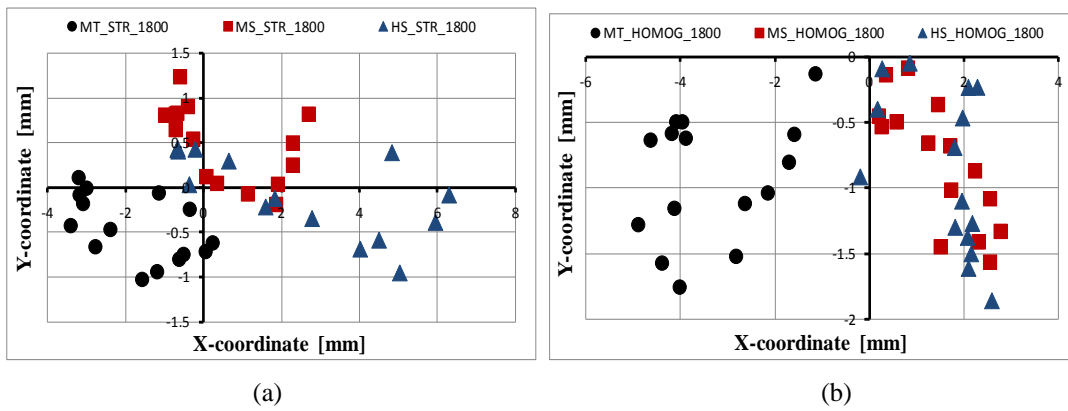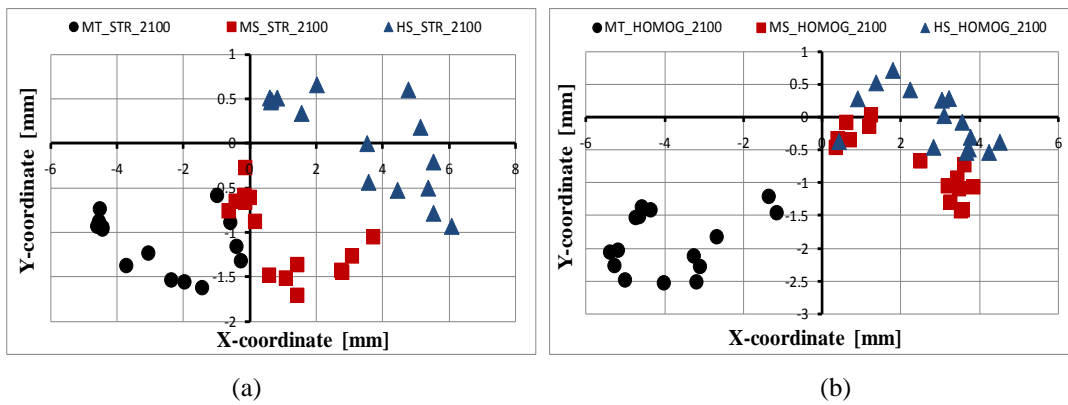
4.3.5   Flame Growth Rate

Flame growth rate or expansion rate measures rate of change of flame size. It is the function of all the flame parameters discussed earlier. Formation of wrinkles on flame

surface increases the reaction surface area of the flame. This, consequently, increases the burning rate and expansion rate. As it was discussed earlier, small scale eddies (eddies smaller than flame size) are responsible for the wrinkles formation on flame surfaces. With the rise in flame size more eddies are becoming smaller than the flame and will add their contribution on the wrinkling process. Hence, the increase in the size of the flame makes the flame interact with the surrounding turbulent flow and result in more wrinkled surface or in other words, the level of wrinkles increases with flame size. Figure 4.37 shows relation of flame wrinkles with flame radius. They have direct relationship and that an increase in flame wrinkles will increase flame radius.
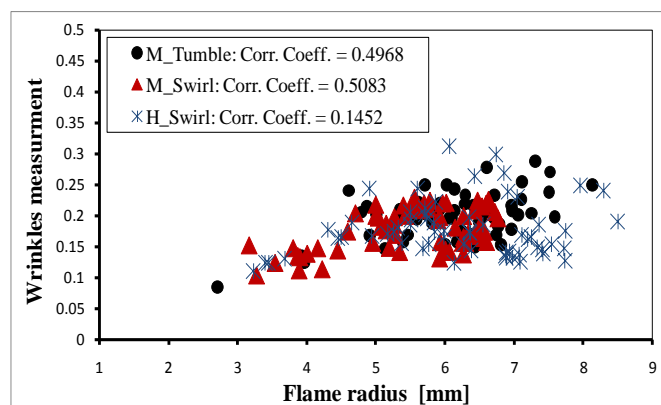
Figure 4.37   Correlations of flame wrinkles and flame size

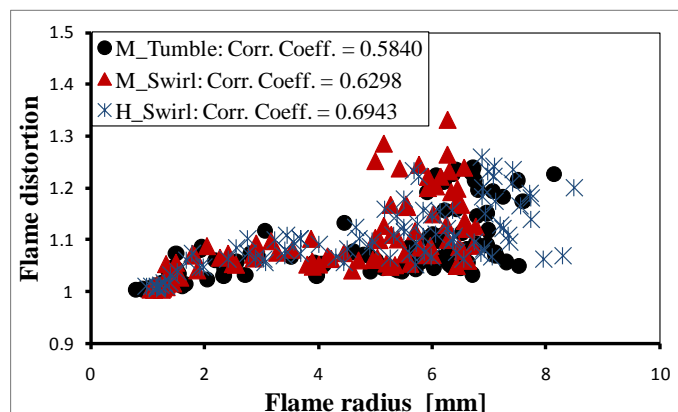*Figure 4.38   Correlations of flame distortion and flame size*

On the other hand, the rate of flame distortion had insignificant contribution for flame expansion in the early development stage. The measured flame distortion at the respected size of the flame for stratified combustion was plotted in Figure 4.38. It was observed that significant distortion was identified when the flame size grew large

enough. In Section 4.3.3, it was also discussed that flame distortion was noticed late in the development period. In the early stage of combustion, distortion was mainly the result of flow effects that could be related to large scale flow interactions with the flame [5]. The contact of flame with a cooler surface, such as spark electrodes, can partially quench the flame and this phenomenon can also create distortion. It can be hypothesized that in the early combustion time when the flame is very small (like in this study within 1 ms after ignition, flame size was around 5 mm) the flame can be convected by wandering large eddies rather than distorted. It can also be concluded from the observation of Figure 4.24 to 4.26 and 4.38 that the effect of distortion on flame growth rate might be noticed in the late development period.

The other parameter that might influence flame expansion rate could be displacement of the flame from the spark center. It was shown in Figure 4.31 to 4.36 that at the start of flame data gathering (0.17 ms after ignition timing) the small flame, which has a radius of about 1.5 mm, was already convected away from its born place (spark center). The flames captured at this point in the medium tumble induction were the farthest of the other two inductions from the spark center. This phenomenon was an advantage to avoid heat losses of such small flame due to contact with the spark plug. This might be the case for the slight advantage of better growth rate in the early development period at medium tumble induction over the other method of inductions in stratified combustion mode, as depicted in Figure 4.39 to 4.41. However, the case with homogeneous combustion was different. It was noticed from Figure 4.40 (b) and 4.41 (b) that high swirl induction had the highest growth rate. Since homogenous combustion of high swirl induction at 1800 rpm and 2100 rpm motor speeds could form better wrinkles on flame surfaces than the other inductions (medium tumble and medium swirl), as shown in Figure 4.22 (b) and 4.23 (b), it affected growth rate better than the medium induction case that had flames with less chance of contacts with the spark electrode in the early stage due to its distance. For all observed cases, it was noticed that flame expansion speed dropped from the maximum valve that was gained by the spark-induced value to minimum and rose again somehow. The minimum drop reported was not less than 2.5 m/s within 1 ms after ignition onset, which agrees with the similar observation of [5].

104
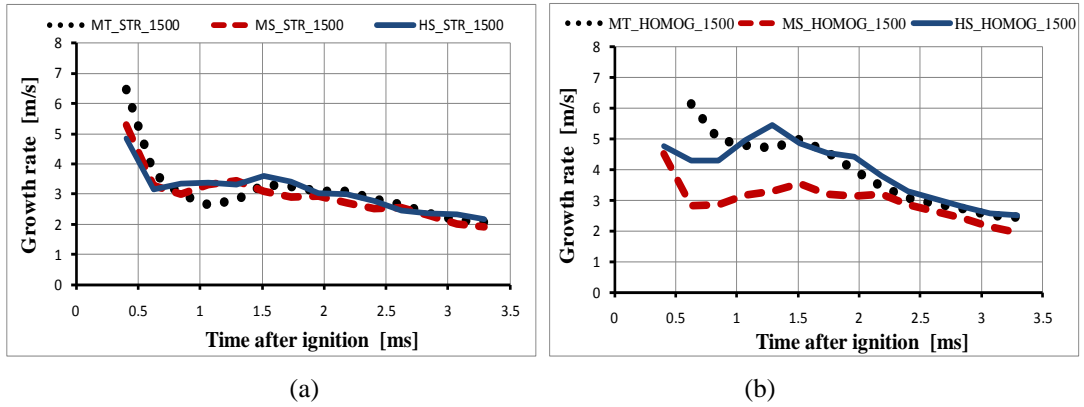
Figure 4.39 Flame growth rate at 1500 rpm (a) stratified combustion (b) homogeneous combustion
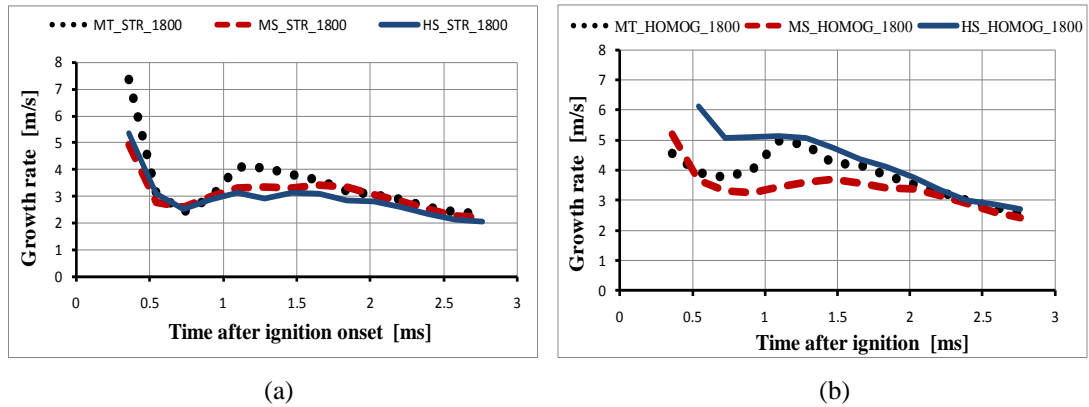
Figure 4.40 Flame growth rate at 1800 rpm (a) stratified combustion (b) homogeneous combustion
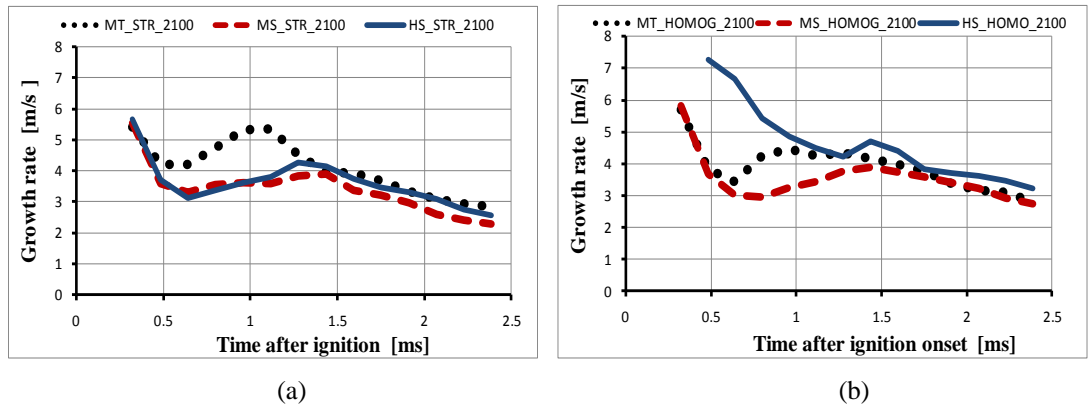
Figure 4.41 Flame growth rate at 2100 rpm (a) stratified combustion (b) homogeneous combustion

From previous analysis, it can be concluded that flame growth rate is highly affected by surface wrinkles. Displacement of early flame from the spark center can also influence growth rate especially in the early period of development. Flame distortion might have influence on growth rate late in the development period. Average flame growth rate within the 3 ms time of combustion was identified for every set parameter and plotted against engine speed in Figure 4.42 for both stratified

and homogeneous combustions. It can be observed from Figure 4.42 (a) that in stratified combustion medium-tumble induction showed a better growth rate than the other induction types especially with the rise in engine speeds. Gunasekaran and Ganesan [75] showed in their CFD study of SI DI combustion that the tumble intake with the late injection provided better mixture formation and combustion characteristics, which supports current findings. Medium and high swirl inductions in the stratified combustion case showed almost similar growth rate characteristics. The Sequence of flame images at the medium tumble induction, stratified combustion for the highest engine speed (2100 RPM) is shown in Figure 4.43.
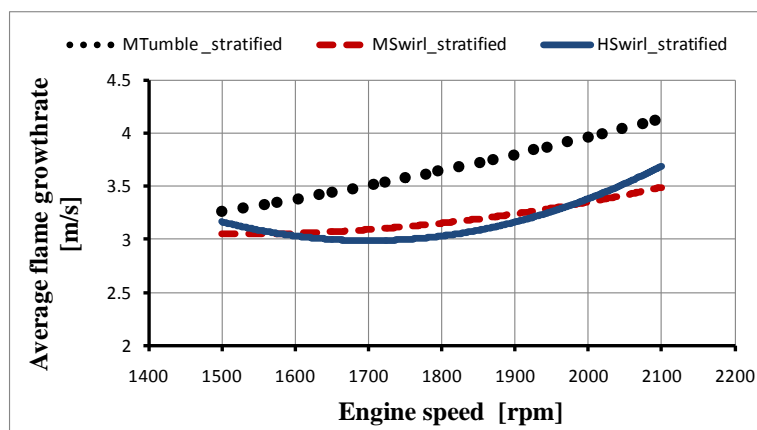
(a) Stratified combustion
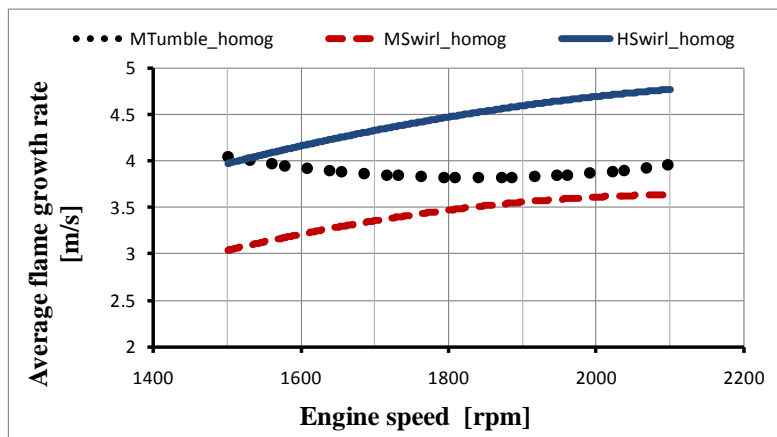
(b) Homogeneous combustion

Figure 4.42   Average flame growth rate for the variable engine parameters

On the other hand, high-swirl induction experienced the highest growth performance and medium-swirl the lowest in homogeneous combustion case as shown in Figure 4.42 (b). It was also observed that high-swirl homogeneous combustion had

the fastest growing flame in the early combustion period and the rate was increasing much more with engine speeds. Average flame growth rate for medium tumble homogeneous combustion showed almost no variation with change in engine speeds. Flame displacement from the spark center might not be correlated with growth rate. However, when the flame had contact with the spark electrodes there could be conductive heat loss. This phenomenon can cause local quenching of the flame, which could reduce flame size and growth rate. The sequence of typical flame images for the high swirl induction, homogeneous combustion at 2100 RPM is portrayed in Figure 4.44.

0.16 ms	0.32 ms	0.48 ms	0.64 ms
0.80 ms	0.96 ms	1.12 ms	1.28 ms
1.43 ms	1.59 ms	1.75 ms	1.91 ms
2.07 ms	2.23 ms	2.39 ms	Scale 5.4 mm
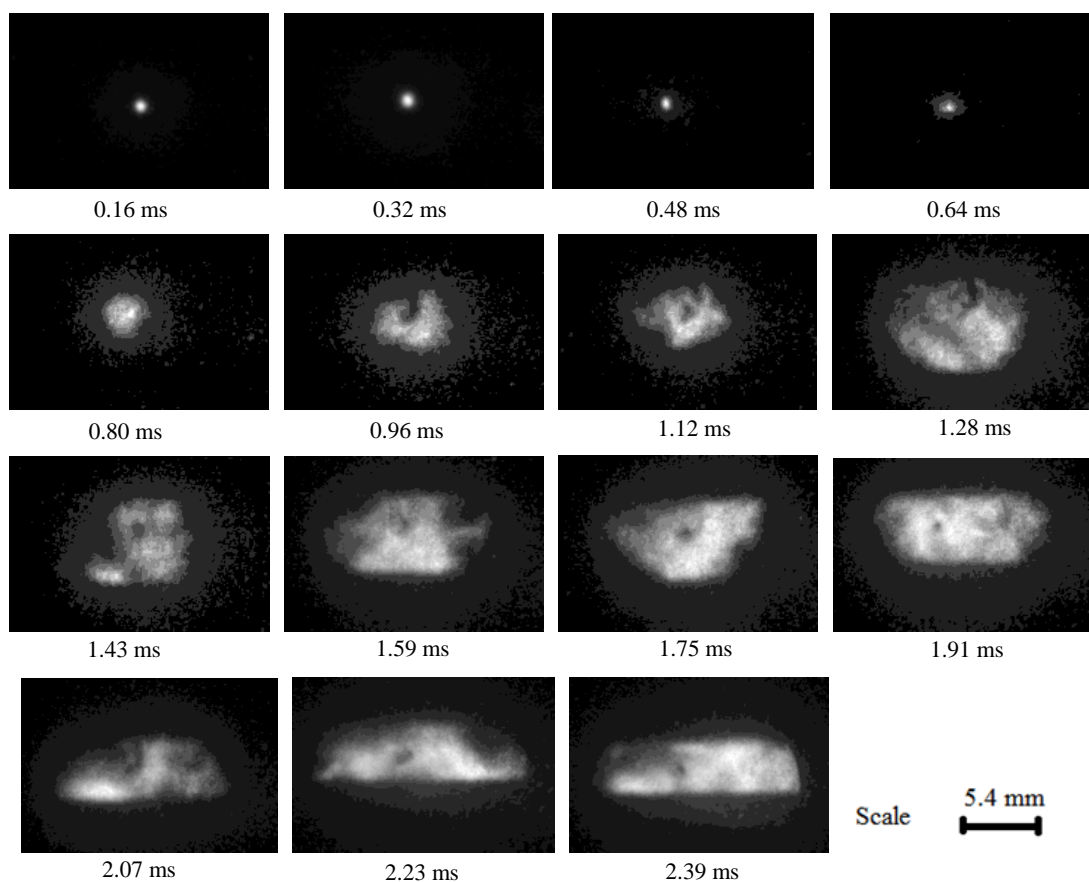
Figure 4.43   Sequences of typical flame images in a medium tumble induction stratified combustion at 2100 RPM engine speed

107
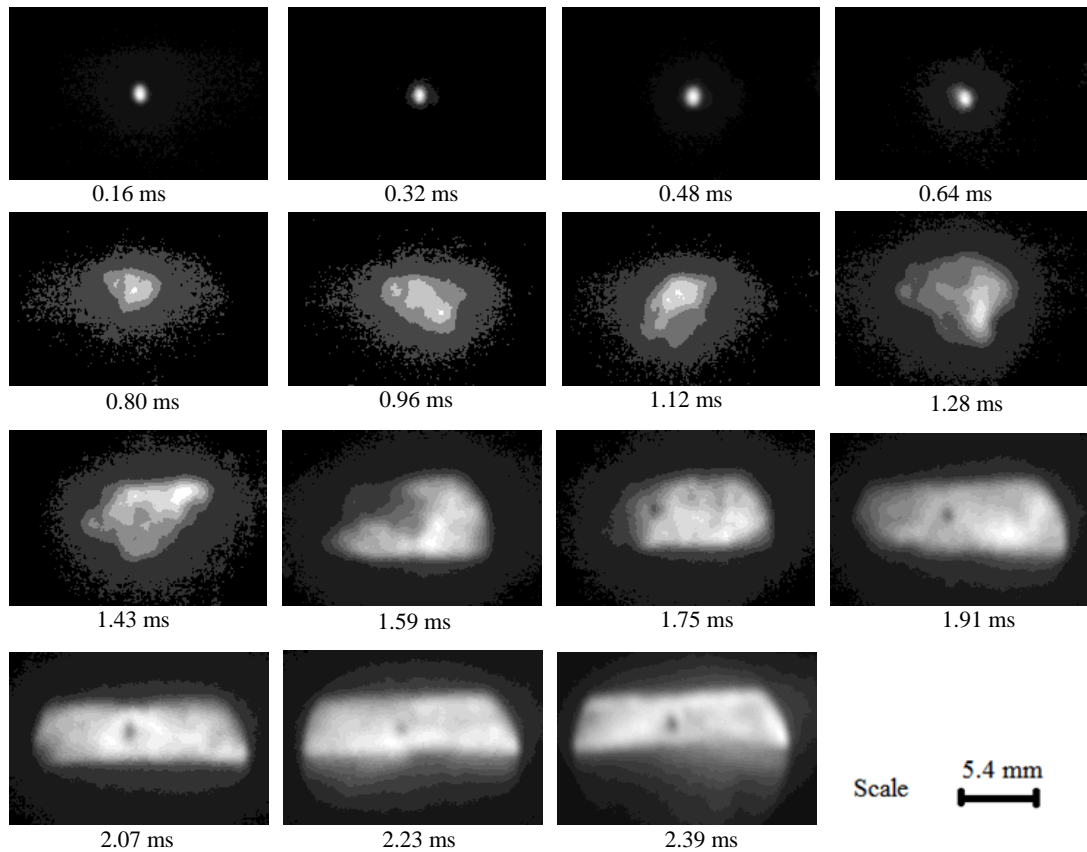
Figure 4.44   Sequences of typical flame images in a high swirl induction homogeneous combustion at 2100 RPM engine speed

4.4 Combustion Performance and its Relationship with Flame Growth Rate

4.4.1 Fuel Burn Fraction

Fuel burn fraction was identified from cylinder pressure data as discussed in Chapter 3. Ignition kernel phases were discussed in Chapter 2 and it was clear that after the end of ignition kernel formation, combustion process controls the flame growth and expansion rate. Fuel burn fraction against time was plotted in Figure 4.45 to 4.47. The effect of induction swirl level was minimal in stratified combustion, but still the medium tumble induction had a slight advantage over the others in early combustion stage. As for homogeneous combustion, high swirl induction had better fuel burn rate. The duration of 0-10% fuel mass burn was compared with growth rate in Figure 4.48. It was observed that an increase in flame growth rate has caused the 0-

10% fuel burn duration to be shorter, and there was a negative 0.631 correlation between them.

(a)   (b)

Figure 4.45   Fuel mass burn fraction at 1500 rpm (a) stratified combustion (b) homogeneous combustion

(a)   (b)

Figure 4.46   Fuel mass burn fraction at 1800 rpm (a) stratified combustion (b) homogeneous combustion

(a)   (b)

Figure 4.47   Fuel mass burn fraction at 2100 rpm (a) stratified combustion (b) homogeneous combustion

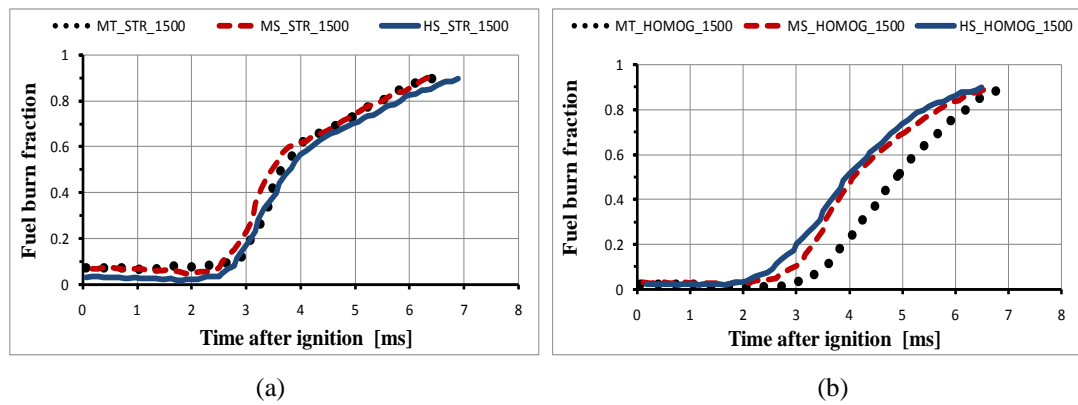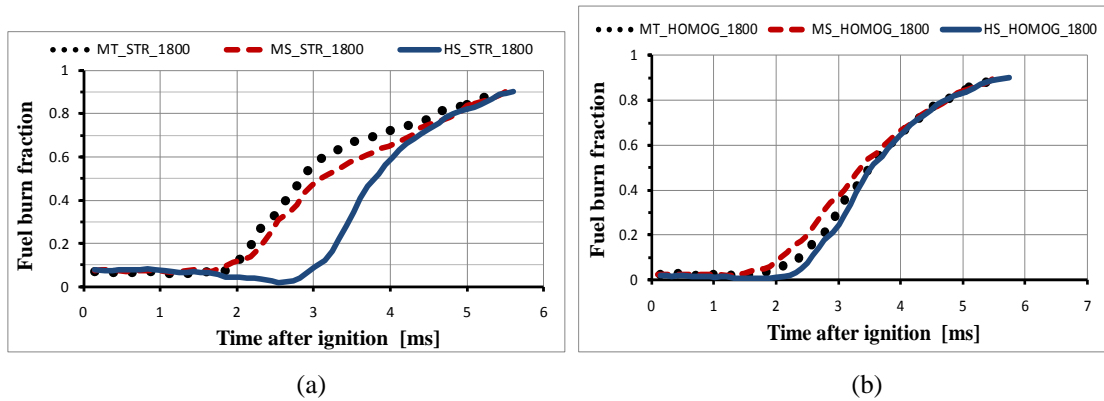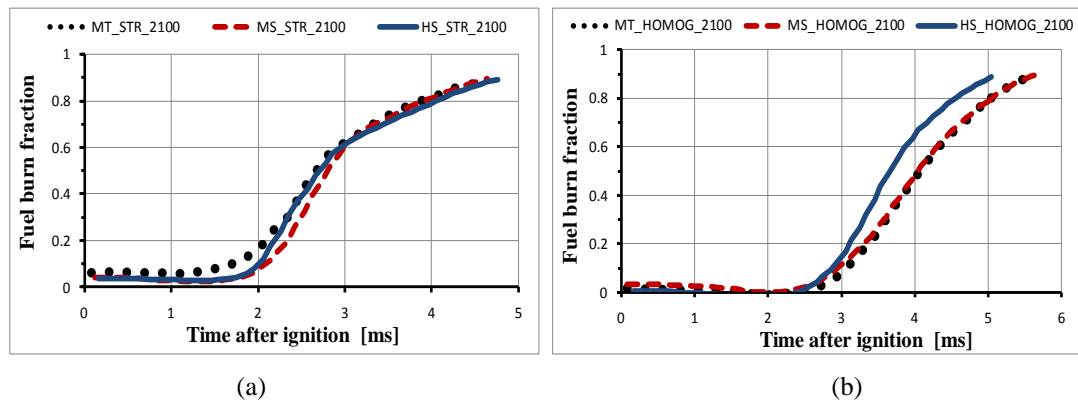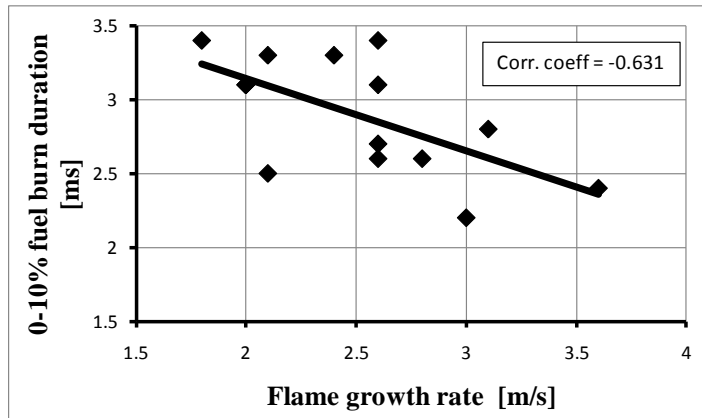*Figure 4.48   Relation between 10% fuel mass burn duration and flame growth rate*

4.4.2 Peak Cylinder Pressure

Variations in ignition timing affect the pressure development in the engine cylinder. If the ignition timing is set early relative to TDC during the compression process the work transfer to the cylinder gases at the end of compression becomes large. This eventually results in a high peak pressure. On the other hand, if ignition is late (near to TDC) the peak pressure developed in the cylinder becomes small. In the current study the ignition timing was set to be 38.5 BTDC (in the range of maximum brake torque). Hence the peak pressure was affected by the rate of combustion especially in the early stages. Figure 4.49 and 4.50 showed relations between average early flame growth rate with peak pressure and its location angle. Peak pressure showed a slight increase with growth rate with a poor positive correlation. Peak pressure angle seemed highly affected by early flame growth rate variations as shown in Figure 4.50. For general consideration, if the peak pressure is too near to TDC or too far from TDC the torque generated will be small. There should be an optimum location for peak pressure to generate high brake torque, because torque has direct relation with peak pressure as shown in Figure 4.51. It was observed from Figure 4.50 that in the case of homogeneous combustion for all cases of inductions, flame growth rate had a positive correlation of 0.52 with the location of peak pressure angle. Thus, with increasing early flame growth pressure angle was delayed beyond TDC up to 10 ATDC for the fastest growing flame at high swirl induction. In the case of stratified combustion early flame growth rate had a negative correlation with peak pressure location relative

110

to TDC. In other words, the higher the growth rate the nearer the peak pressure location to TDC.
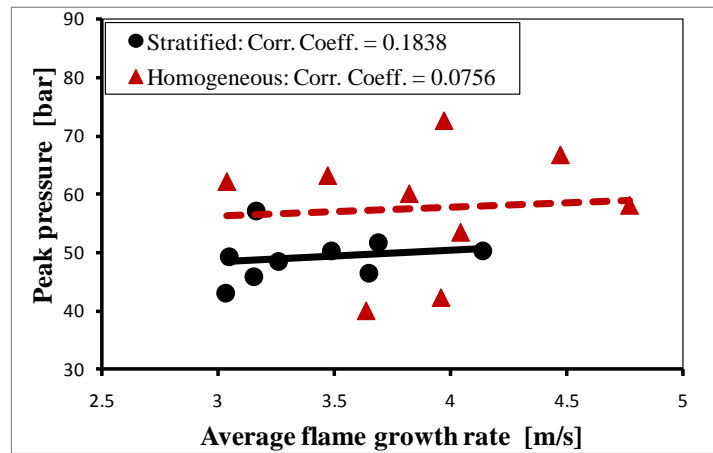
Figure 4.49   Correlation between peak cylinder pressure and average flame growth rate
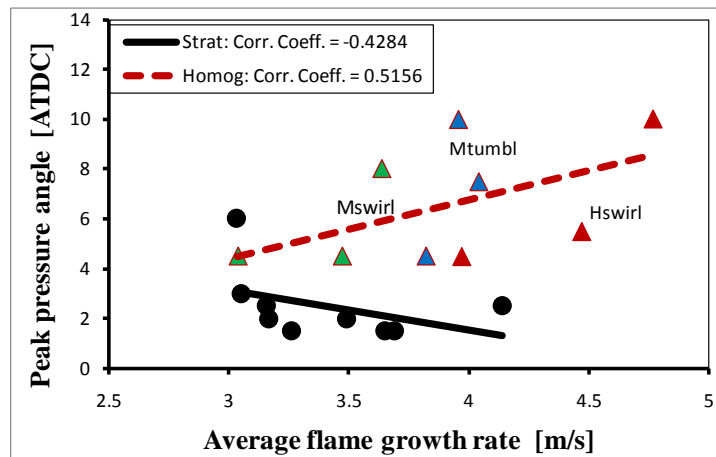
Figure 4.50   Correlations between peak pressure angle and average flame growth rate
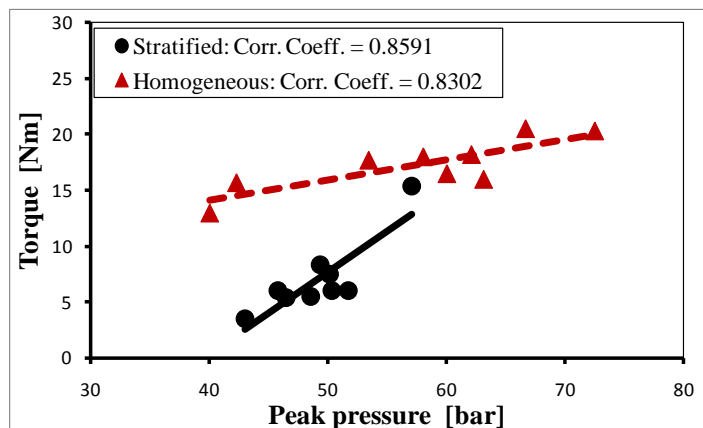
Figure 4.51   Correlation between torque and peak pressure

111
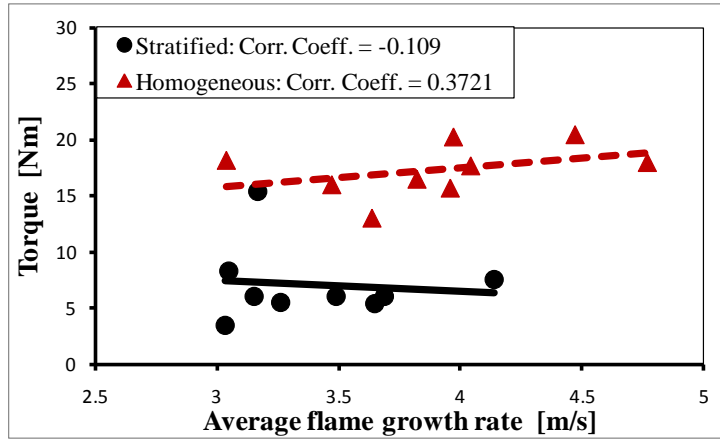
Figure 4.52   Correlation between torque and average flame growth rate

4.4.3 NO$_x$ Formation

Heywood [14] mentioned that the equivalent ratio ϕ and ignition timing are some of the basic engine parameters that can affect NOx emissions. Figure 4.53 to 4.55 show NOx relationships with equivalent ratio, flame growth rate and peak pressure for this study. It was observed that NOx formation can be positively correlated to equivalent ratio (ϕ) with correlation coefficients of 0.81 and 0.92 for stratified and homogeneous combustions, respectively. It was also increasing with the rise in flame growth rate. NOx formation in stratified combustion can be high due to the result of high local temperatures of combustion gases in the early stages. For instance, NOx formation at $\phi = 0.5$ in stratified combustion was greater than the one created at $\phi = 0.7$ in homogeneous combustion as shown in Figure 4.53. Hence, it can be concluded that the formation of NOx in the cylinder had strong positive correlation with equivalent ratio and peak cylinder pressure. And it also had fair positive correlation with flame growth rate.

112
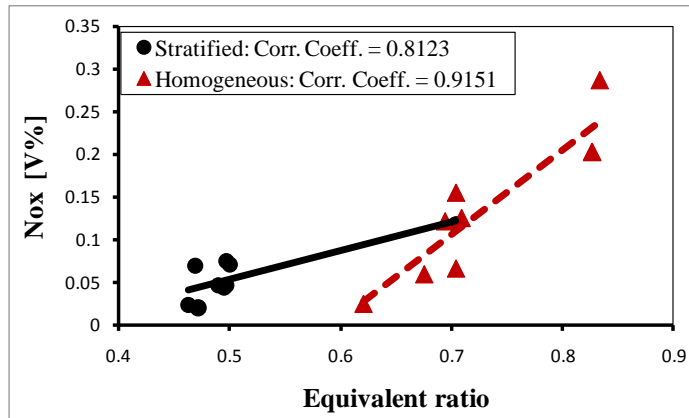
Figure 4.53   Relationship between Nox and equivalent ratio
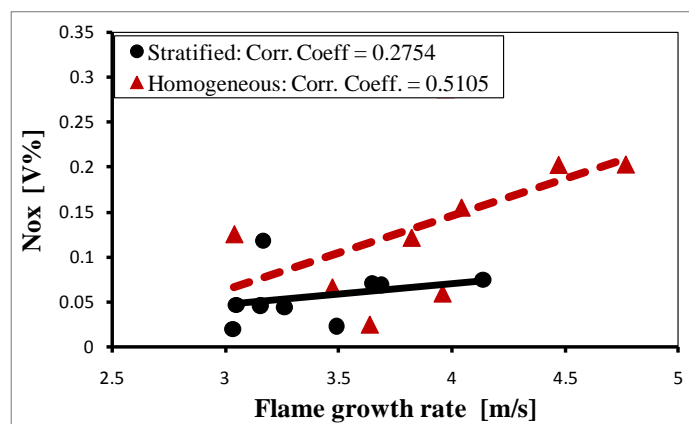
Figure 4.54   Relationship between Nox and flame growth rate
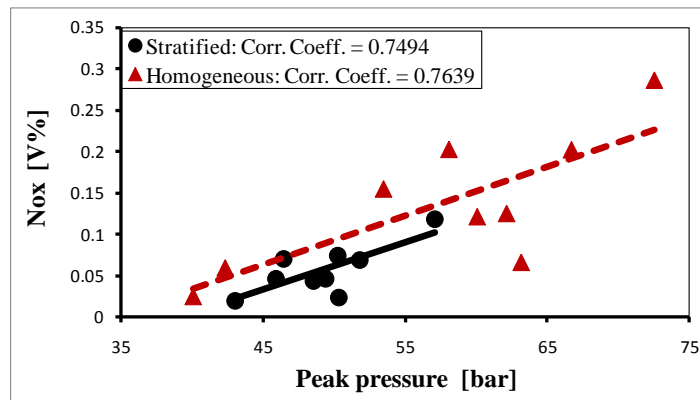
Figure 4.55   Relationship between Nox and peak cylinder pressure

4.5   Summary

Some literature reached to a conclusion that high swirl at induction enhances early flame growth rate in an SI engine [14], [38]. Still others reported that tumble

induction enhances early flame growth rate due to its high turbulence decomposition rate [40]. Yet other researches only associated the high frequency part of the turbulence spectrum with the flame growth rate due to the high wrinkling and shearing effect of the flow when it interacts with the small flame kernel [5], [18], [49]. This study summarizes that early flame kernel growth depends not only on intake swirl properties but also on mixture level of stratification or homogeneity. It was found that in stratified combustion, medium tumble induction had better flame growth rate. On the other hand, in homogeneous combustion high swirl induction demonstrated better flame development rate.

CHAPTER 5

CONCLUSIONS AND FUTURE WORK

5.1   Conclusions

The early flame development characteristics of a CNG direct injection combustion at variable intake swirl flow conditions were investigated for a homogeneous and stratified combustion cases. Flame images were taken by endoscopic intensified CCD camera. Quantitative information was retrieved from the images using elliptic Fourier analysis technique and some basics image analysis procedures such as binarization and contour plotting algorithms. The controlling parameters were SCV adjustment angles, engine speeds and injection timing.

5.1.1   Stratified Combustion Case

Stratified combustion was performed at a fuel injection timing of 90° BTDC. In this combustion mode the flame wrinkles level, which is a function of small scale eddies availability in the flow surrounding the flame, was observed to increase with engine speed. The change in swirl level of induction process did not bring any considerable variations in flame wrinkles at 1500 rpm engine speed. However, for higher speeds (1800 rpm and 2100 rpm) medium tumble showed better wrinkling effect than the other induction techniques.

As for flame distortion, it was found to be directly related to engine speeds. The maximum recorded distortion level in the flame development period was nearly 1.3. The effect of change in swirl induction on flame distortion was not significant. However, medium tumble showed lower distortion rate compared to the other inductions.

Early flame positions relative to the spark center had direct relation to the induction swirl property. The role of piston bowl also seemed to affect the flame position. Therefore, with the high level of swirl induction (medium swirl and high swirl cases) the early flame was displaced into the side of the bowl, which had some offset from the cylinder axis. This flame position and displacement has the advantage of keeping the small flame from having contacts with cold surfaces such as spark electrodes.

The combined effect of the analyzed flame parameters in the stratified combustion resulted in a higher flame expansion rate for medium tumble induction. The medium swirl and high swirl inductions showed almost similar characters on flame growth rate. On the other hand, engine speed rise increased flame expansion rate in all cases of induction. Therefore, when the CNG direct injection engine works in a stratified combustion mode, medium tumble induction at high engine speed delivers a better flame development rate.

5.1.2 Homogeneous Combustion Case

Homogeneous mixture of fuel and air was supposedly formed at an injection timing of 180° BTDC (before the intake valve was closed). The flame wrinkles at the medium tumble induction case was inversely related to engine speeds. The 1500 rpm case showed a better wrinkling effect throughout the development period. Similar general trends were observed in the cases of medium swirl and high swirl inductions. High swirl induction was observed to have a better wrinkling ability of the early flame and medium swirl was the least to form wrinkles on flame surface.

The flame distortion in homogeneous combustion showed similar characteristic to the stratified combustion case. The higher the engine speed the higher the distortion level was. Even though contribution of swirl level variations at induction on flame distortion in homogeneous combustion was small, high swirl induction showed higher tendency than the others.

Regarding flame displacement, the general trend was similar to stratified case.

But, the flame position in medium swirl and high swirl induction cases were more compactly positioned near to the spark center, and totally located on one side of the cylinder portion (where the piston bowl center is located).

The influence of the variable parameters resulted high flame development rate for the high swirl induction case of the homogeneous combustion. This could reach up to 4.8 m/s at 2100 rpm engine speed. The maximum growth rate for the stratified combustion was 4.1 m/s at the same engine speed. Medium tumble induction showed almost no change of growth rate with engine speed, and it was about 4 m/s. Medium swirl case was the lowest development rate. Hence, in homogeneous combustion case, high swirl induction at high engine speed could have the highest flame development rate.

5.1.3 Performance Parameters

Cylinder peak pressure showed weak positive correlation with flame growth rate, whereas peak pressure angle had a positive good correlation with flame growth rate in homogeneous combustion and a negative correlation in stratified combustion. The generated torque showed a slight positive correlation in homogeneous and negative correlation in stratified with flame growth rate. Formation of NO_x was smaller in stratified combustion, and yet increased with flame growth rate in both combustion cases.

5.2 Future Work

Although important characters of early flames for CNG DI combustion were examined in this study, there are still opportunity for further investigation. The study can be extended by providing simultaneous multiple plane visualization of the flame so that its expansion in different direction can be considered.

In regard to in-cylinder flow, turbulence decomposition and its turbulent kinetic energy budget during intake and compression process need to be detailed to characterize the different induction strategies. Quantification of the turbulence level

around spark electrodes near ignition timing is important to study the details of early flame behaviors. For instance, in this study some basic flame kernel parameters (such as flame growth rate and wrinkles level) were found to be different in homogeneous and stratified combustion cases at a similar engine speed and induction swirl levels. Medium tumble had better growth rate in stratified, whereas high swirl induction was best in homogeneous. Obviously, the variation came from the late fuel injection in the stratified case that resulted a higher flame growth rate for a medium tumble induction. This would be a gap to study how the late fuel injection changes the turbulence quantities of a tumble and a swirl induction near to ignition timing. However, to accomplish the recommended works on the current engine setup it needs modifications, such as improving optical accessibility on both tumble and swirl planes.

REFERENCES

[1]   Y. Daisho, T. Yaeo, T. Koseki, T. Saito, R. Kihara, and E. N. Quirs, "Combustion and Exhaust Emissions in a Direct-injection Diesel Engine Dual-Fueled with Natural Gas," SAE Paper, 1995.

[2]   V. Pirouzpanah and B. O. Kashani, "Prediction of Major Pollutants Emission in Direct - Injection Dual - Fuel Diesel and Natural Gas Engines," SAE Paper, 1999.

[3]   S. Rousseau, B. Lemoult, and M. Tazerout, "Combustion characterization of natural gas in a lean burn spark-ignition engine," Journal of Automobile Engineering, vol. 213, pp. 481-489, 1999.

[4]   L. Ben, N. Raud-Ducros, R. Truquet, and G. Charnay, "Influence of Air/Fuel Ratio on Cyclic Variation and Exhaust Emission in Natural Gas SI Engine," SAE Paper, 1999.

[5]   P. G. Aleiferis, A. M. K. P. Taylor, K. Ishii, and Y. Urata, "The nature of early flame development in a lean-burn stratified-charge spark-ignition engine," Combustion and Flame, vol. 136, pp. 283–302, 2004.

[6]   P. G. Aleiferis, A. M. K. P. Taylor, and J. H. Whitelaw, "Cyclic Variations of Initial Flame Kernel Growth in a Honda VTEC-E Lean-Burn Spark-Ignition Engine," SAE, 2000.

[7]   Y. Xiong, W. L. Roberts, M. C. Drake, and T. D. Fansler, "Investigation of Pre-mixed Flame-Kernel/Vortex Interactions via High-Speed Imaging," Combustion and Flame, vol. 126, pp. 1827–1844, 2001.

[8]   D. A. Eichenberger and W. L. Roberts, "Effect of Unsteady Stretch on Spark-Ignited Flame Kernel Survival," Combustion and Flame, vol. 118, pp. 469–478, 1999.

[9]   P. E. Lestrel, "Method For Analyzing Complex Two-Dimensional Forms: Elliptical Fourier Functions," American Journal of Human Biology, vol. 1, pp. 149-164, 1989.

[10]   S. Shiga, S. Ozone, H. T. C. Machacon, T. Karasawa, and H. Nakamura, "A study of the combustion and emission characteristics of compressed-natural-fas direct injection stratified combustion using a rapid-compression-machine " Combustion and Flame, vol. 129, pp. 1-10, 2002.

[11] Z. Huang, S. Shiga, T. Ueda, H. Nakamura, T. Ishima, T. Obokata, M. Tsue, and M. Kono, "Basic characteristics of direct injection combustion fuelled with compressed natural gas and gasoline using a rapid compression machine," Journal of Automobile Engineering, vol. 217, pp. 1031-1038, 2003.

[12] Z. Huang, S. Shiga, T. Ueda, H. Nakamura, T. Ishima, T. Obokata, M. Tsue, and M. Kono, "Combustion characteristics of natural-gas direct-injection combustion under various fuel injection timings," Journal of Automobile Engineering, vol. 217, pp. 393-401, 2003.

[13] M. I. Jahirul, H. H. Masjuki, R. Sadur, M. A. Kalam, M. H. Jayed, and M. A. Wazed, "Comparative engine performance and emission analysis of CNG and gasoline in a retrotitted car engine," Applied Thermal Engineering, vol. 30, pp. 2219-2226, 2010.

[14] J. B. Heywood, Internal combustion engine fundamentals. New York: McGraw-Hill, 1988.

[15] D. Dunn-Rankin, Lean combustion technology and control. London: Elsevier Inc., 2008.

[16] S. Y. Liao, D. M. Jiang, and Q. Cheng, "Determination of laminar burning velocities for natural gas," Fuel, vol. 83, pp. 1247-1250, 2004.

[17] C. Arcoumanis and T. Kamimoto, Flow and combustion in reciprocating engines. Berlin: Springer, 2009.

[18] H. Willems and R. Sierens, "Modeling the initial growth of the plasma and flame kernel in S.I. engines," Journal of Engineering for Gas Turbines and power, vol. 125, pp. 479-484, 2003.

[19] H. Kolera-Gokula and T. Echekki, "Direct numerical simulation of premixed flame kernel–vortex interactions in hydrogen–air mixtures," Combustion and Flame, vol. 146, pp. 155-167, 2006.

[20] P. O. Witze, M. J. Hall, and J. S. Wallace, "Fiber-Optic Instrumented Spark Plug for Measuring Early Flame Development in Spark Ignition Engines," SAE, 1988.

[21] R. Meyer, J. T. Kubesh, S. M. Shahed, and J. K. Davis, "Simultaneous Application of Optical Spark Plug Probe and Head Gasket Ionization Probe to a Production Engine," SAE, 1993.

[22]   P. C. Hinze and W. K. Cheng, "Flame kernel development in a methanol fueled engine," SAE Paper, 1993.

[23]   R. Ancimer, H. Jaaskelainen, and J. Wallace, "Experiments into the Flame Kernel Development in High Swirl Production Spark Ignition Engine," SAE, 1999.

[24]   H. Zhao and N. Ladammatos, Engine combustion instrumentation and diagnostics. Warrendale: Society of Automotive Engineers, Inc., 2001.

[25]   A. R. Kerstein and P. O. Witze, "Flame-Kernel Model for Analysis of Fiber-Optic Instrumented Spark Plug Data," SAE, 1990.

[26]   D. L. Lord, R. W. Anderson, D. D. Brehob, and Y. Kim, "The Effects of Charge Motion on Early Flame Kernel Development," SAE, 1993.

[27]   Y. Ikeda, T. Nakajima, and T. Ohira, "Flame propagation characteristics by planar OH Measurment," SAE Paper, 1999.

[28]   Y. Ikeda, H. Nishihara, and T. Nakajima, Detailed Spectrum Analysis of Chemiluminescent Radicals at Flame Front in an SI Engine. Nagoya: COMODIA, 2001.

[29]   C. M. Fajardo, J. D. Smith, and V. Sick, "PIV, high-speed PLIF and chemiluminescence imaging for near-spark-plug investigations in IC engines," Journal of Physics vol. 45, pp. 19–26, 2006.

[30]   P. G. Felton, J. Mantzaras, D. S. Bomse, and R. L. Woodin, "Initial two-dimensional laser induced fluorescence measurements of OH radicals in an internal combustion engine," SAE Paper, 1988.

[31]   S. H. R. Muller, B. Bohm, M. Gleibner, and S. Arndt, "Analysis of the temporal flame kernel development in an optically accessible IC engine using high-speed OH-PLIF," Applied Physics B, vol. 100, pp. 447–452, 2010.

[32]   B. Bohm, D. Geyer, A. Dreizler, K. K. Venkatesan, N. M. Laurendeau, and M. W. Renfro, "Simultaneous PIV/PTV/OH PLIF imagimg: conditional flow field statistics in partially premixed turbulent opposed jet flames," Proceedings of the combustion institute, vol. 31, pp. 709-717, 2007.

[33]   N. Pasquier, B. Lecordier, M. Trinite, and A. Cessou, "An experimental investigation of flame propagation through a turbulent stratified mixture," Proc. of the Combustion Institute vol. 31, pp. 1567–1574, 2007.

[34]   T. E. Carlsson, R. Mattsson, P. Gren, M. Elfsberg, and J. Tegner, "Combination of schlieren and pulsed TV holography in the study of a high-speed flame jet," Optics and Lasers in Engineering, vol. 44, pp. 535-554, 2006.

[35]   J. Wang, Z. Huang, C. Tang, and J. Zheng, "Effect of hydrogen addition on early flame growth of lean burn natural gas–air mixtures," International Journal of Hydrogen Energy, vol. 35, pp. 7246-7252, 2010.

[36]   H. Miao, M. Ji, Q. Jiao, Q. Huang, and Z. Huang, "Laminar burning velocity and Markstein length of nitrogen diluted natural gas/hydrogen/air mixtures at normal, reduced and elevated pressures," International Journal of Hydrogen Energy, vol. 34, pp. 3145-3155, 2009.

[37]   M. Raffel, C. E. Willert, S. T.Wereley, and J. Kompenhans, Particle Image Velocimetry a Practical Guid. Berlin: Springer, 2007.

[38]   K. Lee, C. Bae, and K. Kang, "The effects of tumble and swirl flows on flame propagation in a four-valve S.I. engine," Applied Thermal Engineering vol. 27, pp. 2122–2130, 2007.

[39]   S. H. Joo, K. M. Chun, Y. Shin, and K. C. Lee, "An investigation of flame expansion speed with a strong swirl motion using high-speed visualization," Journal of Engineering for Gas Turbines and Power, vol. 125, pp. 485-493, 2003.

[40]   F. Zhao, D. L. Harrington, and M.-C. Lai, Automotive Gasoline Direct-Injection Engines. USA: Society of Automotive Engineers, 2002.

[41]   C. O. Funk, "An In-depth Comparison of Experimental and computational turbulence parameters for in-cylinder engine flows," PhD, Mechanical Engineering, University of Michigan, 2005.

[42]   S. B. Pope, Turbulent Flows. Cambridge: Cambridge University Press, 2000.

[43]   C. Arcoumanis and S. Tanabe, "Swirl generation by helical ports," SAE Paper, 1989.

[44]   Y. S. Cho, D. A. Santavicca, and R. M. Sonntag, "The Effect of Spark Power on Spark Ignited Flame Kernel Growth," SAE, 1992.

[45]   J. B. Heywood, "Combustion and its Modeling In Spark-Ignition Engines," in The 3rd Inter. Sym. on Diag. & Mod. of Comb. in IC Engines, Yokohama, Japan, 1994.

[46] M. Grill, T. Billinger, and M. Bargende, "Quasi-Dimensional Modeling of Spark Ignition Engine Combustion with Variable Valve Train," SAE, 2006.

[47] S. Hosseini, R. Abdolah, and A. Khani, "A Developed Quasi-Dimensional Combustion Model in Spark-Ignition Engines," in Proceedings of the World Congress on Engineering, London, 2008.

[48] J. Song, Y. Seo, and M. Sunwoo, "Effects of Ignition Energy and System on Combustion Characteristics in a Constant Volume Combustion Chamber," SAE Paper, 2000.

[49] D. Ting, M. Checkel, and B. Johansson, "The importance of high frequency, small eddy turbulence in spark ignited, premixed engine combustion," SAE, 1995.

[50] Y. Xiong and W. L. Roberts, "Observations on the interaction between a premixed flame kernel and a vortex of different equivalence ratio," Proc. of the Combustion Institute, vol. 29, pp. 1687-1693, 2002.

[51] S. K. Marley, S. J. Danby, W. L. Roberts, M. C. Drake, and T. D. Fansler, "Quantification of transient stretch effects on kernel–vortex interactions in premixed methane–air flames," Combustion and Flame, vol. 154, pp. 296-309, 2008.

[52] H. H. Geok, T. I. Mohamad, S. Abdullah, Y. Ali, A. Shamsudeen, and E. Adril, "Experimental investigation of performance and emission of a sequential port injection natural gas engine," European Journal of Scientific Research, vol. 30, pp. 204-214, 2009.

[53] L. Gui, W. Merzkirch, and R. Fei, "A digital mask technique for reducing the bias error of the correlation-based PIV interrogation algorithm," Experiments in Fluids, vol. 29, pp. 30-35, 2000.

[54] R. J. Adrian, K. T. Christensen, and Z. C. Liu, "Analysis and interpretation of instantaneous turbulent velocity fields," Experiments in Fluids, vol. 29, pp. 275-290, 2000.

[55] N. Hutchins, W. T. Hambleton, and I. Marusic, "Inclined cross-stream stereo particle image velocimetry measurments in turbulent boundary layers," Journal of Fluid Mechanics, vol. 541, pp. 21-54, 2005.

[56]   M. Sezgin and B. Sankur, "Survey over image thresholding techniques and quantitative performance evaluation," Journal od Electronic Imaging, vol. 13, pp. 146-165, 2004.

[57]   N. Otsu, "A threshold selection method from Gray level Histogram," IEEE transactions, vol. 9, pp. 62-65 1979.

[58]   N. Nacereddin, L. Hamami, M. Tridi, and N. Oucief, "Non-parametric Histogram-based thresholding methods for weld defect detection in radiography," Worl Academy of Science, Engineering and Technology, vol. 9, 2005.

[59]   J. C. Neto, "A combined statistical-soft computing approach for classification and mapping weed species in minimum-tillage system," PhD, University of Nebraska, Lincoln, 2004.

[60]   H. Freeman, "On the encoding of arbitrary geometric configurations," IRE Transactions on Electronic Computers, pp. 260-260, 1961.

[61]   F. P. Kuhl and C. R. Giardina, "Elliptic Fourier features of a closed contour," Computer Graphics and Image Processing, vol. 18, pp. 236-258, 1982.

[62]   J. C. Neto, G. E. Meyer, D. D. Jones, and A. K. Samal, "Plant species identification using elliptic Fourier leaf shape analysis," Computers and electronics in agriculture, vol. 50, pp. 121-134, 2006.

[63]   A. Tort, "Elliptic Fourier functions as a morphological descriptor of the genus Stenosarina (Brachiopoda, Terebratulida, New Caledonia," International Association for Mathematical Geology, vol. 35, pp. 873-885, 2003.

[64]   J. M. Le Minor and M. Schmittbuhl, "Importance of elliptic Fourier methods for morphometry of complex outlines: application to the distal human femur," Surgical and Radiologic Anatomy, vol. 21, pp. 387-391, 1999.

[65]   M. S. Nixon and A. S. Aguado, Feature extraction and image processing, 2nd ed. Oxford: Academic Press, 2008.

[66]   O. D. Trier, A. K. Jain, and T. Taxt, "Feature extraction methods for character recognition- a survey," Pattern Recognition, vol. 29, pp. 641-662, 1996.

[67]   M. F. J. Brunt, H. Rai, and A. L. Emtage, "The calculation of heat release energy from engine cylinder pressure data," SAE Paper, 1998.

[68]   M. Achuth and P. S. Mehta, "Predictions of tumble and turbulence in four-valve pentroof spark ignition engines," International Journal of Engine Research, vol. 2, pp. 209-227, 2001.

[69]   B.-G. Paik, J. Kim, Y.-H. Park, and K.-S. kim, "Investigation of the vortex structure of propeller wake influenced by loading on the blase," Journal of Marine science Technology, vol. 12, pp. 72-82, 2007.

[70]   C. Crnojevic, F. Decool, and P. Florent, "Swirl measurments in a motor cylinder," Experiments in Fluids, vol. 26, pp. 542-548, 1999.

[71]   C. Arcoumanis, Z. Hu, C. Vafidis, and J. H. Whitelaw, "Tumbling Motion: A Mechanism for Turbulence Enhancement in Spark-Ignition Engines," SAE Paper, 1990.

[72]   D. Heim and J. Ghandhi, "A detailed study of in-cylinder flow and turbulence using PIV," SAE Paper, 2011.

[73]   J. M. Samaniego and T. Mantel, "Fundamental Mechanisms in Premixed Turbulent Flame Propagation via Flame–Vortex Interactions," Combustion and Flame vol. 118, pp. 537–556 1999.

[74]   L. Gillespie, "Imaging and analysis of turbulent flame development in spark ignition engines," PhD, University of Leeds, Leeds, 1998.

[75]   J. Gunasekaran and V. Ganesan, "Effect Of Swirl and Tumble on the Stratified Combustion of a DISI Engine - A CFD Study," SAE Paper, 2011.

List of Publications

1. Yohannes T. Anbese, A. Rashid A. Aziz and Zainal Ambri B.A. Karim. "*Flame development characteristics at variable swirl level inductions in a stratified CNG direct injection combustion engine*" Journal of Energy & Power Engineering, Vol. 3, No. 12, pp. 1-9

2. Yohannes T. Anbese, A. Rashid A. Aziz and Zainal Ambri B.A. Karim. **"*Flame Development Study at Variable Swirl Level Flows in a Stratified CNG DI Combustion Engine using Image Processing Technique*"** Journal of Applied Science, Vol. 11, No. 10, pp. 1698-1706

Conference Presentations

1. Presenter- a conference of world engineering, science and technology congress, ESTCON 2010, 15-17 June 2010, Kuala Lumpur Convention Centre, Malaysia

2. Presenter - National Postgraduate Conference on Engineering, Science and technology (NPC 2009), 25-26 March 2009, Universiti Teknologi PETRONAS, Malaysia

3. Presenter- 3rd Seminar in Advanced engine and Fuel Technology 2009, 11 Nov., 2009, Universiti Teknologi PETRONAS